Measurement of Single *W* Boson Production in *ep* Scattering

Ytsen R. de Boer

The research described in this thesis was performed at the DESY institute in Hamburg, Germany. During this time, the author was an external Ph.D. student at the University of Twente. During the research, the author was supported by the DESY programme for East-European and Russian students, as a member of the research group at the Institute for Theoretical and Experimental Physics (ITEP) in Moscow, Russian Federation. In addition, the author has received funding during this time from the following agencies:

- Prins Bernhard Cultuurfonds
- Fundatie van de vrijvrouwe van Renswoude

Y.R. de Boer
Measurement of Single W boson Production in ep Scattering

Cover design: Siebe Boersma, artist impression of the chaotic electron-proton interaction (front, back) and a diagrammatic depiction of a photon coupling to a W boson with subsequent decay of the latter in an electron-proton interaction (invitation).

Printed by Gildeprint B.V., Enschede 2007.

ISBN 978-90-365-2577-0

Measurement of single W boson production in ep scattering

PROEFSCHRIFT

ter verkrijging van de graad van
doctor aan de Universiteit Twente,
op gezag van de rector magnificus,
prof. dr. W.H.M. Zijm
volgens besluit van het College van Promoties
in het openbaar te verdedigen
op donderdag 10 Januari om 13.15 uur

door

Ytsen Ronald de Boer

geboren op 5 Januari 1977

te Harlingen, Nederland

This thesis has been approved by:

Promotor:	Prof. Dr. Ing. B. van Eijk
Co-Promotor:	Dr. C. Diaconu

To my parents and brother.

Contents

1 Introduction **1**

2 Electron-Proton Physics at HERA **3**
2.1 The Standard Model and Elementary Particles . . . 3
2.2 Electron-Proton Scattering and the HERA Programme . . . 4
2.3 Physics Processes . . . 8
2.3.1 Standard Model Signal Processes . . . 8
2.3.2 Standard Model Background Processes . . . 9
2.3.3 Beyond the Standard Model . . . 11

3 Single W Boson Production at HERA **13**
3.1 Single W Boson Production in the Standard Model . . . 13
3.2 Cross Section Calculation . . . 13
3.3 The $WW\gamma$ Vertex . . . 16
3.4 Decay Channels and Event Topology . . . 18
3.5 W Boson Polarisation Fractions . . . 19

4 HERA and the H1 detector **25**
4.1 The HERA storage ring . . . 25
4.2 The H1 Detector . . . 26
4.2.1 Tracking . . . 26
4.2.2 Calorimetry . . . 30
4.2.3 Time of Flight System . . . 31
4.2.4 Luminosity Monitoring System . . . 31
4.2.5 Muon Detectors . . . 31
4.2.6 Triggering . . . 31
4.3 Detector Simulation and Analysis Software . . . 32
4.4 Monte Carlo Generators . . . 32

5 Particle Identification and Event Reconstruction **33**
5.1 Track Reconstruction . . . 33
5.2 Electron Identification . . . 33
5.3 Electromagnetic Energy Calibration . . . 34
5.4 Muon Identification . . . 34
5.5 Reconstruction of the Hadronic Final State . . . 35
5.6 List of Observables in the Event . . . 35

6 Event Selection **37**
6.1 General Data Preselection . . . 37
6.1.1 Run Selection . . . 37
6.1.2 Event Vertex Position . . . 37
6.1.3 Triggers . . . 37
6.1.4 Non-ep Background Rejection . . . 38
6.2 Data Sets and Luminosities . . . 39
6.3 Selection of $\ell + \not{P}_T$ Events . . . 40

7 Cross Section Measurements **47**
7.1 Cross Section Extraction Method . . . 47
7.2 Measurement of the $\ell + \not{P}_T$ Cross Section . . . 47
7.3 Measurement of the $\ell + \not{P}_T$ Differential Cross Section . . . 49
7.4 Measurement of the Single W Boson Production Cross Section . . . 51
7.5 Treatment of Systematic and Statistical Uncertainties . . . 53

8 Measurement of the $WW\gamma$ Vertex **57**
8.1 Likelihood Fit . . . 57
8.2 Limits Extraction . . . 58
8.3 Results . . . 60
8.4 Systematic Uncertainties . . . 61

9 Measurement of the W Boson Polarisation Fractions **63**
9.1 W Boson Reconstruction . . . 63
9.2 Charge Measurement . . . 69
9.3 Final Sample for the W Boson Polarisation Measurement . . . 71
9.4 Extraction of the W Boson Polarisation Fractions . . . 72
9.5 Systematic Uncertainties . . . 78

10 Discussion and Conclusions **81**
10.1 Measurement of the $\ell + \not{P}_T$ Production Cross Section . . . 81
10.2 Measurement of Single W boson Production at HERA . . . 81
10.3 Measurement of the $WW\gamma$ Vertex . . . 82
10.4 Measurement of the W Boson Polarisation Fractions . . . 82
10.5 Outlook . . . 83

APPENDIX **85**

A-1 Samples **87**

References **89**

Summary **95**

Samenvatting **97**

Acknowledgements **99**

1 Introduction

The description of the unification of the electromagnetic and weak forces, as predicted by the Standard Model (SM) [1] has been validated by many experiments at the large particle accelerators during the last few decades. Absolute milestones are the discovery of the W and Z bosons at LEP (CERN) and the precise measurement of their masses [2, 3].

A key process in understanding the dynamics of the electroweak interactions in the SM is single W boson production. W boson properties have been studied in electron-positron (e^+e^-) collisions at LEP (CERN) and in proton-antiproton ($p\bar{p}$) collisions at the Tevatron (FNAL). The sole testing ground to study single W boson production in electron-proton (ep) scattering is the HERA collider at DESY [4].

HERA collides electrons[1] at 27.5 GeV with 920 GeV protons at a centre-of-mass energy of 320 GeV. The point particle nature of the electron provides a clean probe to the proton. Two collider-mode detectors H1 [5] and ZEUS [6] investigate in detail the proton structure and explore the energy frontier in electron-quark collisions.

The first years of running, 1994-2000, or the 'HERA I' period, yielded a profoundly enhanced insight into the structure of the proton [7, 8, 9]. Also in the electroweak sector, the ep scattering led to important confirmations of the SM [10]. After the year 2000, the accelerator and the detectors were upgraded and the HERA collider entered a new phase, HERA II, in which the specific luminosity was substantially increased and the electron beam was longitudinally polarised. The full data sample, collected until the collider shut-down on June 30, 2007, corresponds to an integrated luminosity of 0.5 fb^{-1}, balanced over e^+p and e^-p collisions. This harvest facilitated the search for rare processes and physics beyond the SM (BSM).

Single W boson production is an example of a rare process at HERA with a cross section of $\mathcal{O}(1)$ pb. One of the most striking signatures of this process is the observation of events with isolated leptons (electrons or muons) and missing transverse momentum, or '$\ell + \not{P}_T$' events. An excess of such events at the 3σ level was reported by the H1 collaboration in the HERA I data for the topology, atypical for the SM, where an additional prominent jet leads to a high hadronic transverse momentum (P_T^X) in the events [11]. This could not be confirmed by ZEUS [12]. In the full HERA I+II high-energy data set, an arguable excess of 2.3σ still persists in the limited region of phase space where the events have large P_T^X. Nevertheless, the purity of the H1 analysis in the signal, dominated within the SM by the W boson production, is at the 75% level.

A possible interpretation of the excess of $\ell + \not{P}_T$ events at large P_T^X, is provided by an anomalous triple gauge boson coupling (TGC) in W boson production at HERA, where a photon (γ) couples to a W boson at a $WW\gamma$ vertex. The differential cross section as a function of P_T^X is indeed predicted to be sensitive to an anomalous TGC [13]. Limits on the parameters that govern the TGC are calculated by applying statistical methods and using theoretical predictions.

Another tool to analyse the production mechanism is provided by the polarisation properties of the W boson. As an illustration, W bosons produced via top quark decay tend to display radically different

[1] In the following the term 'electron' will be used to refer generically to both electrons and positrons, unless stated otherwise.

polarisation behaviour than those radiated from up or down quarks. Therefore, deviations from the predicted behaviour not only may indicate BSM physics, but also provide additional information about its nature.

This thesis is organised as follows: An introduction to the ep physics at HERA is provided in Chapter 2. The production and properties of single W bosons in ep scattering is presented in Chapter 3. This includes a theoretical overview of the calculation of the single W boson production cross section, the $WW\gamma$ vertex, and the polarisation properties of the W boson at HERA. The HERA particle accelerator and the H1 detector are described in Chapter 4. The reconstruction of the final state particles, whereby various subdetectors of the H1 detector are used, is presented in Chapter 5. In Chapter 6, the selection of $\ell + \not{P}_T$ events is discussed. The production rate of such events is determined in Chapter 7, where the most precise determination of the single W boson production cross section to date in ep scattering is also presented. The measurement of $\ell + \not{P}_T$ events is used in the direct measurement of the triple boson coupling $WW\gamma$, which is described in Chapter 8. The measurement of the W boson polarisation properties is presented in Chapter 9. Finally, Chapter 10 concludes this thesis with a discussion of the results.

2 Electron-Proton Physics at HERA

This chapter provides an introduction to the electron-proton scattering at HERA. In the first section a short introduction of the Standard Model of particles and forces is given. Then, a short overview of the highlights of the HERA physics is presented. Finally, the Standard Model processes, relevant for this work, are discussed.

2.1 The Standard Model and Elementary Particles

The Standard Model (SM) [1], developed in the 1960's, describes the electromagnetic, weak, and strong interactions and explains in a unified way a large variety of experimental observations. The elementary particles of the SM are grouped into bosons and fermions. The bosons are the gluon, the Z^0, the $W^{\pm}$, and the photon, denoted by γ. They are integer spin particles and mediate the strong, weak, and electromagnetic forces, respectively (Table 2.1). In the interactions of elementary particles, the gravitational force is too weak to play a significant role. This is due to the small masses of the elementary particles.[1] The fermions in the SM are half integer spin particles and are further divided into two groups: quarks and leptons. Quarks have never been observed as free particles, they always form bound states called 'hadrons'. Quarks interact via all boson types whereas leptons interact only via $Z, W^{\pm}$, and, if the lepton is charged, via γ as well. Leptons occur as free particles in abundance.

Each particle in the SM is associated with an antiparticle, which has the same mass and opposite electric charge. All quarks and leptons can be classified into three generations. The particle content of the SM is summarised in Table 2.2. Each lepton generation consists of a charged and a neutral particle. Among the charged leptons only the electron is stable. Neutral leptons are called neutrinos (ν) and are massless in the SM.[2] Quarks carry fractional electric charge and occur in six varieties of flavours: up (u), down (d), charm (c), strange (s), top (t) and bottom (b).

Experiment has shown that the weak charged currents ($W^{\pm}$) cause transitions between the fermions within a generation (not between generations). Remarkably enough, this pertains only to left handed fermions for which the spin is oppositely aligned with the direction of motion. Therefore, in the electroweak sector of the SM, the left handed (L) fermions appear in so-called weak isospin doublets, whereas the right handed (R) fermions, where the spin is aligned with the direction of motion, appear in weak isospin singlets. This is also referred to as the 'V-A' chiral structure. For the first generation quarks and leptons this looks like

$$\begin{pmatrix} e \\ \nu_e \end{pmatrix}_L, \begin{pmatrix} u \\ d \end{pmatrix}_L, \quad \text{and} \quad (e)_R, (u)_R, (d)_R. \tag{2.1}$$

The right handed neutrino $(\nu)_R$ is missing, since it has never been observed.

In the SM, all interactions between the particles and forces are described in the Lagrangian formalism, in which all SM particles are massless. Mass is given to each particle via its interaction with an

[1] The gravitational force, presumably mediated by a particle called the graviton, is not included in the SM.
[2] Experiments, however, provide strong evidence that the neutrinos cannot be massless [14].

Force	Relative strength	Couples to	Mediated by
Strong	1	quarks	gluon
Electromagnetic	1.4×10^{-2}	quarks/charged leptons	γ
Weak	2.2×10^{-6}	all	Z^0, $W^{\pm}$

Table 2.1: *The Standard Model bosons and the particles to which they couple.*

LEPTONS (spin= 1/2)				**QUARKS (spin= 1/2)**			
Flavour		Mass (GeV)	Electric charge	Flavour		Approx. Mass (GeV)	Electric charge
$\boldsymbol{\nu_e}$	electron neutrino	$< 1 \times 10^{-8}$	0	$\boldsymbol{u}$	up	0.003	2/3
$\boldsymbol{e}$	electron	0.000511	-1	$\boldsymbol{d}$	down	0.006	$-1/3$
$\boldsymbol{\nu_\mu}$	muon neutrino	< 0.0002	0	$\boldsymbol{c}$	charm	1.3	2/3
$\boldsymbol{\mu}$	muon	0.106	-1	$\boldsymbol{s}$	strange	0.1	-1/3
$\boldsymbol{\nu_\tau}$	tau neutrino	< 0.02	0	$\boldsymbol{t}$	top	175	2/3
$\boldsymbol{\tau}$	tau	1.7771	-1	$\boldsymbol{b}$	bottom	4.3	-1/3

Table 2.2: *The three generations of quarks and leptons in the Standard Model. Also shown are the forces described in the Standard Model with their relative strengths evaluated at $Q = 1$ GeV. Throughout this thesis a system of natural units is used where $\hbar = c = 1$, therefore particle masses are written in units of GeV.*

additional particle. This is the Higgs boson, which is needed to explain why particles have mass. The Higgs boson is the only SM particle that has not been observed and its discovery is the primary goal of the near-future experiments.

The probing of elementary particles and their interactions by means of scattering experiments was opened by Rutherford, in the beginning of the twentieth century. He collided alfa-particles on a gold foil and discovered that the gold consists of hard point-like nuclei and not, as was commonly assumed, of a continuous matter [15]. In fixed-target experiments, leptons were scattered off the nuclei to further resolve their substructure. The resolution with which the 'target' can be analysed, depends on the transfered momentum in the scattering Q^2. The higher Q^2, the more detail that can be resolved. The quarks and gluons were discovered using leptons with higher and higher energies until eventually the nucleus broke in the so-called 'Deep Inelastic Scattering' (DIS). This analysis is continued at HERA where the world's best resolution is obtained in resolving the substructure of the proton.

2.2 Electron-Proton Scattering and the HERA Programme

Kinematics

Electron proton (ep) scattering in the SM occurs via the exchange of a γ, Z or $W^{\pm}$. This is diagrammatically shown in Figure 2.1. In the case of a neutral γ or Z boson exchange, one speaks of a 'Neutral Current' (NC) process $ep \to eX$. The process is called 'Charged Current' (CC), $ep \to \nu X$, when the mediating particle is a charged boson, W. For a fixed center of mass energy $\sqrt{s}$, the kinematics of ep scattering can be uniquely described by two Lorentz invariant quantities: Q^2, the negative squared

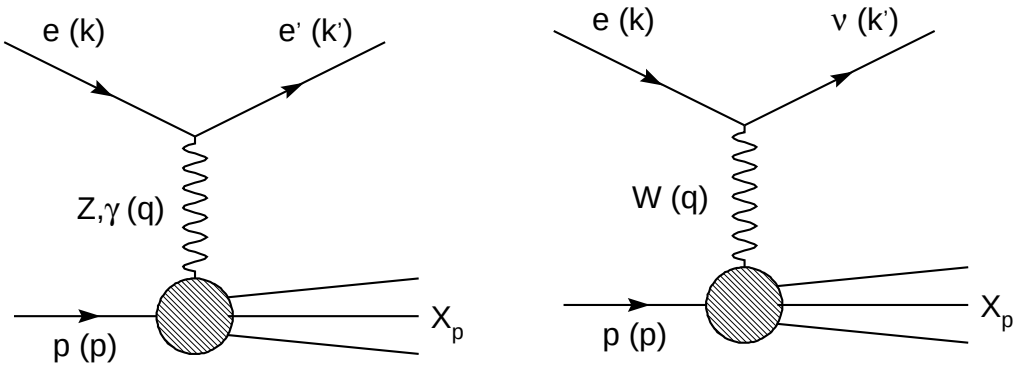

Figure 2.1: *Electron-proton (ep) scattering under the exchange of a neutral gauge boson Z or γ (left) or a charged gauge boson W (right). X is the outgoing hadronic system. The incoming proton (p) and electron (e) have four momentum (p) and (k), respectively. The four momentum of the exchanged boson is denoted by (q).*

four momentum of the exchanged boson, and the Bjorken scaling variable x. Another common Lorentz invariant variable is y, the inelasticity. These variables are explicitely defined as

$$Q^2 \equiv -q^2, \qquad x \equiv \frac{Q^2}{2p \cdot q}, \qquad y \equiv \frac{p \cdot q}{k \cdot p}, \tag{2.2}$$

where q is the four momentum of the exchanged boson, p the four momentum of the incoming proton, and k that of the incoming electron. y corresponds to the energy fraction of the incident electron carried by the exchanged boson in the proton rest frame. The inelasticity y is related to x and Q^2 by the relation

$$Q^2 = xys, \tag{2.3}$$

when the particle rest masses are neglected.

Cross Sections and Structure Functions

The NC and CC differential cross sections in $e^{\pm}p$ scattering as a function of x and Q^2 can generally be expressed as

$$\frac{d^2\sigma_{\mathrm{NC}}}{dxdQ^2} = \frac{e^4}{8\pi x}\left(\frac{1}{Q^2}\right)^2 \phi^{\pm}_{\mathrm{NC}}\left(x, Q^2\right), \tag{2.4}$$

$$\frac{d^2\sigma_{\mathrm{CC}}}{dxdQ^2} = \frac{g^4}{64\pi x}\left(\frac{1}{Q^2 + M^2_{W^{\pm}}}\right)^2 \phi^{\pm}_{\mathrm{CC}}\left(x, Q^2\right), \tag{2.5}$$

with e the unit charge and g, the weak coupling constant. Latter two are related by $g^2 = e^2/\sin^2(\theta_W)$, where θ_W is the Weinberg Mixing Angle. The terms $\frac{1}{Q^2}$ and $\frac{1}{Q^2+M^2_W}$ refer to the exchanged 'propagating' or 'virtual' particles, which are represented by internal lines in Feynman diagrams. The NC

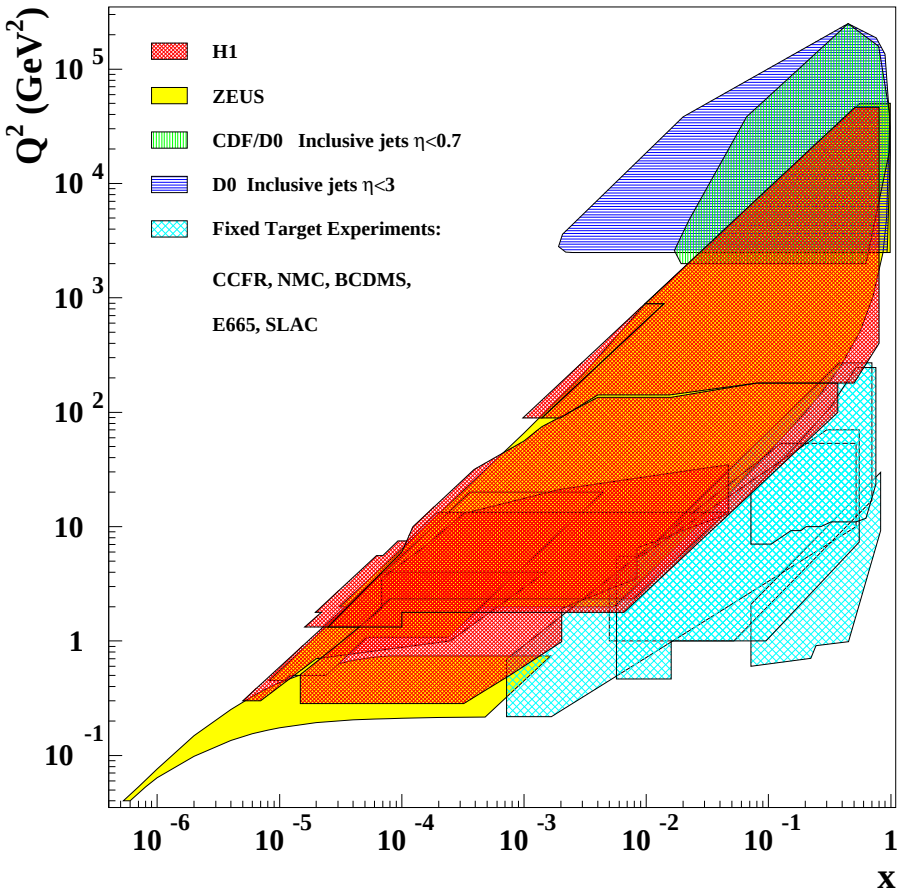

Figure 2.2: *Kinematic plane in x and Q^2 covered by the HERA experiments H1 and ZEUS, in comparison to some fixed-target and $p\bar{p}$ experiments (CDF/D0).*

cross section (2.4) is largest at low Q^2, when the photon is near its mass shell $Q^2 \simeq 0$ GeV^2. The $\phi_i^{\pm}$, where $i = NC$ or CC, are a linear combination of the structure functions $F_{i,2}$, $F_{i,L}$, and $xF_{i,3}$

$$\phi_i^{\pm} \propto Y_+ F_{i,2}^{\pm}\left(x, Q^2\right) - y^2 F_{i,L}^{\pm}\left(x, Q^2\right) \mp Y_- x F_{i,3}^{\pm}\left(x, Q^2\right), \tag{2.6}$$

where $Y_{\pm} = 1 \pm (1-y)^2$. In case of a NC interaction, the structure functions $F_{i,2}$ and $F_{i,3}$ include terms regarding the pure γ or Z exchange and the γZ interference. For CC processes, they only describe the exchange of a W boson. $F_{i,L}$ is the longitudinal structure function, describing interactions whereby a longitudinally polarised vector boson is exchanged.

The HERA Programme

As mentioned in the introduction, the HERA I programme focused mainly on analysing the structure of the proton. The measurements regarding F_2 have changed the view of the proton structure [7, 8, 9]. These were facilitated by the increase of the kinematic range by HERA with respect to the range so far accessible in fixed-targets experiments. This is shown in Figure 2.2, where for several fixed-target experiments, $p\bar{p}$ experiments (D0 and CDF) and ep experiments (H1 and ZEUS) the kinematic ranges

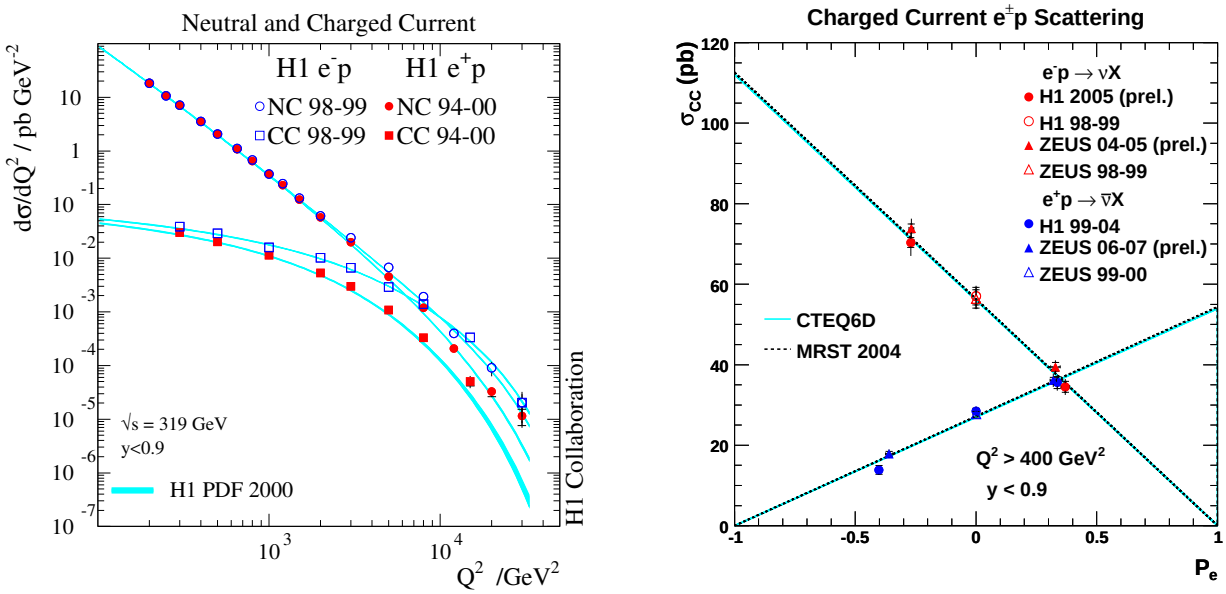

Figure 2.3: *Left: The differential NC and CC cross sections as a function of Q^2 measured by H1 for e^-p and e^+p data [10]. Right: The dependence of the CC cross section on the positron beam polarisation.*

are presented. The fixed-target experiments probe the very low Q^2 region at moderate values of x and the $p\bar{p}$ experiments cover the very high Q^2 region for the same x range. The ep experiments, however, cover a much wider range in Q^2, from 0.2 to $5 \cdot 10^5$ GeV^2 and have access to values of x as far down as $x \sim 10^{-6}$.

A textbook example of a HERA I measurement in the electroweak sector is the determination of the single differential NC and CC cross sections as a function of Q^2 [10]. This is shown on the left hand side of Figure 2.3. The NC cross section dominates for small values of Q^2, due to the photon propagator in Equation (2.4). The CC cross section is suppressed by the heavy W boson propagator, but for Q^2 of the order of the mass of the W boson, it becomes comparable to the NC cross section. The CC cross section is larger in e^-p scattering than in e^+p scattering. This is due to the presence of two positively charged valence quarks inside the proton. By fitting the CC cross section to its Q^2 dependence, the W boson mass was determined to be $80.9 \pm 3.7 \pm 3.7$ GeV. This value agrees well with the mass of the W boson as previously measured at LEP, thereby confirming the electroweak sector of the SM in lepton nucleon scattering in processes where the W boson is virtual [10].

The HERA II programme makes use of an increased luminosity and the availability of longitudinally polarised lepton beams. The dependence of the CC cross section on the polarisation of the lepton beam is shown on the right hand side of Figure 2.3. The measurement is consistent with the prediction of a vanishing cross section for such interactions involving right handed fermions and the upper limit is set to 1.9 pb at 95% Confidence Level (CL).

The installation of new quadrupole magnets resulted in the luminosity increase, which made it possible to study the rare and exotics, put on the centre stage in the HERA II programme. The single W boson production process, analysed in this thesis, is part of that programme.

The final stages of the HERA programme were dedicated to the direct measurement of the longitudinal structure function F_L. As mentioned above, F_L describes the couplings between quarks and longitudinally polarised bosons. Since only off-shell quarks can couple to such bosons, F_L is sensitive to higher-order processes containing off-shell quarks and gluons. So far, only the indirect measurement of F_L was possible [16]. To understand why $\sqrt{s}$ has to be varied to perform the measurement, Equations (2.4) and (2.6) must be considered. They show that, when xF_3 is ignored, which is valid at low Q^2 [17], the NC cross section is proportional to y^2

$$\sigma_{NC} \propto F_2^{\pm}\left(x, Q^2\right) - \frac{y}{Y_+} F_L^{\pm}\left(x, Q^2\right). \tag{2.7}$$

This shows that F_L can be directly measured by deriving σ_{NC} at fixed values for x and Q^2 and varying $\sqrt{s}$, since $Q^2 = xys$ (Equation (2.3)).

2.3 Physics Processes

In this section, the *ep* processes that are relevant for the current analyses are discussed. The SM signal processes are presented first. These are characterised by events containing an energetic, isolated lepton (electron or muon) and large genuine missing transverse momentum in the final state, or 'ℓ+$\not{P}_T$' events. If the isolated lepton is an electron (muon) it is said to contribute in the electron (muon) 'channel'.

Due to the limited geometrical acceptance of the detector and fluctuations in the shower development of the final state particles, other SM processes can have the topological signature identical to that of the $\ell + \not{P}_T$ events and become indistinguishable from it. These are 'background' processes, the most important of which are discussed here. Finally, there is one BSM process that plays a benchmarking role in this thesis. This is anomalous single top production and is also discussed here.

2.3.1 Standard Model Signal Processes

Single W boson Production

The main contribution to ℓ+$\not{P}_T$ events ($\sim 97\%$) comes from single W boson production with subsequent leptonic decay. This process is the main focus of this work and is described in detail in Chapter 3.

Z Boson Production

The production of a Z boson with subsequent decay $Z \to \nu\bar{\nu}$ contributes to the $\ell + \not{P}_T$ signal. Shown in Figure 2.4 are the dominant Z boson production diagrams with subsequent decay $Z \to \nu\bar{\nu}$. The LO Drell-Yan process on the left hand side occurs predominantly at $Q^2 \simeq 0$ and the scattered electron escapes undetected down the beam-pipe. The contribution from the Cabbibo-Parisi process on the right hand side of the figure, however, cannot be neglected [18]. The branching ratio for the decay $Z \to \nu\bar{\nu}$ is $\sim 20\%$. This process is a background in the electron channel only. The contribution from this process to the total $\ell + \not{P}_T$ production cross section is $\sim 3\%$.

It is important to note that in the analyses related to the W boson, later in this thesis, the Z production process is considered to be background.

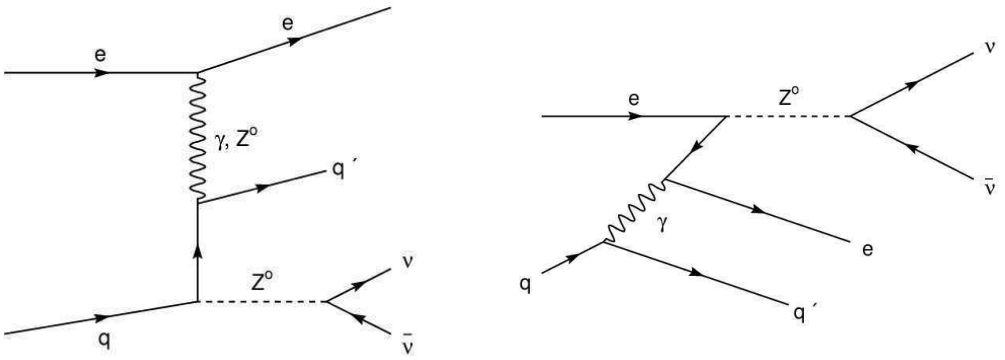

Figure 2.4: *Feynman diagrams for the Z production processes with subsequent $Z \rightarrow \nu\bar{\nu}$ decay. Left: Leading order Z production. Right: The Cabbibo-Parisi process.*

2.3.2 Standard Model Background Processes

Neutral Current in DIS

In the NC process in DIS, the scattered electron is well isolated from the jet and can play the role of the isolated lepton in the event. However, the event is expected to be balanced in P_T, therefore any $\not{P}_T$ can only arise from measurement fluctuations. Since there are no isolated muons in NC events, this process is background only in the electron channel.

Charged Current

CC events have genuine $\not{P}_T$ due to the neutrino, which escapes detection. An isolated lepton can only arise from the misidentification of a hadron, which is separated from a jet. This process is a background in both the electron and muon channel.

Lepton Pair Production

The Lepton Pair Production (LL) process is shown in Figure 2.5. The lepton pair is produced in a $\gamma\gamma$ process. Due to measurement fluctuations, such events can aquire finite $\not{P}_T$. If, in addition, one lepton escapes detection, lepton pair production can fake the ℓ+$\not{P}_T$ signature. More details on Lepton Pair production at HERA can be found in [19].

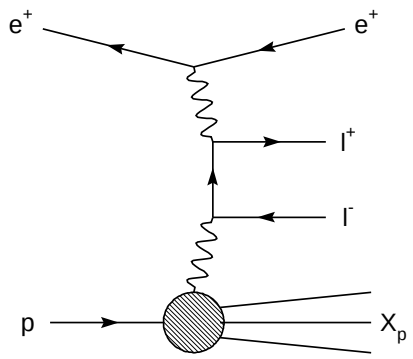

Figure 2.5: *Lepton Pair production.*

Photoproduction and Compton Scattering

The NC processes generated near the photon propagator pole in Equation (2.4) are called photoproduction. The photon is quasi on-shell, $Q^2 \simeq 0$ GeV^2. Due to the limited geometrical acceptance of the detector the scattered electron escapes down the beam-pipe, much to the contrary in DIS, where the large Q^2 forces the scattered electron into the detector. A common convention at

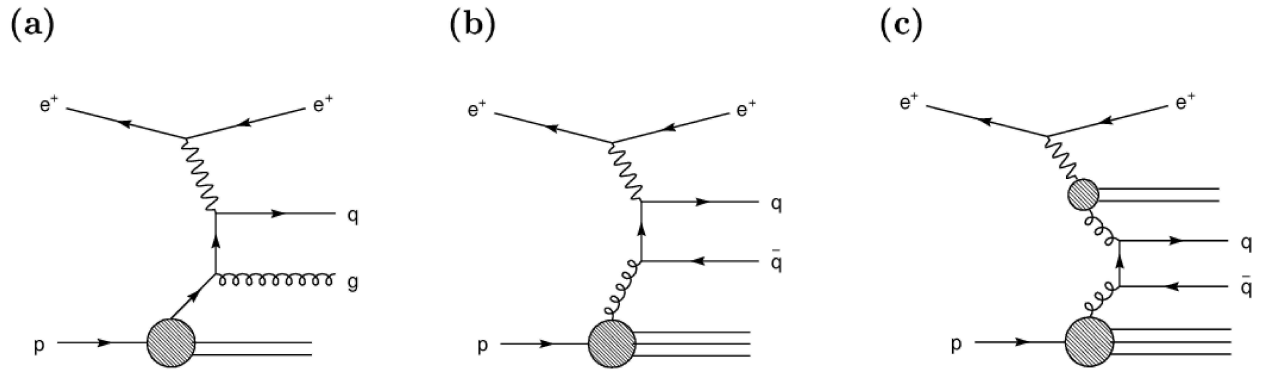

Figure 2.6: *Feynman diagrams for direct and resolved photoproduction processes at tree level. (a) QCD Compton (direct) (b) boson-gluon fusion (direct), and (c) resolved photon process.*

H1 is to speak about photoproduction when $Q^2 < 4$ GeV^2. For these values of Q^2, the proton structure cannot be resolved and the proton interacts as a point particle.

The photoproduction processes are divided into 'direct' and 'resolved' photoproduction. Example diagrams are shown in Figure 2.6. In direct photoproduction the photon couples directly to the hard process, whereas in resolved photoproduction, the photon fluctuates into a $q\bar{q}$ quark pair, one of which then participates in the hard collision.

Compton Scattering is the process $ep \to e\gamma X$, with X an arbitrary hadronic final state.[3] Feynman diagrams are shown in Figure 2.7.

Photoproduction and Compton Scattering contribute to the background in the case of the misidentification of a hadron that is separated from a jet as an isolated lepton. Fluctuations in the hadronic final state can lead to fake missing energy. Despite the large cross section of photoproduction, the contribution of this process to $\ell + \not{P}_T$ events is negligible [20]. The contribution from Compton Scattering is small but is taken into account.

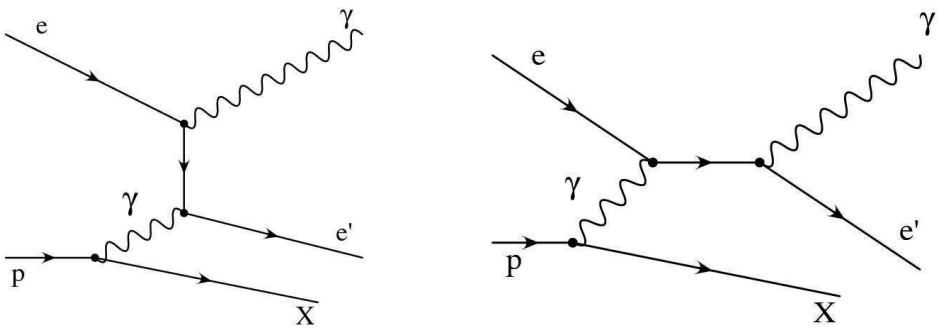

Figure 2.7: *Feynman diagrams of the bremsstrahlung process with bremsstrahlung off the electron line.*

[3]This process is also referred to as bremsstrahlung or the Bethe-Heitler process.

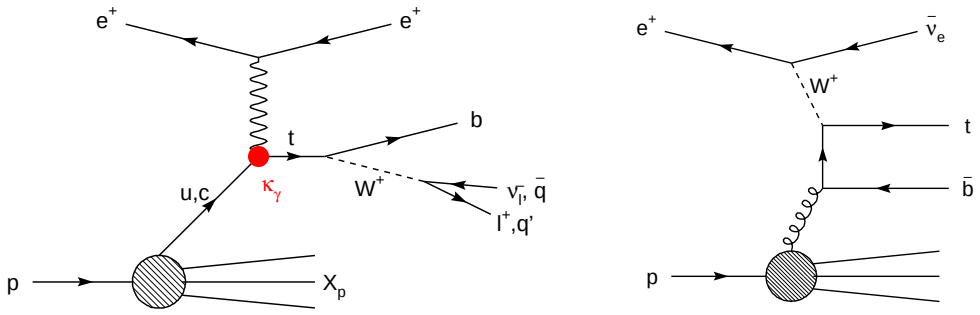

Figure 2.8: *Feynman diagrams of anomalous single top production (left) via flavour changing neutral current (FCNC) and SM single top production (right). u and c denote the up and charm quarks.*

2.3.3 Beyond the Standard Model

Many Beyond the Standard Model (BSM) theories predict processes that would lead to $\ell + \not{P}_T$ events. Usually these involve the production of a heavy particle that produces some invisible particle in its decay chain and, additionally, either an isolated lepton is produced or it is the scattered electron that assumes this role.

The anomalous single production of a top quark is discussed here. The diagram of this process is shown on the left in Figure 2.8. The production cross section is proportional to the coupling κ_γ^2, in a flavour changing neutral current (FCNC) process. The SM process of single top production has a negligible cross section of less than 1 fb at HERA. One such diagram is shown on the right hand side of the figure.

The interest in this BSM single top production was triggered by the observation of the H1 collaboration of an excess of $\ell + \not{P}_T$ events in the high P_T^X region, which is typical for this process. In addition, it serves well to demonstrate that the single W boson from the top quark decay has a radically different polarisation behaviour than those in the SM. This will be discussed in the next chapter.

3 Single W Boson Production at HERA

This chapter describes the theoretical aspects of the SM production of single W bosons in ep scattering at HERA.[1] The calculation of the production cross section, the parametrisation of the $WW\gamma$ vertex, and the polarisation properties of the W boson are discussed.

3.1 Single W Boson Production in the Standard Model

In the SM there are two channels that contribute to single W boson production in ep scattering. These are

$$ep \to eWX \tag{3.1}$$

and

$$ep \to \nu WX. \tag{3.2}$$

Here e is an electron, ν a neutrino, W the quasi real, unstable W boson, and X the recoiling hadronic system. The corresponding Feynman diagrams at parton level are shown in Figure 3.1.[2] Diagram (a) and (b) are the dominant diagrams due to the photon (γ) and, in Diagram (a) only, quark (q) propagators (Section 2.2). Diagram (c) involves the triple gauge boson couplings (TGC) $WW\gamma$ and WWZ. Diagrams (d) and (e) contain off-shell (non-resonant) W bosons and are needed to preserve electromagnetic gauge invariance when considering the W boson decay to leptons [21].

3.2 Cross Section Calculation

The SM Leading Order (LO) W boson production cross section (σ_W) is calculated within the EPVEC generator framework [21], where use is made of the CTEQ4M [22] parametrisation of the proton structure function and the ACFGP [23] parametrisation of that of the photon.

The main difficulty in the calculation is the regularisation of the fermion pole from Diagram 3.1 (a), since close to the pole, QCD corrections become large. Poles can occur in three configurations, as is explained in Figure 3.2, and the fermion pole in Diagram 3.1 (a) appears in a u-channel configuration.

Close to the pole, the photon is quasi on-shell, $Q^2 \simeq 0$, and fluctuates into a $q\bar{q}$ pair. The W boson is produced via the standard Drell-Yan process [24], where one quark originates from the photon's $q\bar{q}$ pair and the other from the proton. The applied strategy to calculate the total cross section is to split the phase space into two regions, which have to be matched carefully to avoid double-counting

$$\sigma_W = \sigma\left(|u| > u_{cut}\right) + \int^{u_{cut}} d|u| \frac{d\sigma}{d|u|}, \tag{3.3}$$

where

$$u = \left(p_q - q_W\right)^2, \tag{3.4}$$

[1] When anomalous non-SM couplings are discussed, it is assumed that all other parameters have their SM values.
[2] The diagrams involving antiquarks are implied.

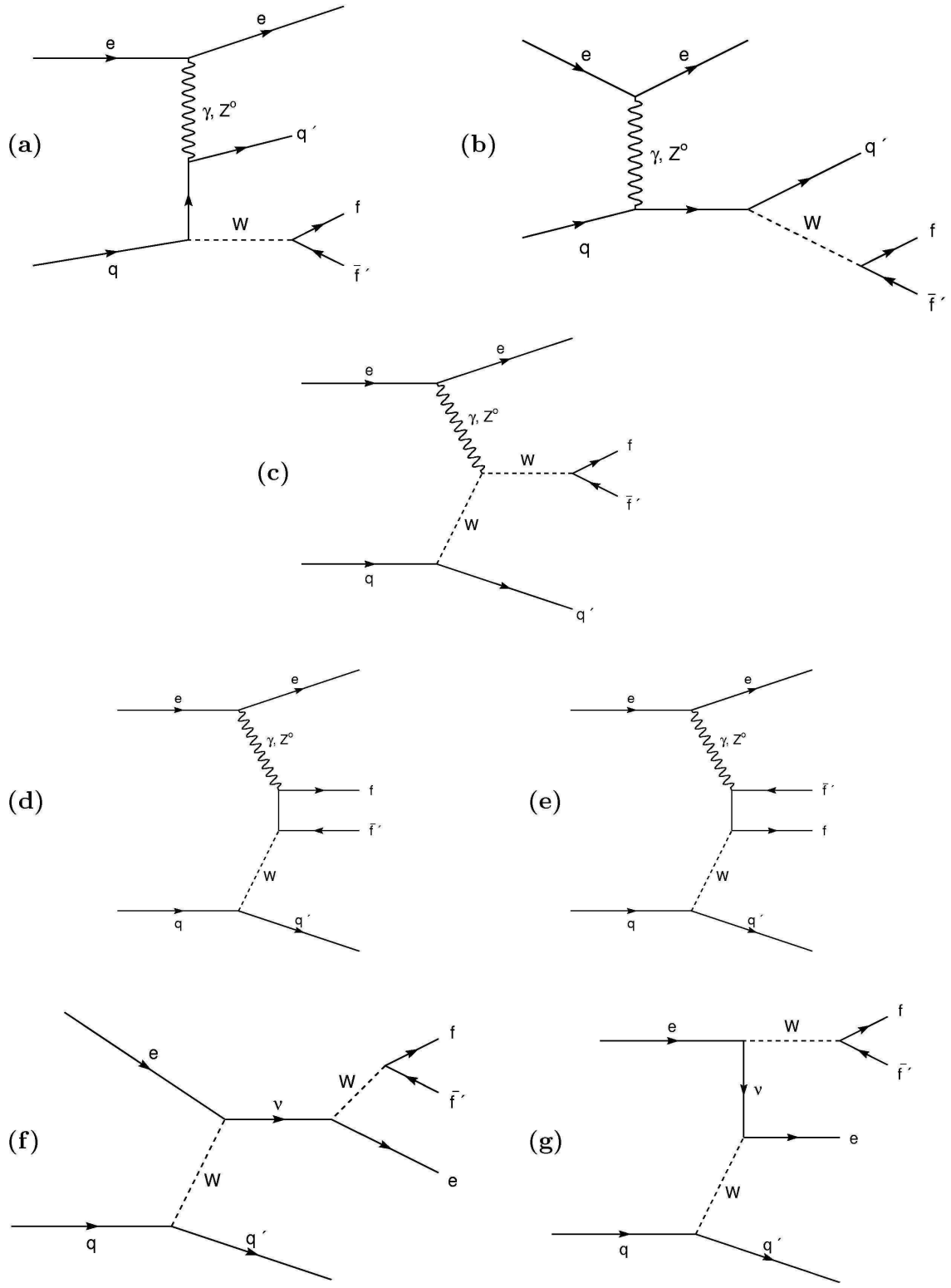

Figure 3.1: *Feynman diagrams for the process* $ep \to eWX$ *with the* W *decay:* $W \to f\bar{f}'$.

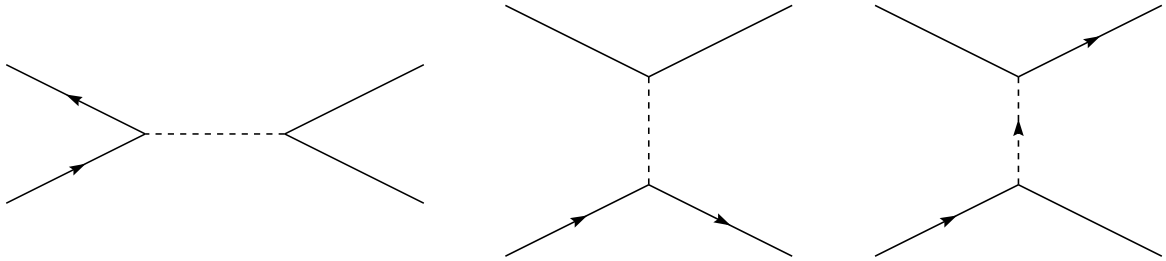

Figure 3.2: *Schematic of processes with a propagating particle (dotted internal line) in a s-channel (left) t-channel (middle) or u-channel (right) configuration.*

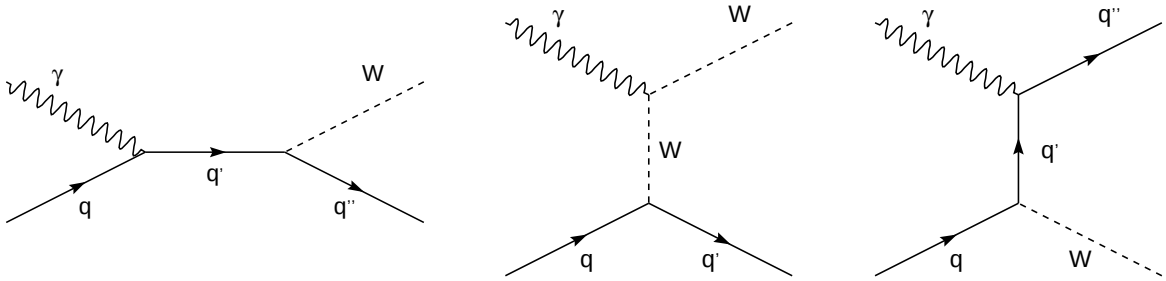

Figure 3.3: *Feynman diagrams contributing to $\gamma q \to W q'$ in the Weizsäcker-Williams approximation.*

and p_q and q_W are the four momenta of the incoming quark and the W boson, respectively. Far away from the pole where $u > u_{cut}$ (DIS regime) no large QCD contributions are expected and the cross section is calculated using the matrix elements for the complete process including the W boson decay to leptons. For the region $u < u_{cut}$ the photon is nearly on-shell, which facilitates the use of the Weizsäcker-Williams approximation (WWA) [25, 26] where only the matrix element for $\gamma q \to W q'$ is considered, thus ignoring the W boson decay. The only three diagrams that contribute are shown in Figure 3.3.

In the integration over the phase space for $u < u_{cut}$, both a divergent and finite term appear. The finite term describes the direct photoproduction contributions from Diagrams (b)-(e) in Figure 3.1. The divergent term contains the u-channel pole as a singularity and represents the single W boson production at small values of u. This term can be substituted by a photon distribution function, which eliminates the singularity and at the same time includes higher order QCD corrections by solving the LO inhomogeneous Altarelli-Parisi equation for the parton content of the photon [27].

The LO EPVEC calculations are reweighed on an event-by-event basis [28]. The procedure employs analytical NLO calculations [29, 30] for the resolved photoproduction regime, which represents the largest contribution to the total cross section. The reweighing is done as a function of the differential distributions of the transverse momentum P_T^W and rapidity y_W of the W boson [31]. This is possible since the NLO corrections are moderate and hardly affect the shapes of the distributions, as can be seen from the predominantly flat distributions in Figure 3.4, where the applied weights as a function

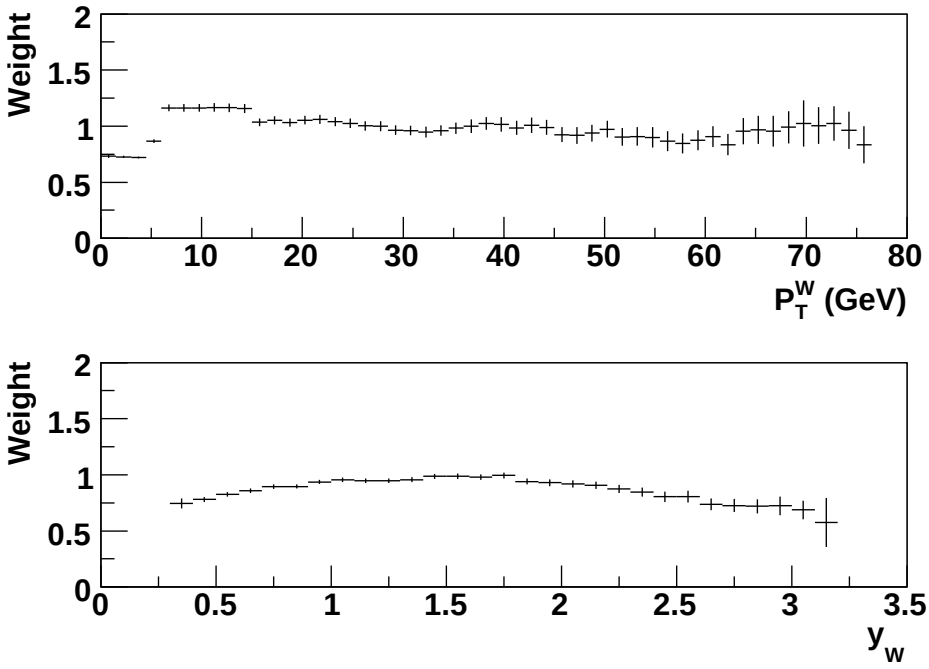

Figure 3.4: *Applied event weights as a function of the transverse momentum P_T^W and rapidity y_W of the W boson.*

of P_T^W and y_W are shown. Only at low P_T^W the corrections are sizeable. This is where the resolved photoproduction component dominates and the corrections have the largest impact. Contrary to what one might expect, the reweighing procedure leads to a reduction of the total LO EPVEC cross section. This is due to the different approaches for separating the photoproduction and DIS regimes in the calculations employed by EPVEC and the authors of Refs. [29, 30]. The latter use Q^2 for this, whereas in EPVEC the separation is based on the u-channel momentum transfer (Equation (3.3)). The EPVEC LO calculations are 20% larger than the LO calculations in Refs. [29, 30] and the distributions get reweighed only moderately when the NLO determined weights from Refs. [29, 30] are applied.

After proper reweighing, the EPVEC results are brought to within 10% of the NLO calculations, reducing the total theoretical uncertainty to about 15%.

3.3 The $WW\gamma$ Vertex

The Triple Gauge Boson Coupling (TGC) at parton level is shown in Diagram 3.1 (c). The Z boson exchange diagram with the WWZ coupling is suppressed by the large mass of the Z boson and no sensitivity to this coupling is expected. The tensor structure of the $WW\gamma$ vertex allows for four free

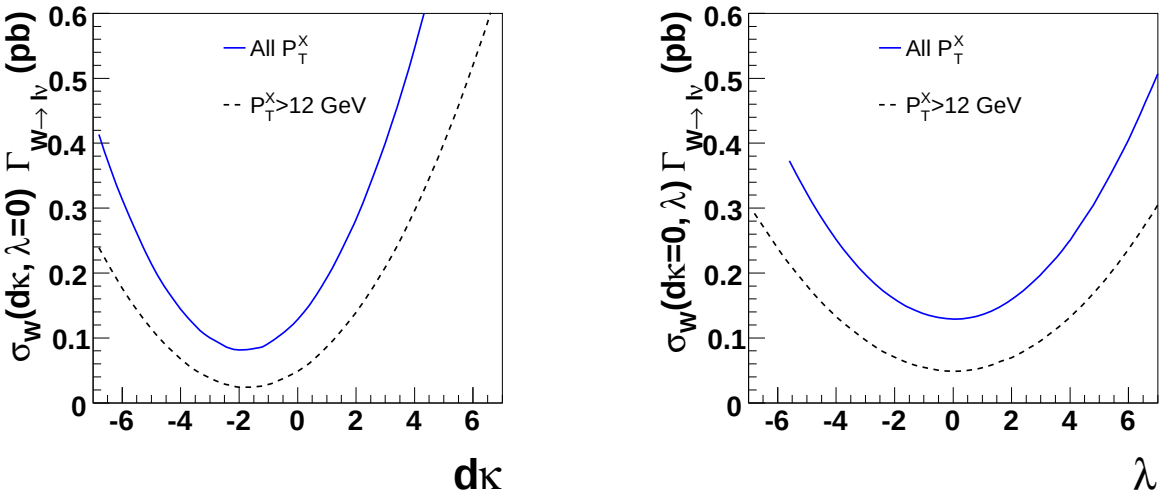

Figure 3.5: *The predicted total production cross section for single W bosons (with the subsequent decay $W \to \ell\nu$) as a function of κ (left) and λ (right) for the full phase space P_T^X (continuous line) and $P_T^X > 12$ GeV (dotted line). One parameter is allowed to vary at the time while all other parameters are fixed to their SM values.*

effective parameters that are conveniently described by the effective Lagrangian [32]

$$\begin{aligned}\mathcal{L}_{WW\gamma} &= -ie\Big\{\Big(W^\dagger_{\mu\nu}W^\mu A^\nu - W^\dagger_\mu A_\nu W^{\mu\nu}\Big) \\ &\quad +\kappa W^\dagger_\mu W_\nu F^{\mu\nu} + \frac{\lambda}{M_W^2}W^\dagger_{\lambda\mu}W^\mu_\nu F^{\nu\lambda} + \\ &\quad +\tilde{\kappa}W^\dagger_\mu W_\nu \tilde{F}^{\mu\nu} + \frac{\tilde{\lambda}}{M_W^2}W^\dagger_{\lambda\mu}W^\mu_\nu \tilde{F}^{\nu\lambda}\Big\}. \end{aligned} \tag{3.5}$$

Here W_μ denotes the W^- field and A_ν is the photon field. $W^{\mu\nu} = \partial^\mu W^\nu - \partial^\nu W^\mu$, $F^{\mu\nu} = \partial^\mu A^\nu - \partial^\nu A^\mu$, and $\tilde{F}_{\mu\nu} = \frac{1}{2}\epsilon_{\mu\nu\rho\sigma}F^{\rho\sigma}$. e is the unit charge. In the SM, the four coupling parameters have the following values

$$\kappa = 1, \qquad \lambda = 0, \qquad \tilde{\kappa} = 0, \qquad \tilde{\lambda} = 0. \tag{3.6}$$

The first term (in parentheses) in the effective Lagrangian (3.5) represents the electromagnetic coupling $U(1)_{\mathrm{EM}}$ of the photon to the electric charge of the W boson. It is important to note that the second term (κ) is an explicit consequence of the non-Abelian $SU(2)_W \otimes U(1)_Y$ symmetry of the SM. The coupling parameters κ ($\tilde{\kappa}$) and λ ($\tilde{\lambda}$) are related to the magnetic (electric) dipole moment

μ_W (d_W) and the electric (magnetic) quadrupole moment Q_W ($\tilde{Q}_W$) of the W^+

$$\mu_W = \frac{e}{2M^W}(1+\kappa+\lambda), \tag{3.7}$$

$$Q_W = -\frac{e}{M_W^2}(\kappa-\lambda), \tag{3.8}$$

$$d_W = \frac{e}{2M_W}\left(\tilde{\kappa}+\tilde{\lambda}\right), \tag{3.9}$$

$$\tilde{Q}_W = -\frac{e}{M_W^2}\left(\tilde{\kappa}-\tilde{\lambda}\right). \tag{3.10}$$

In this thesis, limits are set on the parameters κ and λ. All other parameters are assumed to have their SM values. Instead of κ, the parameter

$$d\kappa \equiv \kappa - 1 \tag{3.11}$$

will be used, such that any non-zero value for $d\kappa$ is a deviation from the SM.

The main contribution to $ep \to eWX$ arises from Diagram (a) in Figure 3.1 due to the u-channel pole. These events have in general small values of the transverse momentum of the recoiling hadronic system P_T^X. Since the $WW\gamma$ vertex does not enter this diagram, an enhanced sensitivity to anomalous values of $d\kappa$ and λ is expected at larger values of P_T^X. This is shown in Figure 3.5, where the predicted dependence of the W boson production cross section σ_W on the parameters $d\kappa$ and λ in the complete phase space is compared to that at $P_T^{\text{jet}} > 12$ GeV.[3]

3.4 Decay Channels and Event Topology

The leptonic and hadronic W boson decay channels $W \to q\bar{q}$ and $W \to \ell\nu$, account together for $\sim 99\%$ of all decays. The measured branching ratios [33] are shown in Table 3.4.

In the leptonic decay $W \to \tau + \nu$ the tau (τ) is not stable. The branching ratio for the decay $\tau \to e/\mu + \nu$ is $\sim 36\%$. W boson production events with subsequent τ decay $W \to \tau\,(\to e/\mu + \nu) + \nu$ are in practice indistinguishable from $ep \to eW\,(\to e/\mu + \nu)\,X$ and contribute to $\ell + \not{P}_T$ events. In the case of the hadronic τ decay $\tau \to q\bar{q}'$, the CC background makes the analysis problematic [34]. The identification of the hadronic W boson decay mode $W \to q\bar{q}'$ is extremely difficult due to the large photoproduction background [35] and is not considered in this thesis.

In case of the leptonic decay $W \to e/\mu + \nu$, the final state has a very clear detector signature. A convenient detection phase space for single W boson production at H1 can be defined where the lepton has $P_T > 10$ GeV and a polar angle $5^o < \theta < 140^o$. In addition, the distance between the lepton and any jet in the event, D^{jet}, should be at least one unit in $\eta - \phi$ space and the missing transverse momentum in the event, $\not{P}_T$, is required to be larger than 12 GeV.[4] The fraction of the total W boson production cross section in this detection phase space is 0.820.

Various distributions of kinematic quantities as generated by EPVEC are shown in Figures 3.6-3.9 in both the full phase space, as well as in the detection phase space. As is shown in Figures 3.6 and 3.7, both leptons originating from the W boson decay have the hard P_T spectrum peaking around

[3] P_T^{jet} is the generated P_T of the quark from which the W boson radiated and can readily be compared to the reconstructed quantity P_T^X.

[4] The detection phase space is also determined by the detector geometry and the kinematics of SM background processes. See Section 6.3.

$W^{\pm}$ decay modes	Fraction	Confidence Level
$\ell + \nu$	$(10.80 \pm 0.09)\,\%$	
e^+nu	$(10.75 \pm 0.13)\,\%$	
$\mu^+\nu$	$(10.57 \pm 0.15)\,\%$	
$\tau^+\nu$	$(11.25 \pm 0.20)\,\%$	
hadrons	$(67.60 \pm 0.27)\,\%$	
$\pi^+\gamma$	$< \ 8 \cdot 10^{-5}$	95%
$D_s^+\gamma$	$< 1.3 \cdot 10^{-3}$	95%
cX	$(33.4 \ \pm \ 2.6)\,\%$	
$c\bar{s}$	$31 \ +13 \ -11$	
invisible	$(1.4 \ \ \pm \ 2.8)\,\%$	

Table 3.1: Measured values for the branching ratios (Fractions) of the W boson decay modes [33].

40 GeV (roughly half the W boson mass). The undetected neutrino therefore leads to large $\not{P}_T$ in the event. A single isolated high P_T lepton is observed in the detector.[5] The P_T and θ distributions of the recoiling hadronic system in the event are shown in Figure 3.8. The hadronic system has typically low P_T and the proton remnant escapes down the beam-pipe (photoproduction). Above $P_T^{\text{jet}} = 80$ GeV the contribution to the total cross section is negligible. The P_T and θ of the W boson itself are shown in Figure 3.9. The P_T spectrum is very similar to that of the recoiling hadronic system and peaks at low values. Though the heavier W boson is generated much more forwardly than the jet.

3.5 W Boson Polarisation Fractions

The W boson is a vector particle in the SM and can have three different polarisations 1,-1, and 0, corresponding to the W boson spin, aligned, opposite, and orthogonal to the momentum direction, respectively. The W boson is said to be right (left) handed, if its polarisation is 1 (-1). When the polarisation is 0 the W boson is said to be longitudinally polarised. The fraction of the total production cross section, represented by W bosons with a particular polarisation is called a *polarisation fraction*. The measurement of the W boson polarisation fractions at HERA makes use of the W boson decay angle θ^* in the decay $W \to e/\mu + \nu$.[6] The decay angle θ^* is defined as the angle between the W boson momentum direction in the laboratory frame and that of the charged decay lepton in the W boson rest frame. For the left handed polarisation fraction F_-, the longitudinal fraction F_0 and the right handed fraction $F_+ \equiv 1 - F_- - F_0$, the $\cos\theta^*$ distributions for W^+ bosons are given by [32]

$$\begin{aligned} \frac{d\sigma_W}{d\cos\theta^*} &\propto (1 - F_- - F_0) \cdot \frac{3}{8}(1 + \cos\theta^*)^2 \\ &+ F_0 \cdot \frac{3}{4}\left(1 - \cos^2\theta^*\right) \\ &+ F_- \cdot \frac{3}{8}(1 - \cos\theta^*)^2 . \end{aligned} \tag{3.12}$$

In the decay of W^- bosons, the charged decay leptons are the antiparticles of those in the W^+ decay. As a result, both the produced neutrino and the charged lepton will have opposite handedness due

[5] In approximately 25% of the cases, the scattered electron is also observed in the detector.
[6] The contribution from the decay $W \to \tau\,(\to e/\mu + \nu) + \nu$ is not included.

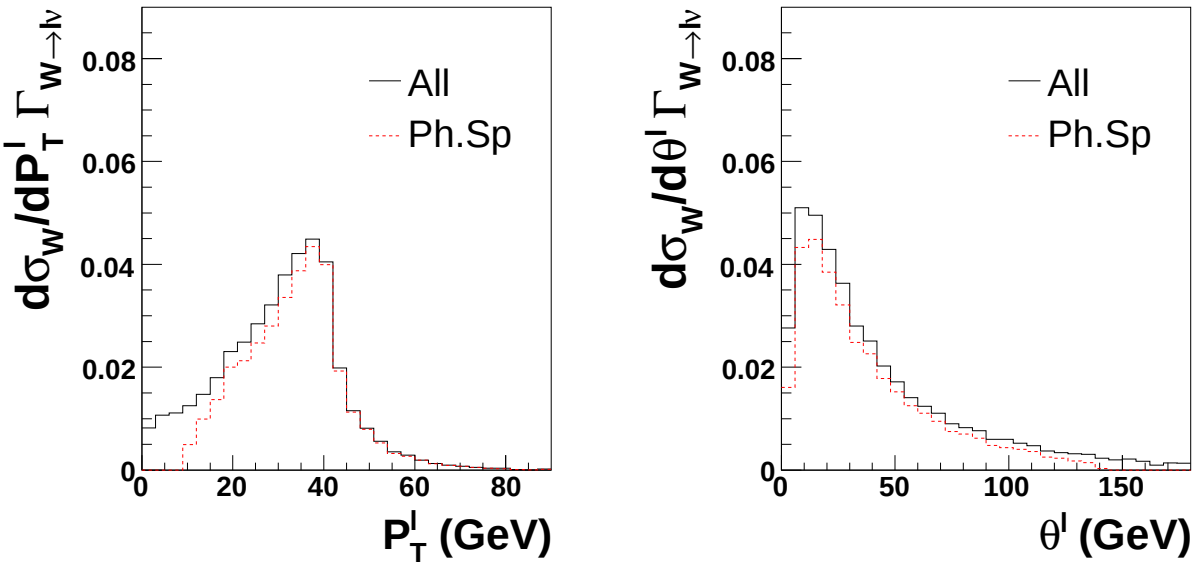

Figure 3.6: *P_T and θ distributions of the charged lepton in the decay $W \to \ell\nu$ from the EPVEC generator in the full phase space (continuous line) and in the detection phase space (dotted line).*

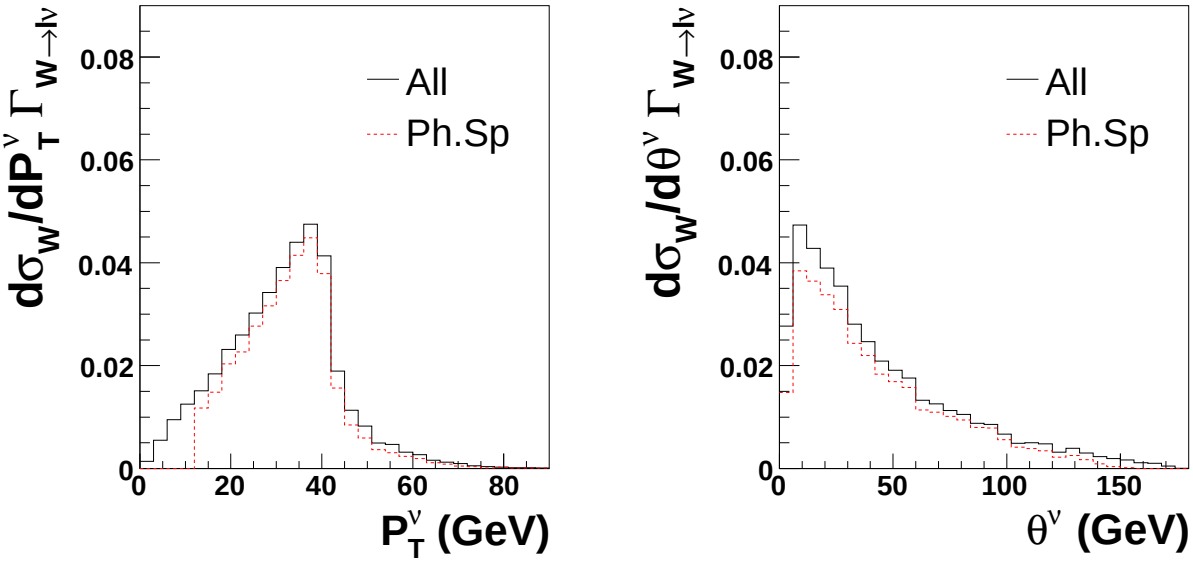

Figure 3.7: *P_T and θ distributions of the neutrino in the decay $W \to \ell\nu$ from the EPVEC generator in the full phase space (continuous line) and in the detection phase space (dotted line).*

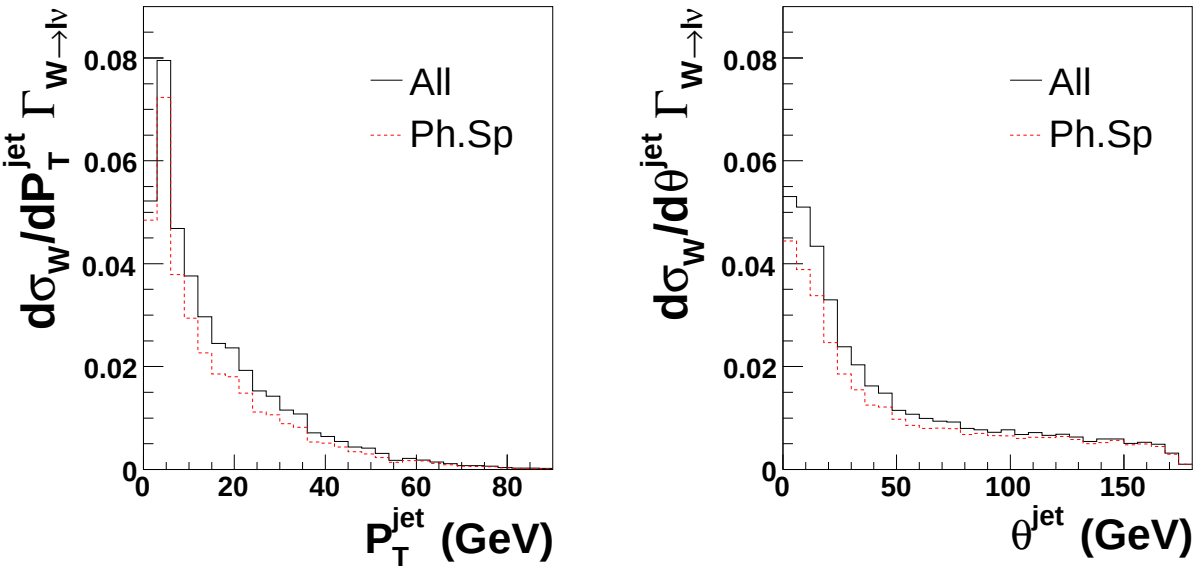

Figure 3.8: *P_T and θ distributions of the jet (X) in the process $ep \to eWX$ from the EPVEC generator in the full phase space (continuous line) and in the detection phase space (dotted line).*

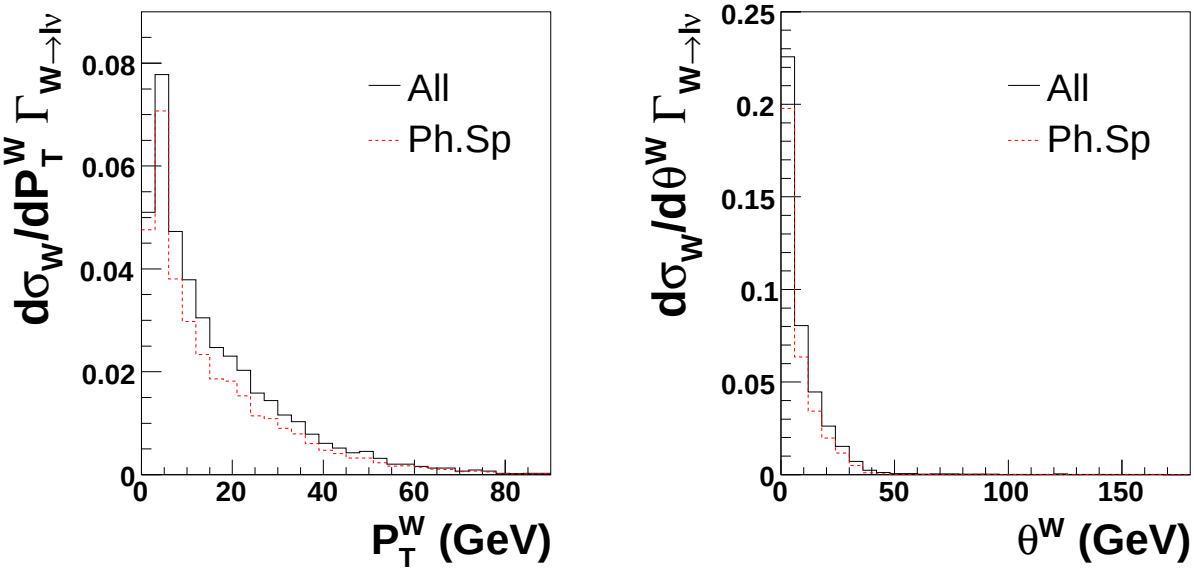

Figure 3.9: *P_T and θ distributions of the W boson in the process $ep \to eWX$ from the EPVEC generator in the full phase space (continuous line) and in the detection phase space (dotted line).*

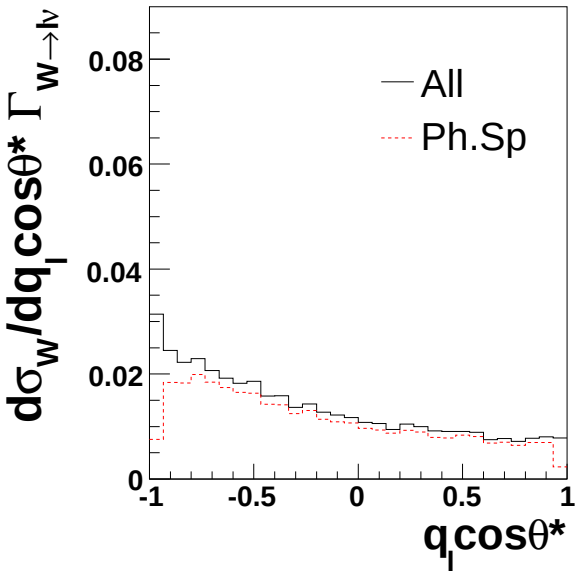

Figure 3.10: *The $q_\ell \cos\theta^*$ distributions of the W boson in the process $ep \to eWX$ from the EPVEC generator in all phase space (continuous line) and in detection phase space (dotted line).*

to the V-A structure of the coupling. Conservation of angular momentum implies therefore that the $\cos\theta^*$ distribution of left handed W^- bosons is identical to that of right handed W^+ bosons and vice versa. To allow for the combination of events containing W^+ and W^- bosons, $\cos\theta^*$ is weighed with the sign of the lepton charge $q_\ell = \pm 1$.

bin:	1	2	3	4	5	6
Cor.Fac.	-0.053	-0.005	0.007	0.027	0.031	0.107

Table 3.2: *Correction factors (Cor.Fac) per bin to apply to the differential single W boson cross section as a function of $q_\ell \cos\theta^*$ to account for the contribution from off-shell W bosons. Estimated with EPVEC. The statistical error on these numbers in each bin is $< 1\%$.*

The $q_\ell \cos\theta^*$ distributions in both the full phase space and the detection phase space are shown in Figure 3.10. Since the W boson direction of flight is mainly forward, as can be seen from Figure 3.9, the charged leptons, which are emitted with $\cos\theta^* \simeq -1$, are prone to escape detection. The differential cross section for given W^+ polarisation can be obtained by projecting the events containing a W^+ onto the moments $(1 \pm \cos\theta^*)^2$ and $\left(1 - \cos^2\theta^*\right)$. This is done by weighing each event with the expectation values $\frac{1}{2}\left(1 \pm 2\cos\theta^* + \cos^2\theta^*\right)$ and $2 - 5\cos^2\theta^*$ for the respective moment [32].

The W bosons from the Feynman diagrams 3.1 (f)-(g) are off-shell. For this reason their polarisation behaviour is not expected to be described by Equation (3.12). The effect of such events on the $q_\ell \cos\theta^*$ distribution, is illustrated on the right hand side of Figure 3.11 and is quantified in Table 3.2. The values in the table are used to correct the data. In the figure, the polarisation fractions in SM W boson production are compared to those of another process, where W bosons are generated via single

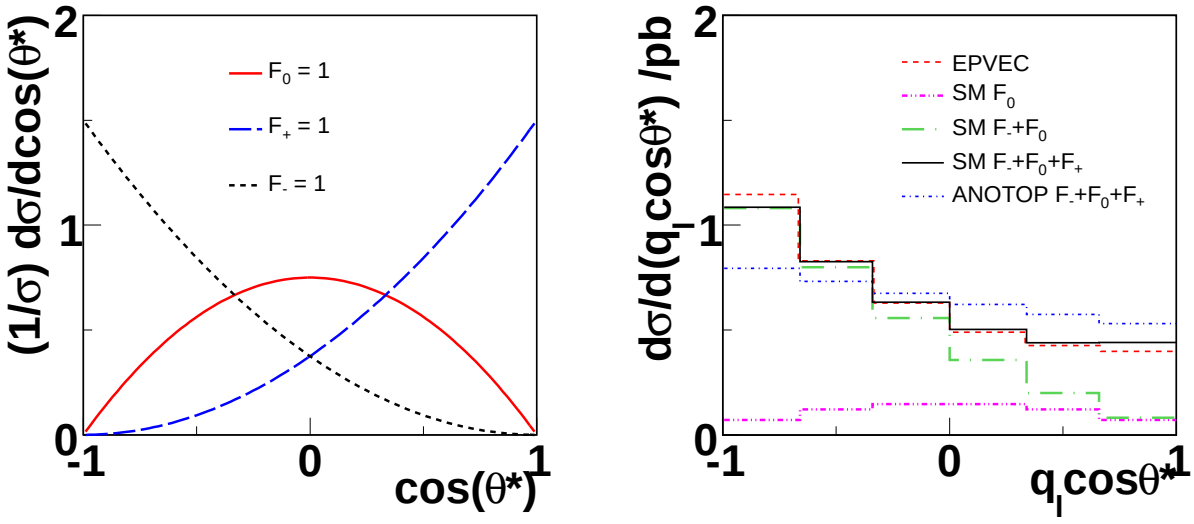

Figure 3.11: *Left: Normalised $d\sigma/d\cos\theta^*$ for each W^+ polarisation. Right: EPVEC generated $q_\ell \cos\theta^*$ distribution (for on- and off-shell W bosons) vs. the SM theoretical prediction for on-shell W's normalised to EPVEC. Also shown for ANOTOP using on-shell W bosons only.*

	ON-SHELL ONLY		ON- AND OFF-SHELL	
Fraction	**EPVEC**	**ANOTOP**	**EPVEC**	**ANOTOP**
F_-	0.611 ± 0.010	0.375 ± 0.008	0.645 ± 0.008	0.373 ± 0.007
F_0	0.172 ± 0.011	0.410 ± 0.012	0.124 ± 0.009	0.409 ± 0.010
F_+	0.217 ± 0.006	0.214 ± 0.007	0.231 ± 0.005	0.218 ± 0.006

Table 3.3: *The polarisation fractions for the SM (EPVEC) and anomalous single top (ANOTOP) calculated for on-shell W bosons only (left two columns) and for both on- and off-shell W bosons (right two columns). The errors are statistical.*

top production in the ANOTOP [36] framework (Section 2.3.3).[7] Table 3.3 shows the results for on-shell W bosons only, and for both on and off-shell W bosons. The ANOTOP values are significantly different from those of the SM. This is due to the different production mechanisms involved and demonstrates that the polarisation behaviour of the W boson provides a probe for the underlying production mechanism. Deviating values of the W boson polarisation fractions thus not only indicate new physics, but also allow to assess its nature.

A qualitative understanding of why single W bosons at HERA are predominantly left handed can be obtained by deriving approximate forms of the $ep \to eW^\pm X$ production amplitudes in the Weizsäcker-Williams approximation (WWA) [13]. As mentioned above, in the WWA the W boson decay is ignored. The quark masses are also ignored, which are therefore always left handed due to the V-A structure of the $Wq\bar{q}$ coupling.

The effective Lagrangian (3.5) leads to cross section formulas for the single W boson production

[7] All generators are discussed in Section 4.4.

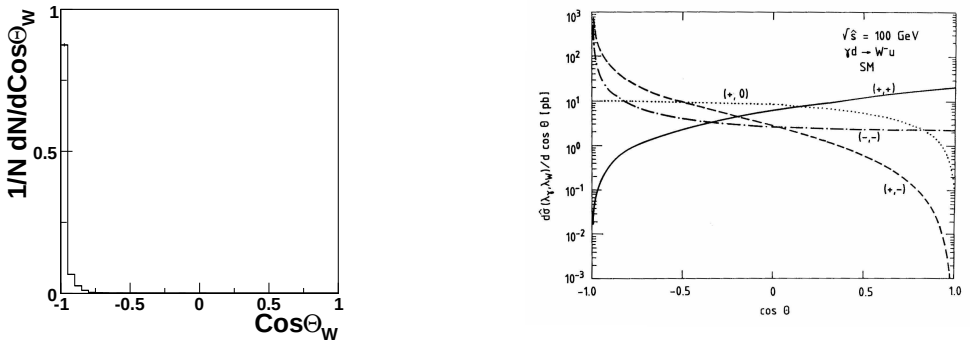

Figure 3.12: *Left: Distribution of the cosine of the polar angle of the generated W boson with respect to the incoming electron beam for on- and off-shell W bosons. Right: Angular distributions* $d\sigma\left(\lambda_\gamma, \lambda_W\right)/dcos\Theta$ *for polarisation* λ *in the SM process Shown in parenthesis are the photon and W boson polarisations in the* γd *centre of mass frame. From Ref. [13].*

and decay process, including the anomalous $WW\gamma$ coupling. In the WWA, with the polarisation amplitudes denoted by $\mathcal{M}_{\lambda_\gamma,\lambda_W}$, one can write

$$\mathcal{M}_{\lambda_\gamma,\lambda_W} = \frac{e^2}{\sqrt{2}\sin\theta_W}\frac{\hat{s}}{\hat{s}M_W^2}\sqrt{\beta}\mathcal{A}_{\lambda_\gamma,\lambda_W}, \tag{3.13}$$

where the polarisations λ can be +,-, or 0. Furthermore, $\beta = 1 - M_W^2/\hat{s}$, θ_W is the Weinberg mixing angle, and $\hat{s}$ denotes the square of the γq invariant mass. With all couplings set to their SM values, the reduced amplitudes $\mathcal{A}_{\lambda_\gamma,\lambda_W}$ in the γq centre of mass frame are for the $W^\pm$ production

$$\begin{aligned}
\mathcal{A}_{--} &= \mp 2\left[-\frac{2M_W^2}{\hat{s}}+2\right]\frac{\cos\frac{\Theta}{2}}{1-\beta_W\cos\Theta} + 2\left(e_q \mp 1\right)\left(1+\frac{M_W^2}{\hat{s}}\right)\frac{2\cos\frac{\Theta}{2}}{1+\cos\Theta},\\
\mathcal{A}_{-+} &= 0,\\
\mathcal{A}_{-0} &= 0,\\
\mathcal{A}_{+-} &= \mp\left[\frac{2M_W^2}{\hat{s}}\right]\frac{1-\cos\Theta}{1-\beta_W\cos\Theta}\cos\frac{\theta}{2} + \left(e_q \mp 1\right)\frac{2}{\beta W}\frac{M_W^2}{\hat{s}}\frac{1-\cos\Theta}{1+\cos\Theta}\cos\frac{\Theta}{2}, \qquad (3.14)\\
\mathcal{A}_{++} &= \mp 2\frac{1+\cos\Theta}{1-\beta_W\cos\Theta}\cos\frac{\Theta}{2} + \left(e_q \mp 1\right)\frac{2}{\beta_W}\cos\frac{\Theta}{2},\\
\mathcal{A}_{+0} &= 2\sqrt{2}\frac{M_W}{\sqrt{\hat{s}}}\left[\frac{1+\cos\Theta}{1-\beta_W\cos\Theta}+\frac{e_q \mp 1}{\beta_W}\right]\sin\frac{\Theta}{2}, \qquad (3.15)
\end{aligned}$$

where e_q is the charge of the incoming quark in units of e and Θ is the scattering angle of the W boson with respect to the incoming photon direction. β_W is defined as:

$$\beta_W = \frac{\hat{s}-M_W^2}{\hat{s}+M_W^2}. \tag{3.16}$$

Since at HERA the W bosons are produced at threshold $\hat{s} \sim M_W^2$ [13], $\cos\Theta \sim -1$, shown on the left hand side of Figure 3.12. Therefore $\mathcal{A}_{--}$ and $\mathcal{A}_{+-}$, in Eq. 3.14, become dominant due to their poles at $\cos\Theta = 1$. This explains why the W bosons are predominantly left handed at HERA.

4 HERA and the H1 detector

4.1 The HERA storage ring

The Hadron Elektron Ring Anlage (HERA) at the Deutsches Electron Synchrotron (DESY) is located in Hamburg, Germany. The construction started in 1984 and the first data was recorded in 1992. Figure 4.1 shows the facility. HERA accelerates protons and electrons in two vacuum beam-pipes over a length of 6.3 km. The protons are brought to collision head-on with the electrons at two points along the ring, inside the H1 and ZEUS hermetic detectors. The two other experiments, HERMES [37] and HERA-B [38], use only one of the beams. The protons start as negative hydrogen ions and are injected via a proton linear accelerator into PETRA. There they are further accelerated to an energy of 40 GeV and injected into HERA. They reach an energy $E_p = 820$ GeV (in the years 1994-1997) or 920 GeV (1998-2007). The electrons or positrons follow much the same scheme. They start off in a linear accelerator. Then they are accelerated further in PETRA and finally injected into HERA where they reach an energy $E_e = 27.5$ GeV. The available centre-of-mass energy of the ep collisions is thus

$$\sqrt{s} \simeq \sqrt{4E_eE_p} = \sqrt{4 \cdot 27.5 \cdot 820\,(920)} = 300\ (320)\ \text{GeV}. \tag{4.1}$$

The particles are accelerated by a RF voltage. The wells of low potential, caused by the RF voltage along the beam-pipe, are called 'buckets', which contain colliding bunches of electrons and protons. 210 buckets can be filled with bunches of electrons or protons. Consecutively filled buckets collide the bunches at a time interval of 96 ns. Usually some buckets contain only an electron or a proton bunch. These are called 'pilot bunches', which are used to monitor beam-gas interactions.

The total number of collisions at the bunch crossing is determined by the 'luminosity' L, which is the proportionality factor between the interaction rate dN/dt and the cross section σ

$$\frac{dN}{dt} = L \cdot \sigma. \tag{4.2}$$

Therefore the total number of events depends on the integrated luminosity $\int L\,dt$. The cross section σ has the dimension of length squared and is usually specified in barn (b), whereby $1\ b = 10^{-28}\ m^2$. Accordingly, the integrated luminosity is measured in units of inverse barn.

In 1992, HERA started operation with electrons. In July 1994 positrons were used instead of electrons. Since then only in 1998 and 2004/2005 electrons were used. The period 1994-2000 is called the HERA I period. The HERA II period, 2002-2007, started after a major upgrade of HERA [39] where also the detectors underwent major upgrade programmes. A significant increase of the luminosity was obtained by installing new (quadrupole super conducting) magnets. In the last months of operation, the proton beam energy was lowered in order to measure F_L (Section 2.2) resulting in a lower luminosity. This can be seen from Figure 4.2 where the data taken by H1 since 1992 is shown. Additionally, spin rotators were installed allowing for longitudinal polarisation of the beam electrons and positrons.

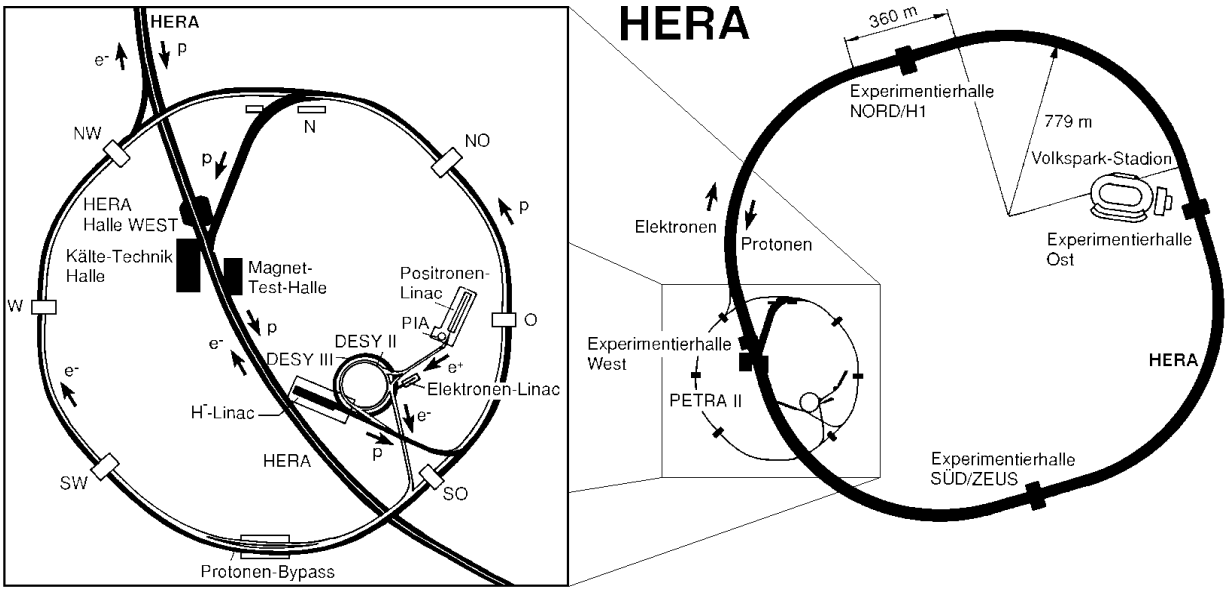

Figure 4.1: *The HERA collider with the main HERA storage ring (right) and the pre-accelerator facility (enlarged left).*

4.2 The H1 Detector

The H1 detector is designed to measure the complete final state of HERA *ep* processes, which contain charged electrons and muons, neutral photons and many charged and uncharged hadrons, mostly pions. Many subdetectors are required to meet the challenge to detect this variety of particles. This section presents the subdetectors that are most relevant to this analysis. The H1 detector, shown in Figure 4.3, is described in detail in Ref. [5].

The Cartesian coordinate system at H1 is defined as follows: the origin is placed at the nominal *ep* interaction point. The positive z-axis points in the direction of flight of the protons. The positive y-axis points upwards and the positive x-axis points toward the HERA centre. The polar angle θ is defined with respect to the positive z-axis and the azimuthal angle ϕ is defined with respect to the positive x-axis. The x-y plane is referred to as the transverse or azimuthal plane.

Since the protons carry more energy than the electrons in the *ep* collisions, most of the final state particles are found in the forward region (with positive z-coordinates) of the detector. The H1 detector is designed correspondingly.

4.2.1 Tracking

The H1 tracking system is displayed in Figure 4.4. It is referred to as the 'inner' tracking system because it is completely contained within the magnetic field of 1.16 Tesla of the central part of the super conducting coil. The 'outer' tracking system, also called the muon system, is described later in this chapter. The angular coverage of the inner trackers is $7^o < \theta < 165^o$. Drift chambers and proportional chambers are used to track the path of charged particles, which are forced along curved trajectories by the magnetic field. The radius of the trajectory in the transverse is proportional to the particle's transverse momentum and inversely proportional to its charge.

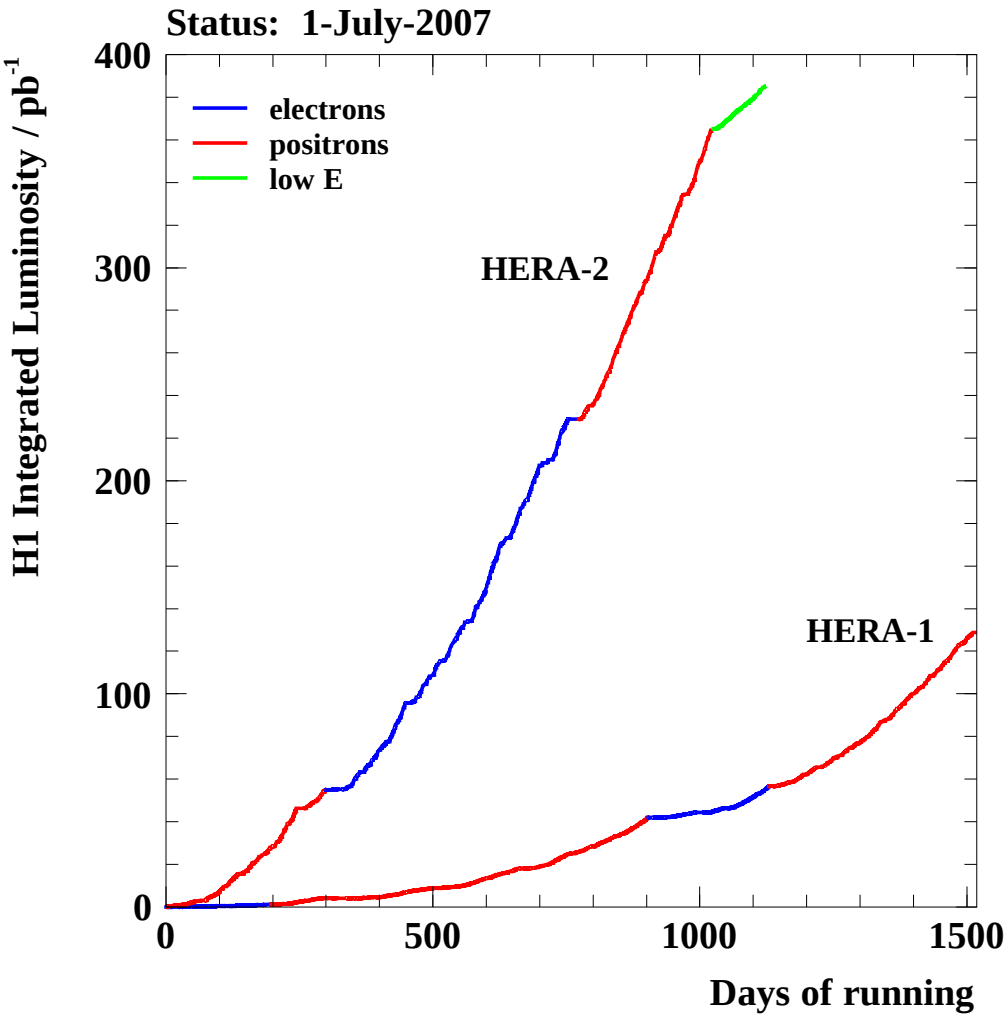

Figure 4.2: *Recorded luminosity by H1 as a function of the days of running since the data taking operation started. The vast increase of luminosity after the upgrade of HERA I to HERA II and the large increase of e^-p data in the HERA II data set are clearly visible.*

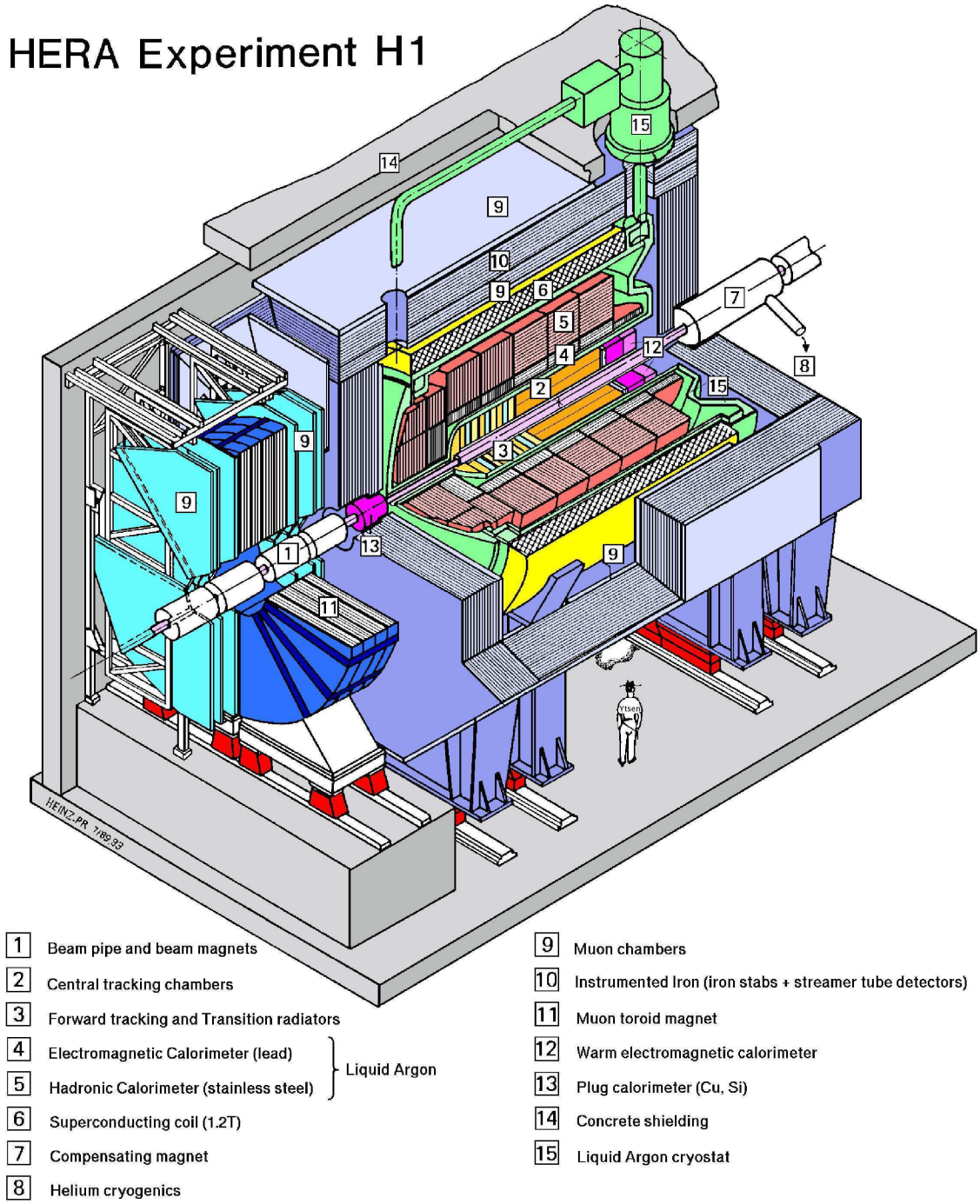

Figure 4.3: *The H1 detector and its major components. The protons come from the right and the leptons from the left. They are brought to collision in the interaction point, inside the central tracking chambers [2].*

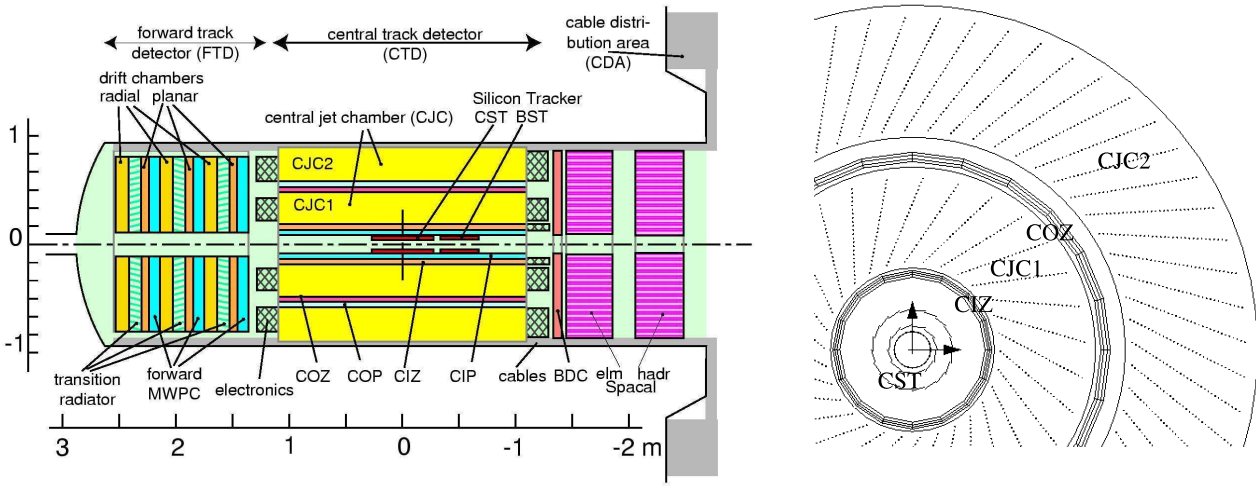

Figure 4.4: *Left: The H1 inner tracking system. The electromagnetic and hadronic parts of the SPACAL are also shown. They are located at the right of the CTD. Right: Transverse view of the CTD. The wires in the CJCs are strung parallel to the z-axis and are shown as dots.*

The system is divided in the central track detector (CTD) and forward track detector (FTD). In the center near the interaction point are the central and backward silicon trackers (CST and BST). Additional tracking information is provided by the backward drift chamber (BDC). During the upgrade a new forward silicon tracker was installed for better tracking close to the interaction point.

The Central Track Detector

The CTD covers the angular range $15^o < \theta < 165^o$. A transverse view is provided in the right plot of Figure 4.4. Since the HERA II upgrade, silicon detectors are located close to the interaction point at 5 to 10 cm. These are used for measuring the primary vertex and better track measurement.

The large central jet chambers (CJC1 and CJC2) are the main components of the inner tracking system. Their angular coverage is $10^o < \theta < 170^o$. Their wires are strung parallel to the z-axis and allow for measuring the hit coordinates of a charged particle with a resolution of 0.170 mm in the transverse plane and 2.2 cm in the z-direction. From the curved trajectory of charged particles the transverse momentum can be determined with a resolution $\sigma_{P_T}/P_T = 0.005 \oplus 0.015$ GeV^{-1} [40].

The central inner (CIZ) and central outer (COZ) z-chambers surround the inner half of the CJC. Their wires are strung in the $r-\phi$ plane, concentrically around the beam axis, allowing for an accurate measurement of the z-coordinate. The Central Inner Proportional Chamber (CIP) and Central Outer Proportional (COP) are multi-wired proportional chambers (MWPC). For HERA II they were replaced by the 'CIP2k', an improved version of the CIP. They surround, like the z-chambers, the inner half of the CJC with an angular coverage of $11^o < \theta < 169^o$. The MWPCs have a high wire density with a small drift time allowing for fast triggering.

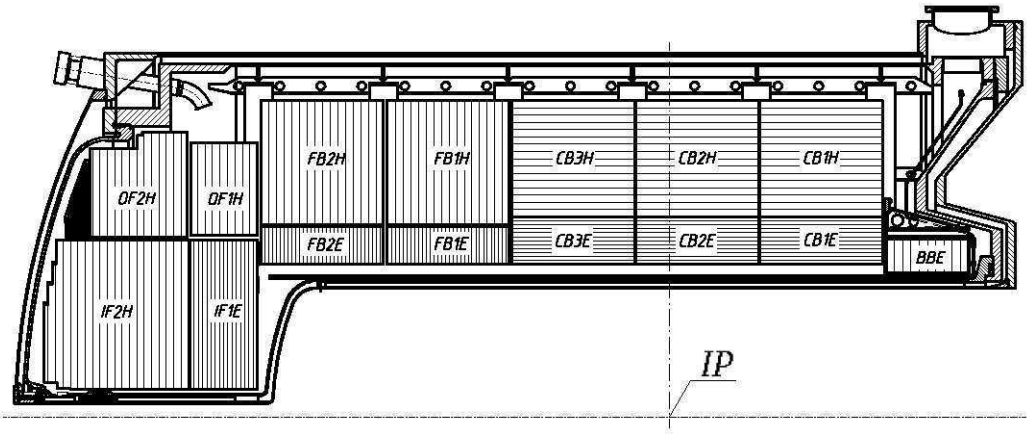

Figure 4.5: *Schematic longitudinal view of the LAr. Shown is only one of the two symmetric halves. The interaction point is marked with IP.*

The Forward Track Detector

The forward track detector (FTD) consists of a set of drift chambers with wires strung perpendicular to the beam axis. The angular region covered by the FTD is $5^o < \theta < 25^o$. The FTD was rebuilt for HERA II to include five new drift chambers. The Forward MWPCs, used for fast triggering, are placed between the drift chambers. The design resolution for the FTD is $\sigma_P/P^2 = 0.003$ GeV. The angular resolution is 1 mrad[41].

4.2.2 Calorimetry

The main calorimeters are the liquid argon (LAr) and the spagetti calorimeter (SPACAL). Both consist of an electromagnetic (EMC) and hadronic (HAC) part.

The LAr, schematically shown in Figure 4.5, is a non-compensating calorimeter. It covers the polar region $4^o < \theta < 154^o$ and all of the azimuthal region. It is divided along the beam axis in eight wheels, each of which is segmented in ϕ into eight identical stacks or octants. The inner part of each wheel is part of the electromagnetic calorimeter and the outer part is part of the hadronic calorimeter. The stainless steel (epoxy-glass fiber) sampling plates in the hadronic (electromagnetic) calorimeter are shown as thin lines in the wheel segments and are 5 to 8 interaction (20 to 30 radiation) lengths thick A traversing particle principally interacts with the sampling material invoking a shower of secondary electrons creating ionisation in the narrow gaps of liquid argon. The ionisation electrons drifting in the electric field provide the signal from readout cells inserted between the sampling plates to obtain high granularity.

The electromagnetic energy resolution, as measured with a test beam, is $\sigma_E/E = 12\%/\sqrt{E} \oplus 1\%$ and for hadronic showers $\sigma_E/E = 50\%/\sqrt{E} \oplus 2\%$. In addition, the timing information from the LAr is used to check whether the energy deposits correspond to the bunch crossing time T_0. Particles that punched through the calorimeter are detected by the tail catcher on the inside of the iron return yoke (instrumented iron).

The SPACAL is a led-scintillator spagetti calorimeter, located in the rear (Figure 4.4). It covers the angular region $153^o < \theta < 177.5^o$ and it provides fast signal response time and an energy resolution of

$\sigma_E/E < 10\%$ (electromagnetic). The angular resolution is less then 1 mrad. Its main function is to catch the scattered electron in low Q^2 analyses.

4.2.3 Time of Flight System

The rate of events from non-ep processes is much higher than that of ep processes and is mostly related to the proton beam. About 75% of these processes occur outside a narrow time window around the bunch crossing time T_0. Information from the time of flight system, ToF, is used to reduce non-ep background contributions by measuring the event timing relative to T_0. The ToF system is comprised of three seperate scintillators located close to the beam and the 'Veto Wall', located behind the iron yoke to detect Halo muons. Additionally, timing information from the SPACAL is used.

4.2.4 Luminosity Monitoring System

The luminosity delivered by HERA at H1 is measured by observing the rate of bremsstrahlung events $ep \rightarrow ep\gamma$ of which the cross section is well known. The photons are measured by the Electron Tagger and the Photon Detector, both of which are Cherenkov calorimeters. The design accuracy on the luminosity measurement is 1.5-2%. The preliminary systematic uncertainty used in this work on the luminosity is 4%.

4.2.5 Muon Detectors

Muons are minimum ionising particles and as such they pass through the calorimeter depositing only little energy. They are detected by the forward muon detector (FMD) and the central muon detector (CMD or 'instrumented iron'), which cover the angular ranges of $3^o < \theta < 17^o$ and $5^o < \theta < 175^o$, respectively. The CMD has a poor momentum measurement resolution and serves mainly as a muon tagger. Muons in the central region are therefore measured by the CTD. Tracks from the FTD or CTD are referred to as 'inner tracks' while tracks from the muon system are called 'outer tracks'. The FMD measures the muon momentum with a resolution of $\sigma_P/P = 0.24 - 0.36$ for $P = 5 - 200$ GeV.

4.2.6 Triggering

The variety of physics processes in ep collisions covers a wide range of event rates. It extends from non-ep beam-gas interactions at $\sim$50 kHz and cosmic muons at 700 Hz, via photoproduction in ep scattering with a cross section of several μb and a rate of 20-30 Hz, towards the single W boson production process, expected to occur a few times a week. With the total event rate of $\sim$50 kHz, a four-step triggering system is employed that reduces this to a data logging rate of 10-25 Hz. The first level trigger, L1, consists of hardware triggers, the output of which is combined into so called subtriggers. Subtriggers can be prescaled if the event rate of the corresponding processes are too large. If a subtrigger has prescale factor n, only every n^{th} event for which this subtrigger fires is accepted. Most triggers for the high P_T analyses, however, are not prescaled. The L1 output event rate is 1 kHz. The second trigger level, L2, starts the readout. It makes use of topological information of the event and reduces the event rate to less than 200 Hz. The third trigger level L3, starts the event building. The computing power for the L3 trigger was upgraded for HERA II. The level three trigger makes decisions based on detailed tracking information and reduces the event rate further to 50 Hz. The fourth level trigger, L4, runs on a farm and receives the raw data of the full event as a basis for its decision making algorithms. This allows for online trigger selections with the full intrinsic detector

resolution. The output is stored on tape for off-line analysis at an event rate of 10-25 events per second.

4.3 Detector Simulation and Analysis Software

The detector is simulated with the H1SIM program, in the GEANT framework [42]. The reconstruction of the simulated events proceeds in the same way as for the data. The output is stored in BOS (Bank Object Storage) format from which all information can be accessed during off-line analysis. The analysis platform used in this thesis is based on H1OO (H1 Object Oriented) [43], which is the H1 software, written in C++, operating in a ROOT [44] environment.

4.4 Monte Carlo Generators

As mentioned in Section 3.2, the signal contribution from single W bosons is calculated with the LO EPVEC generator in a NLO reweighing scheme (Section 3.2). This generator is also used to calculate the contributions from Z boson production, albeit without any NLO corrections. To calculate the DIS and diffractive contributions from NC and CC events to $\ell+\not{P}_T$ events, the LO generators RAPGAP [45] and DJANGO [46] are used.[1] The LO generator GRAPE [47] is used to calculate contributions from Lepton Pair (LL) processes. Contributions from electron (muon/tau) pair production are abbreviated in this work by EE (MM/TT). When only the total contribution from lepton pair production is given, the abbreviation LL is used. The small background contributions to $\ell + \not{P}_T$ events coming from bremsstrahlung are included in this work using the generator WABGEN [48]. The elastic case, were the outgoing hadronic final state X consists merely of the proton p is included in the WABGEN calculations. The abbreviation used in the figures for this process is EG (from 'e-gamma'). Calculations for the anomalous single top production process via FCNC are done with the generator ANOTOP [36], where the LO matrix elements are obtained from the CompHEP program [49].

[1] The choice of the generator depends on the available statistics and the description of the data. Both can differ per dataset.

5 Particle Identification and Event Reconstruction

Reconstructing the full event final state from the detector output commences with identifying isolated electrons and muons. The non-isolated leptons are assumed to originate from hadronic decays and are included in the hadronic final state (HFS). Tracks are combined with clusters to reconstruct charged hadron candidate particles and the remaining energy is attributed to neutral hadrons. The identified hadronic final state particles are combined into jets after which the energy scale of electrons and hadrons is calibrated. The fully reconstructed and calibrated event final state is used to determine global topological event variables.

5.1 Track Reconstruction

The measurement points in the Central Track Detector (CTD) are fit to a helix hypothesis and the obtained parameters are used to reconstruct the kinematics of the charged particle. In addition, a track can be fit to the beam spot in the transverse plane, improving the precision of the momentum measurement. The track segments are required to originate from a vertex, which is determined from the common point of origin of the largest part of all track segments in the CJC. Tracks are classified as 'good' when the requirements listed in Table 5.1 are satisfied. The charge of the particle is determined from the curvature of the track.

P_T^{track}	> 70 MeV
DCA	$< 2/\sin\theta^{\text{track}}$ cm
R_{start}	< 50 cm
R_{length}	> 5 cm (> 10 cm if $\theta^{\text{track}} < 150^o$)

Table 5.1: *Track requirements for 'good' tracks.* DCA *is the distance of closest approach to the vertex in the transverse plane,* R_{start} *is the track radius at its start and the track length is denoted by* R_{length}.

5.2 Electron Identification

Compact and isolated energy clusters of cells in the LAr are identified with electromagnetic particles. The energy deposition in each cluster must be larger than 2 GeV of which at least 90% must be found inside the LAr and at least 50% in the electromagnetic part of it. Neighbouring clusters can be merged to the primary electron cluster by defining the electron 'envelope' as a cone of 7.5^o around the vertex-cluster axis. This axis connects the event vertex and the cluster bary-centre in a straight line and starts at 1 m from the event vertex and is truncated at the end of the first hadronic layer. The clusters are merged if more than 50% of their energy is inside the electron envelope.

An electron is identified when 98% of the total cluster energy is located within a cone with radius 0.25 in $\eta - \phi$ space around the vertex-cluster axis. A fraction of 95% is allowed if the hadronic energy in the isolation cone is less then 300 MeV. The four vector of the electron is defined by the cluster's energy and location. The resulting electron must have $P_T >$ 3 GeV and an energy $>$ 5 GeV and the cluster must have at least three cells. A track is 'linked' to the cluster when the distance of closest approach of the track to the cluster bary-center is less than 12 cm. The track linking efficiency is better than 97%. Latter is determined from the ratio between two samples of NC events where in one sample a linked track is required for the electron in the event and in the other not. The closest linked track to the cluster is associated to the electron. The polar angle θ^e is known to 3 mrad in the LAr and 1 mrad in the SPACAL. The azimuthal angle ϕ^{e} has an uncertainty of 1 mrad [50]. The electron is isolated against hadrons if 95% of the electron energy is found in a cone of radius 0.5 in $\eta - \phi$ space around the vertex-cluster axis.

For electrons in the SPACAL a different algorithm is used. The energy deposit should be larger than 5 GeV and the radius of the cluster, which is attributed to the electron, should be smaller than 4 cm.

5.3 Electromagnetic Energy Calibration

The energies and angles of isolated electrons are measured in the Liquid Argon Calorimeter (LAr). The angular measurement from LAr clusters is adjusted with respect to the angular measurement of the internally aligned CTD. In order to do this, high Q^2 NC events are used where the scattered electron traverses both the central tracking system and the LAr. The electromagnetic energy calibration procedure is described in [51] and only briefly discussed here. Clusters consist of cells in which the energy deposit is larger than the threshold (noise) value of 300 MeV. The cell is defined to be electromagnetic or hadronic, depending on whether the dominant contribution of the cell energy is found in the electromagnetic or hadronic part of the calorimeter. The energy scale of the clusters is corrected for the non-compensating nature of the calorimeter and for dead material. The LAr is calibrated using the so-called 'NC DIS at high Q^2' method and done for each data taking period. The procedure uses NC DIS events of which the kinematics are over-constrained. The momentum of the scattered electron and the jet are balanced in the azimuthal plane and the incoming (beam) energies are precisely known. As a result the measured values for the angle of the scattered electron θ_e and that of the hadronic system γ_h can be used to calculate the electron energy E_{DA} in the 'Double Angle Method'

$$E_{DA} = \frac{2E_e \sin\gamma_h}{\sin\gamma_h + \sin\theta_e - \sin\left(\gamma_h + \theta_e\right)}, \tag{5.1}$$

which is used to calibrate the measured value. The resulting accuracy on the energy scale is 1% in the central and 2% in the forward region, depending on the statistical precision of the data.

5.4 Muon Identification

The Central Muon Detector (CMD) and the Forward Muon Detector (FMD) measure outer tracks that can be linked to inner tracks from the central jet chambers. The minimum ionising muons create characteristic signals in the calorimeter along the muon trajectory, which can be detected. In order of decreasing quality, five muon types are distinguished:

1. An inner and outer track are linked.

2. As Grade 1 muons, but with less strict linking requirements.

3. An inner track is matched to a track segment or energy deposit in the instrumented iron.

4. A muon signature is detected in the calorimeter.

5. Only an outer track is present.

The muon is isolated against hadrons when the LAr energy in a cylinder around the extrapolated muon track is less than 8 GeV. The cylinder has a radius of 35 cm in the electromagnetic part of the LAr and a radius of 75 cm in the hadronic part. The track, associated to the muon, must be isolated from all 'good' tracks in the event (Section 5.1) by at least 0.5 in $\eta - \phi$ space. The over-all muon finding efficiency is greater than 90%. The uncertainty on the finding efficiency is 15% in the forward region $5^o < \theta < 15^o$ and 5% in the region $\theta^\mu > 15^o$ [52].

5.5 Reconstruction of the Hadronic Final State

The Hadronic Final State (HFS) is defined as the total of all final state particles, excluding identified isolated leptons. The HFS particles are reconstructed using the Hadroo2 algorithm [53]. The energy of a HFS particle is determined from the curvature of its track or from the energy deposition in the calorimeter. A calibration is only applied to HFS particles reconstructed using the calorimeter, as the particles reconstructed using track information are already at the right energy scale. Once the electromagnetic energy measurement from the LAr (EMC) is established, it is used to calibrate the hadronic energy scale using an intrinsically balanced NC DIS sample where the electromagnetic energy equals the hadronic energy.

For the reconstruction of jets, an inclusive k_T clustering algorithm is used [54] that combines uncalibrated final state particles into jets. The jet polar angle, $\theta^{\rm jet}$, is known to 5 mrad for $\theta^{\rm jet} < 20^o$ and 10 mrad elsewhere and the azimuthal angle $\phi^{\rm jet}$ has an uncertainty of 1 mrad [55]. The jets have a minimum P_T of 2 GeV and are reconstructed in the angular range $5^o < \theta < 170^o$ and have a jet radius $\mathrm{R_{jet}} < 0.1$ in $\eta - \phi$ space. The jet energy scale is known to 2% in the LAr ($\theta^{\rm jet} < 155^o$) and to 7% in the SPACAL for jets with $P_T^{\rm jet} \geq 8$ GeV. The uncertainty on the energy scale for jets with lower P_T is 5% [56].

5.6 List of Observables in the Event

This section summarises all relevant kinematic quantities in the event, which are referred to throughout this thesis.

- θ^ℓ Lepton polar angle as measured by the calorimeter.
- $D^{\rm jet}$ Minimum distance between a lepton (ℓ) and a jet in the event in $\eta - \phi$ space

$$D^{\rm jet} = \sqrt{(\eta_\ell - \eta_{\rm jet})^2 + (\phi_\ell - \phi_{\rm jet})^2}. \tag{5.2}$$

- $E - P_Z$ Energy and longitudinal momentum balance of the final state.

- $\delta_{\mathbf{miss}}$ The imbalance of energy and longitudinal momentum in the final state

$$\delta_{\text{miss}} = 2E_b - (E - P_Z), \tag{5.3}$$

where E_b is the energy of the incoming beam electron.

- $\Delta\phi_{\ell-X}$ Acoplanarity, defined as the opening angle between the isolated lepton, ℓ, and the recoiling hadronic system, X, in the transverse plane.

- M_T Transverse mass in the event, obtained by projecting the P_T of the isolated lepton and $\not{P}_T$ onto the transverse plane $M_T = \sqrt{\left(|\bar{P}_T^{\ell}| + |\bar{\not{P}}_T|\right)^2 - \left(\bar{P}_T^{\ell} + \bar{\not{P}}_T\right)^2}$.

- $\not{P}_T$ Missing transverse momentum in the event. Calculated using all reconstructed particles (rec) in the event $\bar{\not{P}}_T = -\bar{P}_{T,\text{rec}}$.

- P_T^X Transverse momentum of the hadronic system X.

- $P_T^{\mathbf{calo}}$ Uncalibrated total transverse calorimetric energy. The trigger decision is based on this quantity. In this analysis, only events with $P_T^{\text{calo}} > 12$ GeV are considered due to the low trigger efficiency at lower transverse momentum. It is calculated using the HFS particles after the jet finding procedure. In the case of an isolated minimum ionising muon in the event, $P_T^{\text{calo}} \simeq P_T^X$.

- P_T^{ℓ} Lepton transverse momentum as measured by the calorimeter.

- Q^2 Virtuality of the event. The negative invariant mass of the exchange boson. It is calculated with the 'electron method' [57], where the electron is the scattered electron

$$Q^2 = 4E_b E_s \cos\left(\theta^e/2\right). \tag{5.4}$$

Here, E_b is the energy of the incoming (beam) electron and E_s the scattered electron with polar angle θ^e.

- σ_Q Charge significance, a measure for the accuracy of the measurement of the curvature κ of a track

$$\sigma_Q = \frac{|\kappa|}{d\kappa} \tag{5.5}$$

where $d\kappa$ is the uncertainty on κ.

- V_{ap}/V_p 'Vratio', a measure of the azimuthal balance in the event where

$$V_{ap} = -\sum_i \frac{\bar{P}_T^X \cdot \bar{P}_{T,i}}{P_T^X} \quad \text{for} \quad \bar{P}_T^X \cdot \bar{P}_{T,i} < 0 \tag{5.6}$$

$$V_p = \sum_i \frac{\bar{P}_T^X \cdot \bar{P}_{T,i}}{P_T^X} \quad \text{for} \quad \bar{P}_T^X \cdot \bar{P}_{T,i} > 0 \tag{5.7}$$

V_{ap} and V_p are the transverse energy flow anti-parallel and parallel to $\bar{P}_T^X$. The sum is over the P_T components of all particles in the final state using the energy deposits in the clusters only. Processes containing particles that are not detected generally have small values of V_{ap}/V_p. V_{ap}/V_p is known to 2% in this analysis [11].

- ζ Defined analogously as Q^2, but the electron is assumed to come from the W boson decay. For NC events, ζ is identical to Q^2, but for W boson production events it behaves differently and is used to separate between these processes [11].

6 Event Selection

This chapter describes the analysis event selection. The first part explains the preselection that is used to obtain a good quality physics sample from the collected data. Then the selection of events with an energetic isolated electron (e) or muon (μ) and large missing transverse momentum ($\not\!\!P_T$) is presented. These events are referred to as $\ell + \not\!\!P_T$ events. The previously by H1 reported 'excess' of observed events over the SM prediction in the region of phase space where $P_T^X > 25$ GeV is discussed [11]. More details on the full $\ell + \not\!\!P_T$ analysis can be found in Ref. [20].

6.1 General Data Preselection

6.1.1 Run Selection

The data taking during a HERA 'fill' (defined by the time during which a proton beam is present) consists of a series of '(H1) runs' for which the luminosity is individually measured. The detector status is rather stable during a run but may differ between runs.

The runs are preselected here mainly by High Voltage (HV) requirements of subdetectors, which means not only that those subdetectors were operating during the run, but also the relevant read-out branches were in operation. This is required for the following detectors: Central Jet Chambers (CJC), liquid argon calorimeter (LAr), spaghetti calorimeter SPACAL, time-of-flight system (ToF), Luminosity system, and Central Proportional Chambers.

6.1.2 Event Vertex Position

The event vertex reconstruction was discussed in Section 5.1. To ensure reliable event reconstruction, the z-coordinate of the primary event vertex must lie between -40 and 100 cm. The opening of the forward region up to $z = 100$ cm allows to keep ep events with low track multiplicity. In such events, the vertex can be falsely reconstructed due to, for example, a nuclear interaction in the event, but an isolated electron can still be reconstructed reliably.

6.1.3 Triggers

The events in the analysis are triggered by the LAr based triggers. These were originally developed to trigger NC and CC events [51]. The LAr trigger elements are based on either an imbalance in the energy deposits indicating $\not\!\!P_T$ or large compact electromagnetic energy deposits indicating energetic electrons. The LAr trigger efficiency for electrons with $P_T > 10$ GeV is $\gtrsim 98\%$. In the case of a $\mu + \not\!\!P_T$ event, no large energy deposits in the LAr are expected from the minimally ionising muon and the trigger signals are due to the hadronic system, similar as in CC events. The efficiency of the LAr triggers for such event topologies is simulated using 'pseudo CC' events, which are formed using a large sample of NC events, from which all information regarding the scattered electron is removed [58]. The events are reconstructed again and the CC selection (including the trigger requirements) is applied. The reselected events are reweighed by the ratio of the theoretical CC and NC cross sections. The

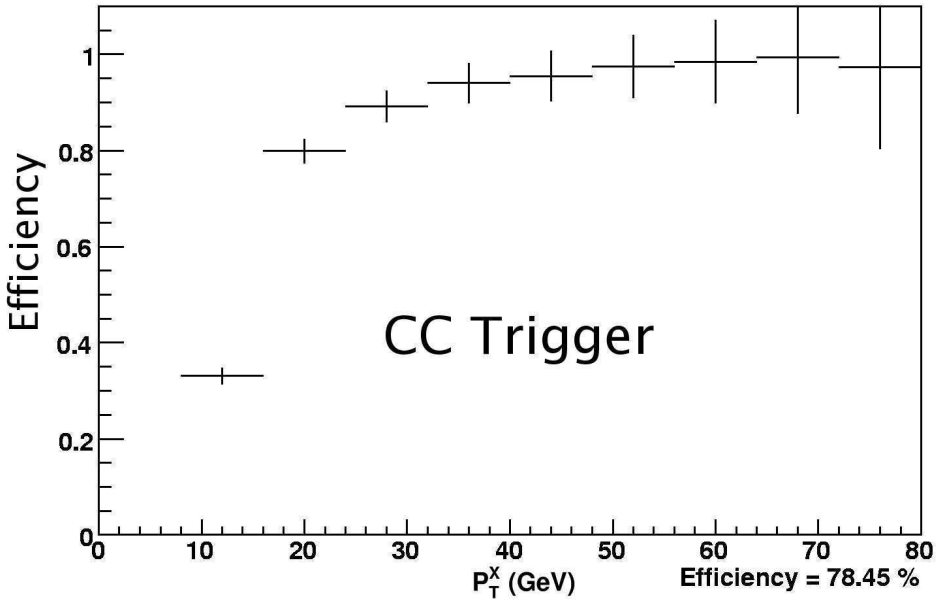

Figure 6.1: *Applied LAr trigger efficiences in the muon channel.*

selection efficiency of the resulting sample allows to determine the CC trigger efficiency ϵ_{CC}. The uncertainty on the latter is estimated at 30% of the inefficiency $(1 - \epsilon_{CC})$. In the analysis, all MC events are weighed with the obtained trigger efficiencies. Figure 6.1 shows the applied weights for muon events as a function of P_T^X. Only events with $P_T^X >$ 12 GeV are considered, since at lower values, the trigger is both not efficient and not well understood. For increasing values of P_T^X, the energy, deposited in the calorimeter, increases and a larger trigger efficiency is obtained.

6.1.4 Non-ep Background Rejection

As mentioned in Section 4.2.6, the rate of genuine ep processes at H1 is of the order 10 Hz whereas the background, mainly due to beam-gas interactions, exceeds 50 kHz. The main sources of the latter are halo particles, which come from interactions between the proton beam with the beam-pipe wall or gas molecules inside the beam-pipe, and cosmic muons, which are produced by highly ionising particles that penetrate the earth's atmosphere. Most of this non-ep background is suppressed by using timing information from the ToF system. A smaller part is rejected by the vertex requirements. For the rejection of the remaining part, a sophisticated set of non-ep background finder algorithms [59] is developed, which uses topological knowledge of a number of possible non-ep processes. Some of the algorithms are, however, sensitive to single W boson production and cannot be used for this analysis. To determine which background rejection algorithms can be used, the complete analysis chain is run with transparent background finders using simulated events from EPVEC. A 1% inefficiency is used as typical threshold to ignore certain algorithms, the result is shown in Figure 6.2.

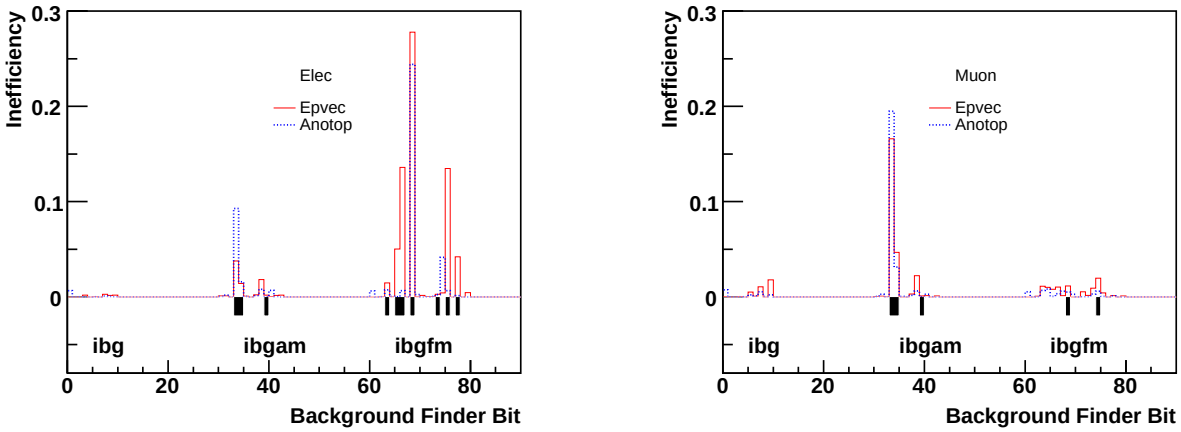

Figure 6.2: *The non-ep Background finder algorithms (bits), represented by the numbers on the horizontal axes in three regions (ibg, ibgam, and ibgfm) for simulated and reconstructed EPVEC and ANOTOP events in the electron (left) and muon (right) channel. The results are shown only for $\ell + \not{P}_T$ events that pass all selection criteria (except for non-ep background rejection) of the present analysis. The algorithms with a black mark below it are ignored in the analysis.*

6.2 Data Sets and Luminosities

The data sample that is used in the present analyses has been accumulated during the full HERA programme and corresponds to an integrated luminosity of 481 pb^{-1}. The various data taking periods and the respective centre-of-mass energies are given in Table 6.1. The HERA I data is taken in the period 1994-2000 and the HERA II data in 2003-2007. Between 1994 and 1997, the proton beam energy was 820 GeV resulting in a centre-of-mass energy $\sqrt{s} = 300$ GeV as opposed to $\sqrt{s} = 318$ GeV for the other data taking periods. The resulting different production cross sections of all processes are taken into account.

Period	**Interaction**	$\sqrt{s}$ **(GeV)**	$\int$**L (pb^{-1})**
1994 - 1997	e^+p	300	37.7
1998 - 1999	e^-p	318	13.9
1999 - 2000	e^+p	318	68.8
2003 - 2004	e^+p	318	54.3
2004 - 2006	e^-p	318	172.2
2006 - 2007	e^+p	318	134.0
Total			**481.4**

Table 6.1: *Data sets used in this analysis. The columns show from left to right: Running period, collision type ($e^{\pm}p$), centre of mass energy $\sqrt{s}$, and integrated luminosity $\int L$.*

6.3 Selection of $\ell + \not\!\!P_T$ Events

A summary of the selection criteria is given by Table 6.2. The detection phase space, already mentioned in Section 3.4, is defined by the cuts on P_T^ℓ, θ^ℓ, $D^{\rm jet}$ and $\not\!\!P_T$. The isolated lepton candidate should have $P_T^\ell >$ 10 GeV and be observed in the polar angle region $5^o < \theta^\ell < 140^o$. $D^{\rm jet}$, should be larger than 1 in $\eta - \phi$ space and P_T^X should be larger than 12 GeV. The upper limit on θ^ℓ rejects much of the NC background, while keeping as much signal as possible [20]. The lower limit on θ^ℓ is enforced by the detector acceptance (Chapter 4). The isolation of the lepton from jets is required to ensure that the lepton is not part of a jet.

Selection of the Isolated Lepton

In the search for events with an isolated electron and large $\not\!\!P_T$, or $e + \not\!\!P_T$ events, at least one electron should be present, isolated against hadrons (Section 5.2). The highest P_T such electron in the event is the 'isolated lepton'. Latter is assumed to come from the W boson decay, since this is most likely in the SM. Any second electron in the event, ordered in decreasing P_T, is assumed to be the scattered electron. No more than 3% of the total electron energy should be outside a cone of radius 1 in $\eta - \phi$ space around the electron and at least 95% of the cluster energy should be found in the electromagnetic part of the LAr. Central linked tracks must be 'good' tracks (Section 5.1) and be separated from all other vertex fitted tracks in the event by at least 0.5 in $\eta - \phi$ space. If there is no linked good track in the forward region, there must be both a linked non-vertex fitted track and another vertex fitted track with a distance of closest approach DCA<90 cm. Requiring the presence of a track reduces contributions from radiative photons.

In the muon channel, there must be precisely one muon in the event, which is isolated against hadrons. This muon must be of grade 1,2,3, or 5 (Section 5.4) and its distance to the nearest jet must be at least 1 in $\eta - \phi$ space.

Topological Cuts for ep Background Rejection

Besides the phase space selection criteria, further cuts to suppress SM background are applied on variables which are sensitive to the presence of high-energy undetected particles in the event: The azimuthal balance of the event, V_{ap}/V_p, the difference in azimuthal angle between the lepton and the hadronic system, $\Delta\phi_{\ell-X}$, and the longitudinal momentum imbalance, $\delta_{\rm miss}$. Additionally, muon events are required to have a minimum P_T^X, in order to select events with large $P_T^{\rm calo}$ for which a higher trigger efficiency is expected (Section 6.1.3), since for $\mu + \not\!\!P_T$ events $P_T^{\rm calo} \simeq P_T^X$. For $e + \not\!\!P_T$ events this problem does not arise, because the electron deposits at least 10 GeV in the calorimeter, for which the calorimeter trigger is very efficient and well understood. Electron events with low values of $P_T^{\rm calo}$ are required to have large ζ_ℓ^2, to reject NC events. Electron events must not contain any isolated muons to ensure that the two lepton channels are mutually exclusive.

The $\ell + \not\!\!P_T$ Data Sample

42 electron and 16 muon events are selected with these selection criteria. The total sample contains 58 events where 57.4 ± 7.3 are expected by the SM. As an illustration, three 'event displays' are shown in Figures 6.3-6.5 in longitudinal (left) and transverse (right) view of the H1 detector. The tracks are shown as well as the energy deposits in the calorimeters. Figure 6.3 shows an event with no hadronic activity and a single energetic isolated electron with P_T= 47 GeV. The $\not\!\!P_T$ in the event is 47 GeV.

Variable	Electron	Muon
θ^ℓ	$5^o < \theta^\ell < 140^o$	$5^o < \theta^\ell < 140^o$
P_T^ℓ	> 10 GeV	> 10 GeV
D^{jet}	> 1	> 1
$\not\!\!P_T$	> 12 GeV	> 12 GeV
P_T^{calo}	> 12 GeV	> 12 GeV
P_T^X	-	> 12 GeV
D^{track}	> 0.5 for $\theta^e > 45^o$	> 0.5
ζ_ℓ^2	> 5000 GeV^2 for $P_T^{\text{calo}} < 25$ GeV	
V_{ap}/V_p	< 0.5 (< 0.15 for $P_T^{\text{e}} < 25$GeV)	< 0.5 (< 0.15 for $P_T^{\text{calo}} < 25$GeV)
$\Delta\phi_{\ell-X}$	$< 160^o$	$< 170^o$
#isolated μ	0	1
δ_{miss}	> 5 GeV†	-
† In the case of exactly one isolated electron candidate in the event with the same charge as the beam.		

Table 6.2: *Topological selection requirements for the electron and muon channels in the search for $\ell + \not\!\!P_T$ events. The cuts on θ^ℓ, P_T^ℓ, D^{jet} and $\not\!\!P_T$ define the detection phase space.*

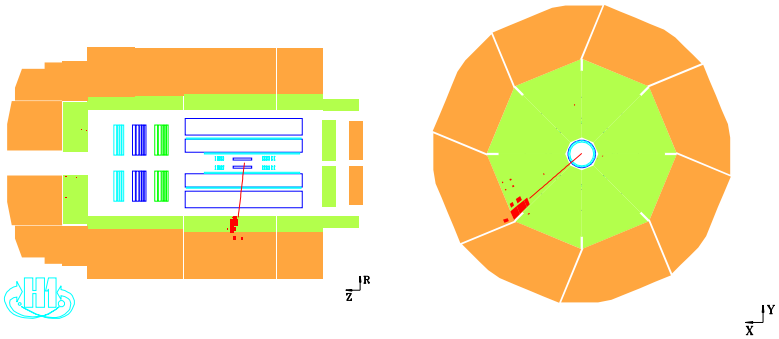

Figure 6.3: *Display of an event with an isolated electron and $\not\!\!P_T$. The measured electron P_T is 47 GeV and $\not\!\!P_T$=47 GeV. Recorded with the H1 detector in the HERA II e^+p data.*

This is a candidate event for W boson production via photoproduction in which case the scattered electron escapes down the beam-pipe and so does the proton remnant. Only the charged W boson decay lepton is found in the detector and the missing neutrino causes the large momentum imbalance. Figure 6.4 shows an event containing an energetic isolated muon with P_T= 38 GeV and a prominent jet of 24.7 GeV. The $\not\!\!P_T$ in the event is 51 GeV. This is a candidate event for single W boson production via DIS. A similar event is shown in Figure 6.5.

For each event in the $\ell + \not\!\!P_T$ data sample, the kinematic quantities P_T, θ^ℓ, P_T^X, and $\not\!\!P_T$, are reconstructed. The corresponding distributions in the electron and muon channel are shown in Figure 6.6. The data are compared to the expected sum-total of the SM signal and background contributions. For the calculations of the contributions of each of these processes, including the theoretical uncertainties, the Monte Carlo (MC) generators, presented in Section 4.4, are employed. The data distributions agree with the expectation in shape and number, which means that the physics processes and the corresponding detector response are well understood. The largest contribution to the sample comes from

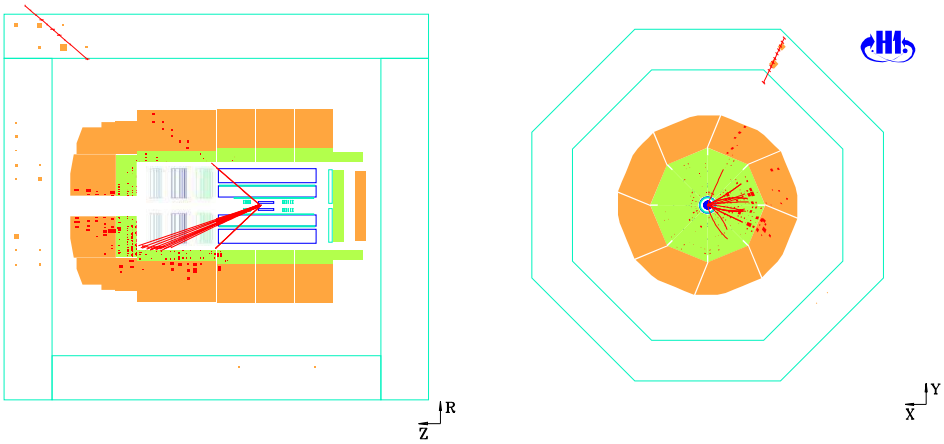

Figure 6.4: *Display of an event with an isolated muon, $\not\!\!P_T$ and a prominent jet. The measured muon P_T is 38 GeV, $\not\!\!P_T$= 51 GeV, and P_T^X=24.7 GeV. Recorded with the H1 detector in the HERA II e^+p data.*

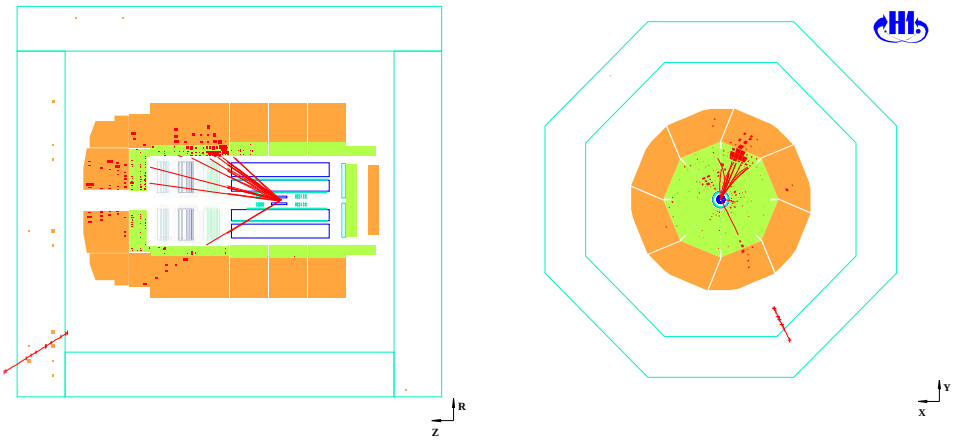

Figure 6.5: *Display of an event with an isolated muon, $\not\!\!P_T$ and a prominent jet. The measured muon P_T is 51 GeV, $\not\!\!P_T$=39 GeV, and P_T^X=48 GeV. Recorded with the H1 detector in the HERA II e^-p data.*

the signal processes, dominated by W boson production. The corresponding sample purity, defined as the fraction of signal events in the total sample, is $\sim 75\%$ in both lepton channels. The signal to noise quality estimator $S/\sqrt{N} = 9.5$. In the electron channel, the largest background contribution comes from CC events (17%). Contributions from NC, including bremsstrahlung (EG) is 8% and the lepton pair processes contribute 6%. The largest background in the muon channel comes also from CC processes contributing 10%. The only other significant background process in this channel is Lepton Pair Production (LL), contributing 8%.

The P_T^X and the transverse mass (M_T) distributions of the combined lepton channels are shown in Figure 6.7. The data follows the peak in the M_T distribution, typical for the W boson signal. This

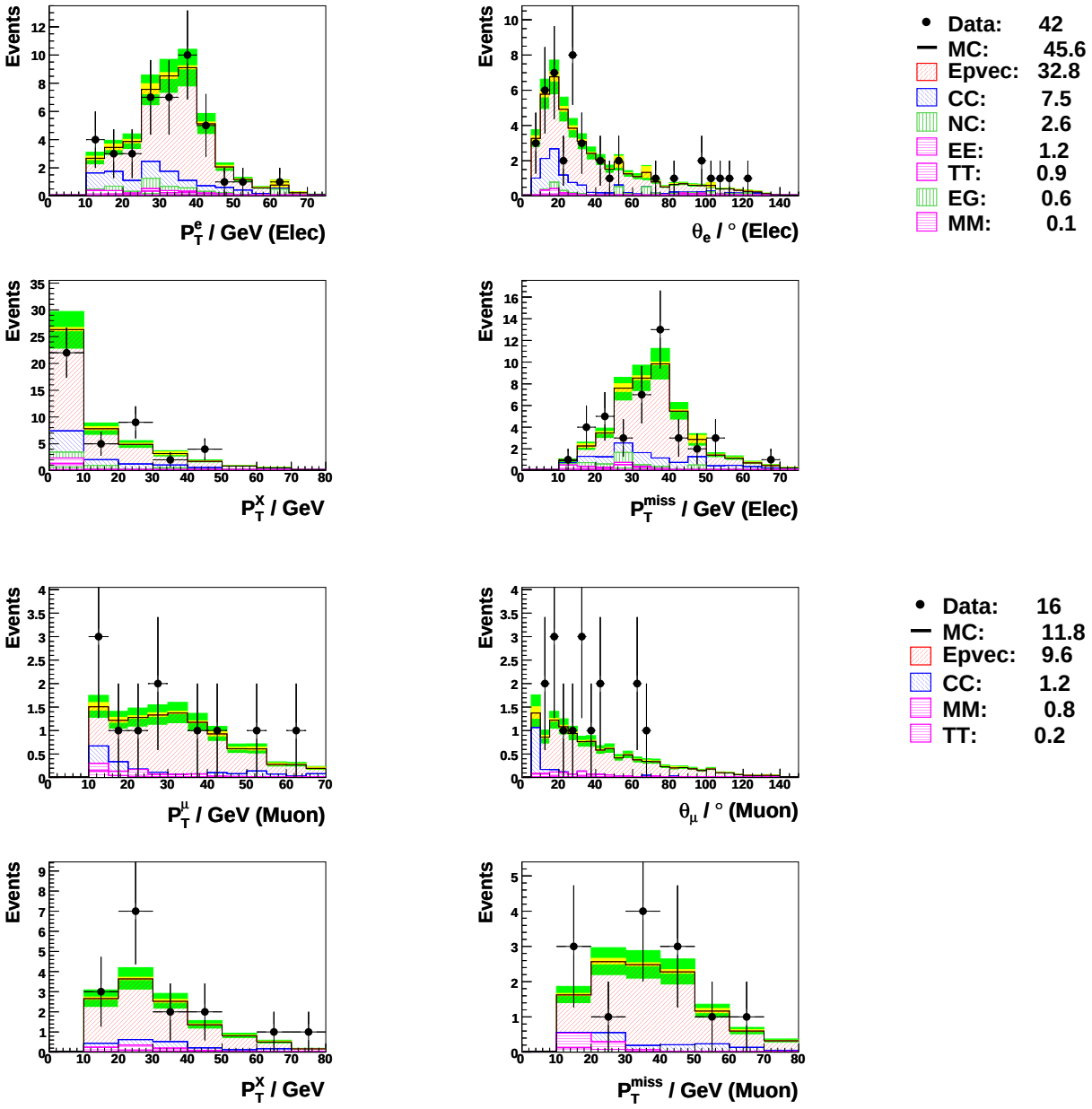

Figure 6.6: *Distributions in the electron (top two rows) and muon (bottom two rows) channels. For each are shown: Top left: P_T of the isolated lepton. Top right: θ of the isolated lepton. Bottom left: P_T^X. Bottom right: $\not{P}_T$. The data are denoted by the points and the statistical uncertainty by the bars. The contributions to the total sample from data and SM processes are explained in the legends, with the following SM processes: W boson production (Epvec), NC (NC), CC (CC), bremsstrahlung (EG), and pair production of electrons (EE), muons (MM), and taus (TT). The total uncertainty is the quadratic sum of the statistical and systematic uncertainties and is denoted by the filled areas on the total MC histogram where the lighter region denotes the statistical uncertainty.*

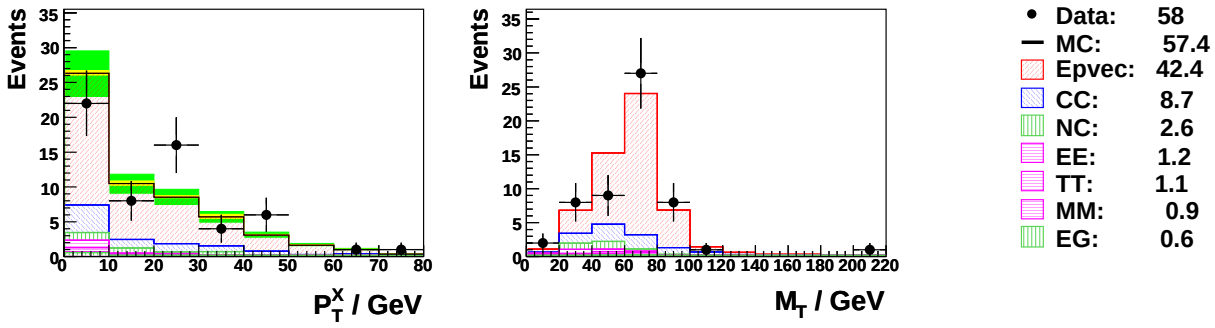

Figure 6.7: *Distributions of the total $\ell + \not{P}_T$ data sample in the electron and muon channel in P_T^X (left) and M_T (right). The contributions from the data and SM processes to the total sample are given in the legend on the right where the following SM processes are included: W boson production (Epvec), NC (NC), CC (CC), bremsstrahlung (EG), and pair production of electrons (EE), muons (MM), and taus (TT).*

Rates $e^{P_T^X\ (e^+p)}_{P_T^X>12}$	**H1 Data**	**SM exp**	**SM sig**	**SM bg**
$All\ P_T^X$	10	9.46 ± 1.27	7.55 ± 1.18	1.91 ± 0.41
$P_T^X > 25$	9	4.46 ± 0.62	3.59 ± 0.56	0.87 ± 0.25
Rates $\mu^{P_T^X\ (e^+p)}_{P_T^X>12}$	**H1 Data**	**SM exp**	**SM sig**	**SM bg**
$All\ P_T^X$	13	6.63 ± 1.00	5.74 ± 0.95	0.89 ± 0.19
$P_T^X > 25$	8	3.92 ± 0.59	3.45 ± 0.56	0.47 ± 0.10
Rates $e^{P_T^X\ (e^+p)}_{P_T^X\le 12}$	**H1 Data**	**SM exp**	**SM sig**	**SM bg**
$All\ P_T^X$	20	18.56 ± 2.27	12.48 ± 1.94	6.08 ± 1.04
$P_T^X > 25$	0	0.00 ± 0.00	0.00 ± 0.00	0.00 ± 0.00
Rates$^{P_T^X\ (e^+p)}_{e+\mu}$	**H1 Data**	**SM exp**	**SM sig**	**SM bg**
$All\ P_T^X$	43	34.64 ± 4.36	25.77 ± 4.00	8.88 ± 1.50
$P_T^X > 25$	17	8.38 ± 1.15	7.04 ± 1.10	1.34 ± 0.30

Table 6.3: *Event yields of the $\ell + \not{P}_T$ data sample in the e^+p data in the electron (top row) and muon channels (middle row) as well as for both channels combined (bottom row). The systematic uncertainties are also shown. The event yields are shown for the complete sample (All P_T^X) as well as at high P_T^X ($P_T^X > 25$ GeV). The SM signal (SM sig) comprises single W boson production and also Z boson production in the case of the invisible decay $Z \to \nu\bar{\nu}$. The contributions from SM backgrounds (SM bg) are also shown.*

peak is caused by the mass of the W boson, retained in the invariant mass of the observed lepton and the missing momentum. The peak cannot be explained without the signal MC and is a clear indication of single W boson production.

Discussion of the Excess

The first event observed at HERA that could be attributed to W boson production, was reported by H1 in 1994 [60] in 4 pb^{-1} of e^+p data. The kinematic properties of this event are not typical for the SM, and the probability to find it was only 0.03. In 1998 the H1 collaboration published a paper on 'Events with an isolated lepton and large missing transverse energy', using 37 pb^{-1} of e^+p data, in which an excess of events with respect to the SM expectation was announced [61]. Three events were atypical for the SM. One year later, ZEUS published its findings in turn, using 47.7 pb^{-1} of data, but could not confirm the excess [62]. In 2003, H1 had analysed 105 pb^{-1} of e^+p data, improved their background rejection algorithms, and extended the search to a larger phase space. At $P_T^X > 25$ GeV, 10 events were observed, where 2.92 ± 0.49 were expected by the SM [11]. The probability for the SM expectation to fluctuate to this number of events or more is 0.0015, corresponding to an excess of 3.0σ.

The official current preliminary status of the H1 $\ell + \not{P}_T$ data sample [63] was presented at [64]. At high P_T^X, 21 events are observed where 8.9 ± 1.5 are expected in 294 pb^{-1}of e^+p data, which is still a 3.0σ excess. The e^-p data sample is in agreement with the SM.

Due to reanalysis and reprocessing of the data, the kinematic properties of each event are subject to minor changes. As a result of this, events can migrate in or out of the data sample, even when the same kinematic cuts are employed. By this mechanism, 2 new events have come in and 6 events have migrated out of the combined data sample at $P_T > 25$ GeV, relative to the preliminary sample. The current e^+p data sample, used in this work, is tabulated in Table 6.3. The probability for the SM expectation of 8.38 ± 1.15 to fluctuate to the observed 17 events or more is 0.010, corresponding to a 2.3σ excess. This is still an arguable excess and its origin is unfortunately not cleared after HERA II.

However, the excess manifests itself in a limited region of phase space and only in the e^+p data set. The over-all agreement with the SM is good with 58 observed events where 57.4 ± 7.3 are expected, and with the description presented in Figures 6.6, 6.7 and Table 6.3. The predominance of the signal in the expectation and the observed event yield open the way to the cross section measurements, which are presented in the next chapter.

7 Cross Section Measurements

In this chapter the determination of the production cross section of events with an energetic isolated electron (e) or muon (μ) and large missing transverse momentum ($\ell + \not{P}_T$ events) and the differential $\ell + \not{P}_T$ cross section as a function of P_T^X ($d\sigma_{\ell+\not{P}_T}/dP_T^X$), are presented along with the measurement of the single W boson production cross section (σ_W).

7.1 Cross Section Extraction Method

For the cross section determination the following formula is used:

$$\sigma = \frac{N_{data} - N_{bg}^{MC}}{\mathcal{L}\,\mathcal{A}} \qquad \text{with} \qquad \mathcal{A} = \frac{N_{rec}^{MC}}{N_{gen}^{MC}}, \tag{7.1}$$

where N_{data} is the number of data events, N_{bg}^{MC} is the Monte Carlo (MC) estimate of the number of background events, and $\mathcal{L}$ is the integrated data luminosity. $\mathcal{A}$ is the acceptance, defined as the ratio of the number of reconstructed events N_{rec}^{MC} in the MC sample and the total number of generated events N_{gen}^{MC}.

As mentioned in Section 6.3, there is no measurement in the muon channel for the region $P_T^X < 12$ GeV. Therefore, the derived cross section for $P_T^X < 12$ GeV in the electron channel is used for the muon channel in that region under the assumption of lepton universality. The total combined cross section, σ_{tot} is determined as follows:

$$\sigma_{\text{tot}} = \sigma_e^{P_T^X>12} + \sigma_\mu^{P_T^X>12} + (1+f)\,\sigma_e^{P_T^X<12}, \tag{7.2}$$

where the subscript (e or μ) denotes the lepton channel and the superscript denotes the region of phase space determined by P_T^X. f is determined from MC simulation as the ratio of generated W boson production cross sections in the muon and electron channel at $P_T^X < 12$ GeV

$$f \equiv \frac{\sigma_\mu}{\sigma_e}. \tag{7.3}$$

The value of f is 0.89 ± 0.05 (systematic uncertainties are discussed in Section 7.5). This value for f implies that the cross section in the electron channel is larger than that in the muon channel in the region $P_T^X < 12$ GeV. This is due to extra contributions in the electron channel that are not present in the muon channel. These comprise $Z \to \nu\bar{\nu}$ events and single W boson production events in which the scattered electron plays the role of the isolated lepton.

7.2 Measurement of the $\ell + \not{P}_T$ Cross Section

The $\ell + \not{P}_T$ cross section is defined by the production rate of events with an isolated electron or muon and large missing transverse momentum in the detection phase space (Section 6.3) shown in Table 7.1.

$P_T^\ell > 10$ GeV
$5^o < \theta^\ell < 140^o$
$D_{\rm jet} < 1$ in $\eta - \phi$ space
$\not\!\!P_T >$ 12 GeV

Table 7.1: *The detection phase space.*

The $\ell + \not\!\!P_T$ cross section is determined by employing Equation (7.1) in which N_{gen}^{MC} is the number of MC events generated in the detection phase space.

The two contributions to the SM signal are single W and Z boson production. The latter contributes only in the electron channel via the decay $Z \to \nu\bar{\nu}$. The $\ell + \not\!\!P_T$ data sample obtained in the previous chapter is evaluated in the three separate regions of phase space from Equation (7.2). This is tabulated in Table 7.2.

Rates $^{(e^\pm p)}_{\ell+\not\!\!P_T}$	**H1 Data**	**SM exp**	**SM sig**	**SM bg**
$e_{P_T^X>12}$	19	17.52 ± 2.29	12.47 ± 1.95	5.06 ± 1.11
$\mu_{P_T^X>12}$	16	11.80 ± 1.73	9.58 ± 1.58	2.22 ± 0.49
$e_{P_T^X\leq 12}$	23	28.07 ± 3.54	20.31 ± 3.16	7.76 ± 1.41
$\int$	58	57.39 ± 7.32	42.36 ± 6.58	15.03 ± 2.86

Table 7.2: *Event yields obtained for the $\ell + \not\!\!P_T$ cross section measurement in the separate regions of phase space. Also shown are the contributions from the SM signal (SM sig) and background (SM bg) with systematic errors. The row marked with $\int$ contains the total yield.*

For a meaningful cross section measurement, the migration of events in and out of the phase space has to be limited. An example of a possible migration is an event containing an isolated lepton with P_T= 9.9 GeV. Due to the limited detection precision, the lepton can be reconstructed with P_T= 10.1 GeV and enter the data sample. A measure for the amount of migrations in a data sample is provided by the variables 'stability' and 'purity'. The values of each should not be much less than $\sim 30\%$ [51, 65]. They are defined as

$$\begin{aligned} \text{Stability} &\equiv \frac{N^{MC}_{\text{gen+rec}}}{N^{MC}_{\text{gen}}}, \\ \text{Purity} &\equiv \frac{N^{MC}_{\text{gen+rec}}}{N^{MC}_{\text{rec}}}, \end{aligned} \tag{7.4}$$

where 'gen' and 'rec' refer to 'generated' and 'reconstructed' respectively. $N^{MC}_{\text{gen+rec}}$ is the number of events both generated and reconstructed in the detection phase space. In order to remove the dependency on the acceptance, only reconstructed events are considered in (7.4).

The acceptance and purity are evaluated for each of the three regions of phase space and are tabulated in Table 7.3. It can be seen that all the acceptances are comparable. All purities are 99% if migrations within the detection phase space are ignored. This means that there is little inward migration of events that were generated outside the detection phase space. From the last row in Table 7.3, it can be seen that in the electron channel the purities in the separate regions of phase

	ELEC		MUON
	$P_T^X < 12$ GeV	$P_T^X > 12$ GeV	$P_T^X > 12$ GeV
Acceptance	0.556	0.523	0.499
Purity Ph.Sp	0.994	0.988	0.985
Purity P_T^X	0.988	0.919	0.963

Table 7.3: *Acceptance and Purities for the three regions of phase space in the calculation of the $\ell + \not{P}_T$ cros section. For the purities in the row 'Purity Ph.Sp', the migrations within the detection phase space are ignored. This is not the case for the purities presented in the last row 'Purity P_T^X'.*

space, $P_T^X < 12$ and $P_T^X > 12$ GeV, are smaller than the purity in the full phase space. This can only be due to events, which migrate within the detection phase space. The region $P_T^X < 12$ GeV represents a larger phase space and is less affected by this. Considering the lower limit for the purity of $\sim 30\%$, the over-all effect of these migrations can savely be ignored.

Applying Equation (7.1) together with Equation (7.2) results in the derived $\ell + \not{P}_T$ cross section

$$\sigma_{\ell+\not{P}_T} = 0.24 \pm 0.05\,(\text{stat}) \pm 0.04\,(\text{sys}) \quad \text{pb}, \tag{7.5}$$

which is in good agreement with the SM prediction

$$\sigma_W^{\text{SM}} = 0.26 \pm 0.04\,(\text{th.sys}) \quad \text{pb}. \tag{7.6}$$

All results are tabulated in Table 7.4. Agreement with the SM is observed in both lepton channels and both regions of phase space.

$\sigma_{\ell+\not{P}_T}^{(e^\pm p)}$ **(fb)**	**Measured** $\pm$ **stat** $\pm$ **sys**	**SM** $\pm$ **th sys**
$e_{P_T^X>12}$	$58.3 \pm 18.4 \pm 8.7$	52.2 ± 7.8
$\mu_{P_T^X>12}$	$62.6 \pm 18.2 \pm 8.7$	43.5 ± 6.5
$e_{P_T^X\leq 12}$	$64.3 \pm 20.3 \pm 11.0$	85.7 ± 12.8
$\int$	$242.5 \pm 46.3 \pm 37.1$	257.7 ± 38.6

Table 7.4: *Derived values for the $\ell + \not{P}_T$ cross section with statistical (stat) and systematic (sys) uncertainties, shown in the separate regions of phase space compared to the SM expectation with the theoretical uncertainty (th.sys) from the EPVEC generator. The row marked with $\int$ contains the total $\ell + \not{P}_T$ cross section and SM expectation.*

7.3 Measurement of the $\ell + \not{P}_T$ Differential Cross Section

The differential $\ell + \not{P}_T$ cross section is measured in four bins as a function of the hadronic transverse momentum P_T^X and is obtained by applying Equation (7.1) together with Equation (7.2) in each bin of P_T^X and subsequently dividing by the bin width. Bin center corrections are found to have an effect $< 1\%$ in each bin and are not applied. From Figure 7.1 and Table 7.5 it can be seen that the data yield is well described by the MC prediction in all bins.

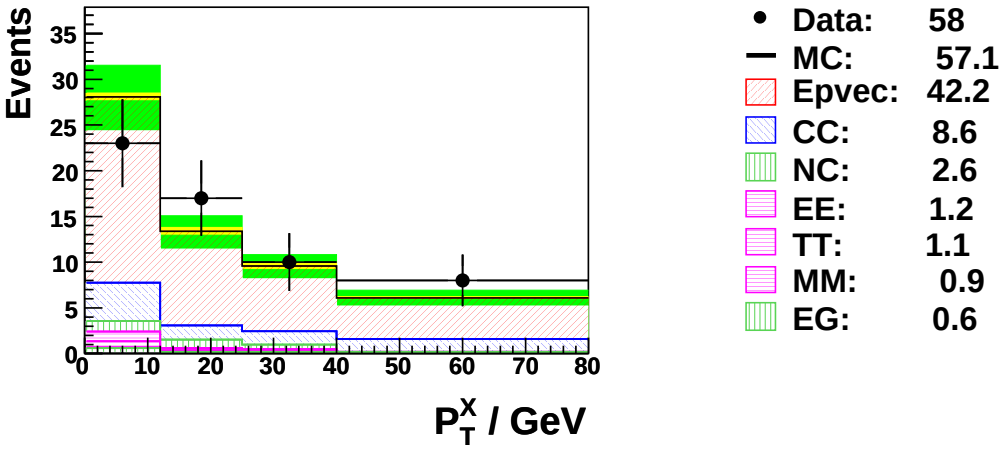

Figure 7.1: *The data yield (points) with statistical uncertainty (bars) in bins of P_T^X compared to the SM expectation (open histogram). The shaded inner regions around the open histogram line denote the statistical uncertainty of the MC and the darker regions denote the statistical and systematic uncertainties added in quadrature. The contributions from data and SM processes are explained in the legend (right), where the following SM processes are included: single W boson production (Epvec), NC (NC), CC (CC), bremsstrahlung (EG), and pair production of electrons (EE), muons (MM), and taus (TT).*

Rates$^{(e^\pm p)}_{P_T^X}$	**H1 Data**	**SM exp**	**SM sig**	**SM bg**
0 – 12	23	28.07 ± 3.54	20.31 ± 3.16	7.76 ± 1.41
12 – 25	17	13.37 ± 1.75	10.29 ± 1.61	3.09 ± 0.57
25 – 40	10	9.57 ± 1.24	7.12 ± 1.11	2.45 ± 0.49
40 – 80	8	6.08 ± 0.84	4.50 ± 0.70	1.58 ± 0.43

Table 7.5: *Event yields in bins of P_T^X compared to the SM expectation. Also shown are the contributions from the SM signal (SM sig) and background (SM bg) with systematic errors.*

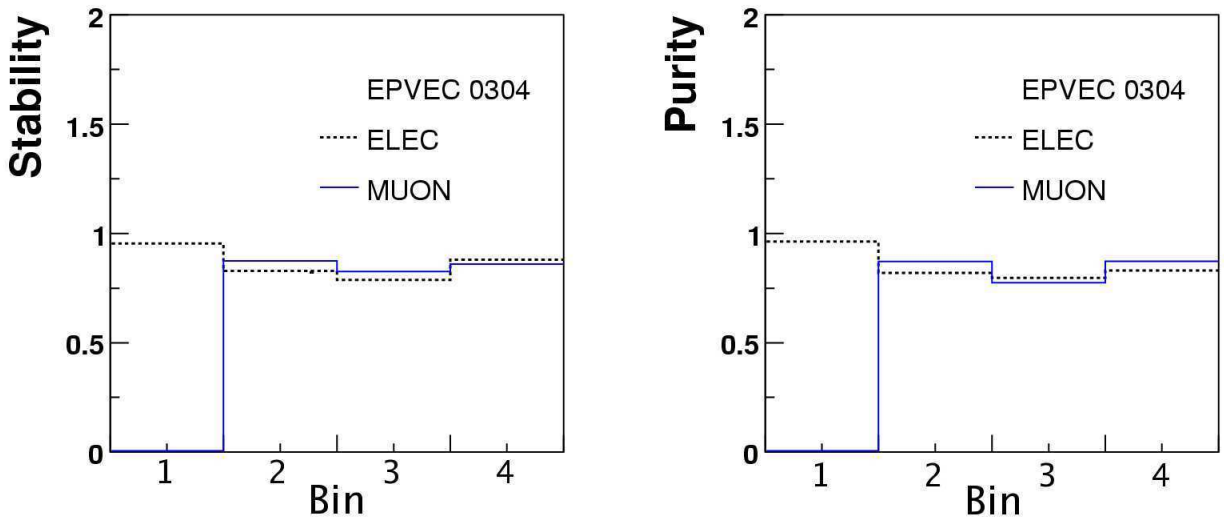

Figure 7.2: *Stability (left) and purity (right) for each bin in P_T^X for the electron (dotted line) and muon channel (solid line). Calculated with reconstructed events from EPVEC.*

The stability and purity for the bins in P_T^X are shown in Figure 7.2. The choice of bins in P_T^X is retained from the HERA I publication [11] for consistency. There are four bins ranging from 0 to 80 GeV separated at 12, 25 and 40 GeV, respectively. The signal contribution at P_T^X>80 GeV is negligible, as can be expected from Figure 3.8, and is not considered.

The acceptances per bin in the electron and muon channels are shown in figure 7.3. There is no acceptance in the muon channel due to the cut on $P_T^{\text{calo}} \simeq P_T^X$. Due to the LAr triggers (Section 6.1.3), the acceptance in the muon channel increases with increasing P_T^X. It rises to about 60%, which is larger than in the electron channel where the over-all cuts are more strict, as enforced by the larger SM background.

The derived differential cross section as a function of P_T^X is well described by the MC prediction and is shown in Figure 7.4 and tabulated in Table 7.6.

7.4 Measurement of the Single W Boson Production Cross Section

The production of $\ell + \not{P}_T$ events can be interpreted as single W boson production as mentioned before. The single W boson production cross section (σ_W) is determined by using Equation (7.1) and Equation (7.2). In this case the branching ratio for the decay $W \to e/\mu/\tau\,(\to e/\mu + \nu) + \nu$ is employed. N_{gen}^{MC} is the total number of generated events containing a W boson in the full phase space (electron channel) or at $P_T^X >$ 12 GeV (muon channel). The small SM contribution to N_{rec}^{MC} from Z boson

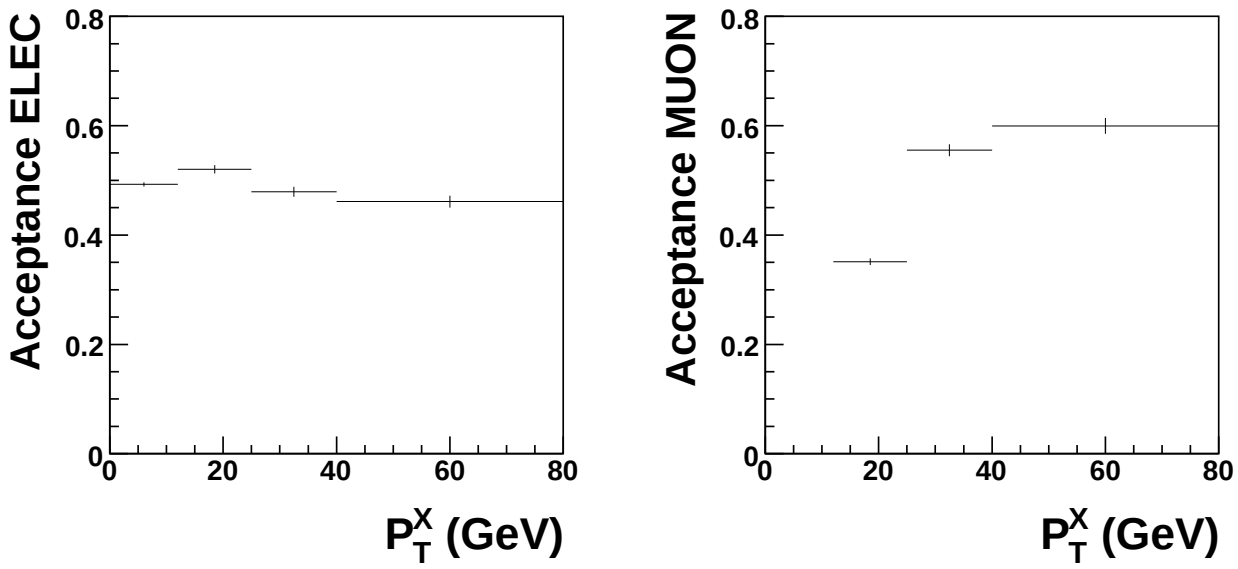

Figure 7.3: *Acceptances in the electron (left) and muon (right) channels in bins of P_T^X calculated using reconstructed events from EPVEC. The error bars denote the statistical error.*

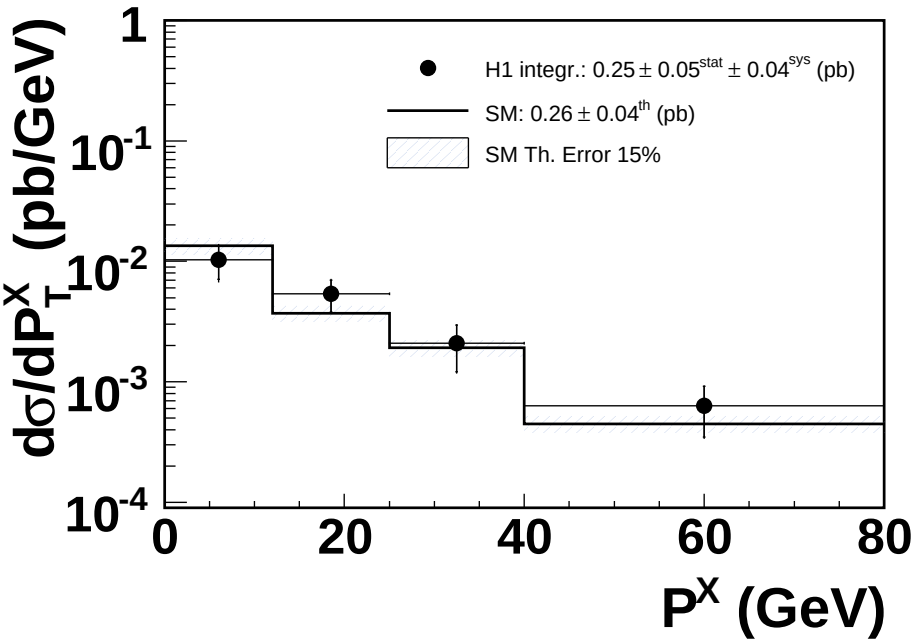

Figure 7.4: *Derived differential $\ell + \not{P}_T$ cross section as a function of P_T^X (points) where the dashes denote the statistical uncertainty and the total length of the error bars denote the quadratic sum of the statistical and systematic uncertainties in quadrature. The measurement is compared to the SM prediction (open histogram), which has a 15% theoretical uncertainty (hatched).*

$\frac{d\sigma_{\ell+\not{P}_T}{}^{(e^\pm p)}}{dP_T^X}(\frac{fb}{GeV})$	**Measured $\pm$ stat $\pm$ sys**	**SM $\pm$ th sys**
0 – 12	$10.13 \pm 3.20 \pm 1.75$	13.50 ± 2.02
12 – 25	$5.35 \pm 1.59 \pm 0.73$	3.72 ± 0.56
25 – 40	$2.06 \pm 0.87 \pm 0.32$	1.92 ± 0.29
40 – 80	$0.63 \pm 0.28 \pm 0.09$	0.45 ± 0.07

Table 7.6: *Derived values for the differential $\ell+\not{P}_T$ cross section in bins of P_T^X with statistical (stat) and systematic (sys) uncertainties, compared to the SM prediction with the theoretical systematic uncertainty (th.sys).*

Rates $^{W\ (e^\pm p)}$	**H1 Data**	**SM exp**	**SM sig**	**SM bg**
$e_{P_T^X>12}$	19	17.52 ± 2.20	11.66 ± 1.82	5.86 ± 1.12
$\mu_{P_T^X>12}$	16	11.80 ± 1.73	9.57 ± 1.58	2.23 ± 0.49
$e_{P_T^X\leq 12}$	23	28.07 ± 3.37	18.91 ± 2.94	9.17 ± 1.44
$\int$	58	57.39 ± 7.04	40.14 ± 6.24	17.26 ± 2.90

Table 7.7: *Event yields for the single W boson production in the separate regions of phase space compared to the SM expectation (SM exp), which is shown with the systematic uncertainty. Also shown are the SM signal (SM sig) and background (SM bg) contributions with the systematic uncertainties. The row marked with $\int$ denotes the total yield.*

production is considered here a background process. The resulting small difference in the number of SM signal and background events can be obtained by comparing Tables 7.2 and 7.7. The derived values for the single W boson production cross section in both lepton channels and regions of phase space are presented in Table 7.8. These results in the electron and muon channel at $P_T^X > 12$ GeV are consistent with lepton universality. The total single W boson production cross section is determined at

$$\sigma_W = 1.23 \pm 0.25\,(\text{stat}) + 0.13\,(\text{sys})\ \text{pb}, \tag{7.7}$$

which is in good agreement with the SM prediction

$$\sigma_W^{\text{SM}} = 1.31 \pm 0.20\,(\text{th.sys}) \quad \text{pb}. \tag{7.8}$$

This is the first significant determination of the W boson production cross section at HERA.

7.5 Treatment of Systematic and Statistical Uncertainties

Table 7.9 summarises all sources of systematic uncertainty. They were introduced in Chapter 5. For the cross section measurements, only those are taken into account that have an estimated effect on the total signal yield larger than 1%. Table 7.10 tabulates the resulting systematic uncertainties for the $\ell + \not{P}_T$ cross section. For the single W boson production cross section these numbers are identical for all practical purposes, except that no model uncertainty is applied.

The largest systematic contribution stems from the model dependence. This enters the calculations via the uncertainty on the acceptance and the relative production cross sections in the electron

$\sigma_W^{(e^\pm p)}$ (fb)	Measured $\pm$ stat $\pm$ sys	SM $\pm$ th sys
$e_{P_T^X>12}$	$284.9 \pm 95.3 \pm 33.0$	252.9 ± 37.9
$\mu_{P_T^X>12}$	$359.0 \pm 104.4 \pm 33.9$	249.5 ± 37.4
$e_{P_T^X\leq 12}$	$292.8 \pm 101.9 \pm 37.6$	400.2 ± 60.0
$\int$	$1231.7 \pm 248.6 \pm 129.2$	1305.8 ± 195.9

Table 7.8: *Derived values for the single W boson production cross section in the separate regions of phase space for the electron (e) and muon (μ) channels with statistical (stat) and systematic (sys) uncertainties, compared to the SM expectation with the theoretical systematic uncertainty (th.sys). The row marked with $\int$ denotes the total combined cross section.*

and muon channels, expressed by the factor f in Equation (7.3). A 10% model dependence on the acceptance is applied to stay as model independent as possible. Latter is estimated [11] using two further generators, which produce single W bosons with different kinematic distributions from those of EPVEC. The used generators are an implementation of W boson production within PYTHIA [66] and ANOTOP (Section 4.4). The systematic uncertainty on f is estimated using ANOTOP. The EPVEC value is 0.891 ± 0.006 and the ANOTOP value is 0.90 ± 0.04, where the uncertainties are determined by statistics only. The EPVEC central value of 0.89 is taken and the uncertainty set at 0.05.

The total theoretical uncertainty on the derived contributions of the SM background processes enters the derivation of the cross section via the estimated number of background events in Equation (7.1). This represents the second largest source of systematic uncertainty and is denoted by 'Theory' in Table 7.10.

Statistical Uncertainty on the Combined Cross Sections

The total cross section is calculated from the three terms in Equation (7.2). The statistical uncertainties between terms are added in quadrature. Since the same data is used for the cross section measurement in both the electron and muon channel at low P_T^X, the statistical uncertainties of these terms are added linearly

$$\left(\mathrm{d}\sigma^{\mathrm{stat}}_{\mathrm{total}}\right)^2 = \left(\mathrm{d}\sigma^{\mathrm{stat}}_{e\,P_{TX}>12}\right)^2 + \left(\mathrm{d}\sigma^{\mathrm{stat}}_{\mu\,P_{TX}>12}\right)^2 + \underbrace{\left((1+f)\,\mathrm{d}\sigma^{\mathrm{stat}}_{e\,P_{TX}>12}\right)^2}_{\text{linear addition}}. \tag{7.9}$$

Systematic Uncertainty on the Combined Cross Sections

The total systematic uncertainty is obtained by adding in quadrature the systematic uncertainties of each considered systematic i

$$\left(\mathrm{d}\sigma^{up\,(dn)}_{\mathrm{total}}\right)^2 = \sum_i \left(\mathrm{d}\sigma^{up\,(dn)}_{i\,e\,P_{TX}>12} + \mathrm{d}\sigma^{up\,(dn)}_{i\,\mu\,P_{TX}>12} + (1+f)\;\mathrm{d}\sigma^{up\,(dn)}_{i\,e\,P_{TX}<12}\right)^2. \tag{7.10}$$

Source	HERA I	HERA II
E^{jet}	LAr: $P_{T\,\text{jet}} < 8\,\text{GeV}$ 5% LAr: $P_{T\,\text{jet}} > 8\,\text{GeV}$ 2% Spacal: 7%	
E_e	LAr : z < 20 cm 0.7% LAr :20 z<100 cm 1.5% LAr : 100 < z cm 3.0% Spacal: 0.5%	LAr : z < 20 cm 1.0% LAr :20 z<100 cm 2.0% LAr : 100 < z cm 3.0% Spacal: 0.5%
θ_{JET}	$\theta_{\text{jet}} < 20^o$: 5 mrad $\theta_{\text{jet}} > 20^o$: 10 mrad	
θ^e	LAr: 3 mrad Spacal: 1 mrad	
ϕ^{e}	1 mrad	
V_{ap}/V_p	0.02%	
P_T^μ	5%	
θ^μ	3 mrad	
ϕ^μ	1 mrad	
ϕ^{jet}	1 mrad	
μ ID	5% if $\theta_\mu > 12.5^o$ else 15%	
elec ID	2%	
$\mathcal{L}$	4%	
Track/Clus Linking	3%	
Trigger	$2\% \oplus 30\%(1 - \epsilon_{CC})$	

Table 7.9: *All systematic uncertainties, which are taken into account shown for HERA I and HERA II for the jet energy E^{jet}, electron energy E^e, jet polar angle θ^{jet}, electron polar angle θ^e,electron azimuthal angle ϕ^e, vratio V_{ap}/V_p, muon $P_T P_T^\mu$, muon azimuth angle ϕ^μ, jet azimuth angle ϕ^{jet}, muon identification efficiency μ ID, electron identification efficiency elec ID, integrated luminosity $\mathcal{L}$, track cluster linking efficiency Track/Clus Linking, and trigger efficiency Trigger, where ϵ_{CC} is the trigger efficiency estimated from pseudo CC constants.*

Systematic	%
`Trigger`	3.24
`Trk/Clus Lnk`	3.48
`Elec ID`	2.21
μ `ID`	1.90
Theory	7.39
Lumi	4.00
Model	11.28

Table 7.10: *Systematic uncertainties on the derived $\ell + \not{P}_T$ cross section in percent.*

8 Measurement of the $WW\gamma$ Vertex

In this chapter the measurement of the $WW\gamma$ vertex is presented. A likelihood method is employed to extract limits on the parameters $d\kappa$ and λ that govern the triple boson coupling $WW\gamma$. The $\ell+\not{P}_T$ data sample with a SM single W boson interpretation is used. [1]

8.1 Likelihood Fit

As discussed in Section 3.3, the effective Lagrangian (3.5) describes the possible production of single W bosons through couplings, parametrised by the variables κ and λ. The SM values are $\kappa = 1$ and $\lambda = 0$. Instead of κ, the parameter

$$d\kappa \equiv \kappa - 1 \tag{8.1}$$

will be used, such that any non-zero value for $d\kappa$ is a deviation from the SM.

The sensitivity of the total single W boson production cross section σ_W to anomalous values of $d\kappa$ and λ (Figure 3.5) facilitates the use of the 'counting' experiment to compare the observed (counted) number of events N_{obs} to the expected number of events N_{exp} a function of $d\kappa$ and λ. This allows to set limits on their possible anomalous values. The expected number of events N_{exp} can be written as

$$N_{exp}\,(d\kappa, \lambda) = B\mathcal{L}\,\mathcal{A}\,\sigma_W\,(d\kappa, \lambda) + N_{bg}. \tag{8.2}$$

Here, B is the branching ratio in the decay $W \to e/\mu/\tau\,(\to e/\mu + \nu) + \nu$. The luminosity $\mathcal{L}$, the acceptance $\mathcal{A}$, the expected number of background events N_{bg}, and $\sigma_W(d\kappa, \lambda)$, the predicted cross section as a function of $d\kappa$ and λ, are known only with finite precision, which will affect the limits. In the following, this is included and will be discussed explicitely in Section 8.4.

A likelihood function L is introduced as the Poisson probability density of observing N_{obs} data events for given $d\kappa$ and λ

$$L_{N_{obs}|(d\kappa,\lambda)} = \frac{(N_{exp})^{N_{obs}}\, e^{-N_{exp}}}{N_{obs}!}, \tag{8.3}$$

where N_{exp} is a function of $d\kappa$ and λ as expressed in Equation (8.2). Of interest for the measurement, however, is the probability to observe N_{exp} as a function of $d\kappa$ and λ, given the outcome N_{obs} of the counting experiment. In a Bayesian approach [33], this is the 'posterior probability densitiy'

$$P_{(d\kappa,\lambda)|N_{obs}} = \frac{L_{N_{obs}|(d\kappa,\lambda)} \cdot P_{(d\kappa,\lambda)}}{P_{N_{obs}}}. \tag{8.4}$$

Here, $P_{(d\kappa,\lambda)}$ is the prior probability to observe any pair $(d\kappa, \lambda)$; it 'reflects the experimentor's degree of believe before carrying out the measurement', cite taken from ref. [33]. In this case, a constant probability density to observe $P_{(d\kappa,\lambda)}$ is assumed on the domain $\mathcal{D}$

$$\begin{aligned} -7 < \quad d\kappa \quad < 7, \\ -7 < \quad \lambda \quad < 7. \end{aligned} \tag{8.5}$$

[1] With the possible exception of non-SM values for $d\kappa$ and λ.

$P_{(d\kappa,\lambda)}$ is assumed 0 elsewhere. This domain must contain all values of $d\kappa$ and λ, for which there exists a non-vanishing probability to agree with the result of the counting experiment. Furthermore, it is required that $\int_{\mathcal{D}} P_{(d\kappa,\lambda)} d\,(d\kappa)\, d\lambda = 1$. The choice for the domain boundaries is inspired by the measured single W boson production cross section (previous chapter) and the dependence of the predicted cross section on $d\kappa$ and λ (Figure 3.5). In Equation (8.4), $P_{N_{obs}}$ is the prior probability density to observe N_{obs} events. Using the law of total probability this can be expressed as

$$P_{N_{obs}} = \int L_{N_{obs}|(d\kappa,\lambda)} \cdot P_{(d\kappa,\lambda)} d\,(d\kappa)\, d\lambda, \tag{8.6}$$

which, together with Equation (8.4), finally leads to the posterior probability density

$$P_{(d\kappa,\lambda)|N_{obs}}\,(d\kappa,\lambda) = \frac{L_{N_{obs}|(d\kappa,\lambda)} \cdot P_{(d\kappa,\lambda)}}{\int\int L_{N_{obs}|(d\kappa',\lambda')} \cdot P_{(d\kappa',\lambda')}\; d\,(d\kappa')\, d\lambda'}. \tag{8.7}$$

As discussed in Section 3.3, the P_T^X spectrum is expected to have larger sensitivity to anomalous values of $d\kappa$ and λ at higher P_T^X ($P_T^X > 12$ GeV). A priori, this gain (Figure 3.5) is not expected to be cancelled by the expected loss of statistical precision (see also Table 8.1). To confirm this, the measurement is presented here in both the full phase space and in the region $P_T^X > 12$ GeV.

8.2 Limits Extraction

Single Parameter Limits

The extraction of the single parameter limits on $d\kappa$ and λ commences by performing the likelihood fit (8.7) where one parameter is allowed to vary while the other is fixed to its SM value, and vice versa. The resulting probability distributions $P_{(d\kappa,\lambda=0)|N_{obs}}$ and $P_{(d\kappa=0,\lambda)|N_{obs}}$, are shown in Figure 8.1 for both the full phase space and for $P_T^X > 12$ GeV.

The probability distribution for $P_{(d\kappa,\lambda=0)|N_{obs}}$ displays two peaks. The reason for this is that the measured cross section σ_W^{Data} intersects the theoretical curve σ_W at two points (see also Figure 3.5) resulting in two values for $d\kappa$, which are favoured by the outcome of the counting measurement. For $P_{(d\kappa=0,\lambda)|N_{obs}}$ this is also the case, although, only at $P_T^X > 12$ GeV. When the lower P_T^X events are included in the measurement, only one value for λ is statistically favoured. This can be understood by observing that σ_W^{Data} in the full phase space is smaller than the SM expectation (at $d\kappa = 0$ and $\lambda = 0$), whereas for the region $P_T^X > 12$ GeV, it is larger, as is shown in Table 8.1. For the same

Region	σ_W^{Data}	$\sigma_W^{\text{SM}}(d\kappa = 0, \lambda = 0)$
$P_T^X > 0$	1.232 ± 0.280	$1.306 \pm \quad 0.196$
$P_T^X > 12$	0.644 ± 0.156	$0.502 \pm \quad 0.075$

Table 8.1: *Derived values for the measured σ_W (σ_W^{Data}) in pb together with the total uncertainty in the full phase space ($P_T^X > 0$ GeV) and in the region of phase space where $P_T^X > 12$ GeV. Also shown are the SM expectations $\sigma_W^{SM}(d\kappa = 0, \lambda = 0)$ with the theoretical uncertainties. The total uncertainty on σ_W^{Data} is calculated by adding in quadrature the total statistical uncertainty (added in quadrature among bins) and the total systematic uncertainty (added linearly among bins).*

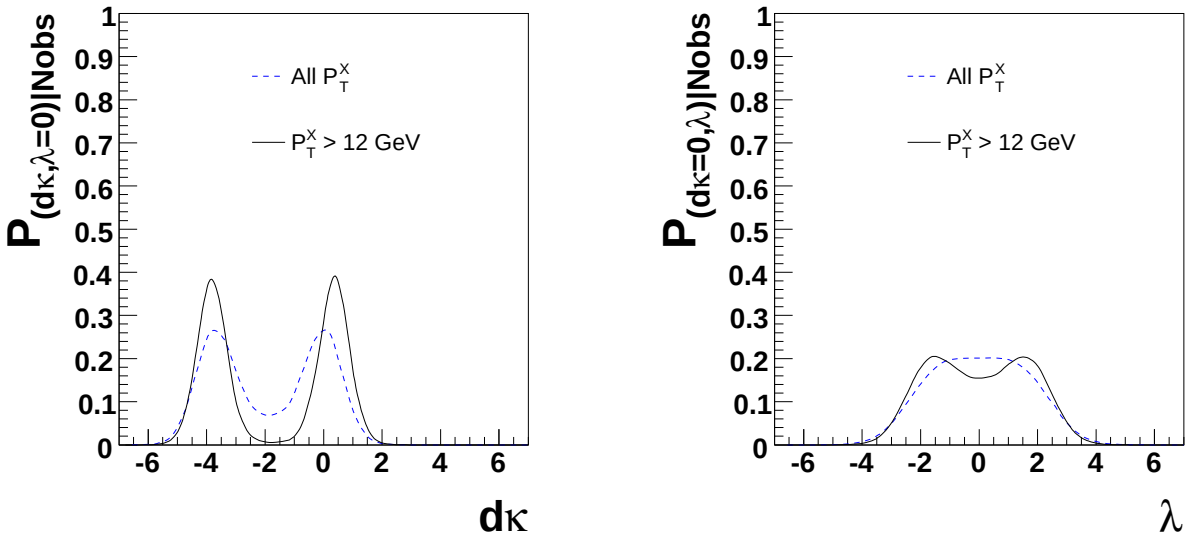

Figure 8.1: $P_{(d\kappa,\lambda=0)|N_{obs}}$ *(left) and* $P_{(d\kappa=0,\lambda)|N_{obs}}$ *(right) for all phase space (dotted) and for the region* $P_T^X > 12$ *GeV (continuous).*

reason, $P_{(d\kappa,\lambda=0)|N_{obs}}$ is shifted toward larger absolute values for $d\kappa$ in the region $P_T^X > 12$ GeV. Also in this region, the two peaks in $P_{(d\kappa,\lambda=0)|N_{obs}}$ are steeper and higher than in the full phase space, which implies stricter limits. For $P_{(d\kappa=0,\lambda)|N_{obs}}$, the situation is different. At higher P_T^X, the degeneracy sets in and leads to a lessened probability density around $\lambda = 0$.

All this can be quantified by using the Confidence Level (CL) as a function of either parameter, represented by x, in

$$CL\,(x) = \int_{P(x')>P(x)} P\,(x')\,dx'. \tag{8.8}$$

This definition of the CL is chosen such, that in the integral over x, the points with highest probability are always included (maximum likelihood). The 95% CL single parameter limits can now be obtained by using Equation (8.7) in Equation (8.8), and identifying the parameter values for which $CL < 0.95$. The results are displayed in Table 8.2. The limits on $d\kappa$ are indeed much better for the measurement at $P_T^X > 12$ GeV. A decrease of 25% is observed for the total 95% CL region $\Delta d\kappa_1 + \Delta d\kappa_2$. The corresponding limits for λ are slightly better as well.

95% CL	$d\kappa_1$	$\Delta d\kappa_1$	$d\kappa_2$	$\Delta d\kappa_2$	λ	$\Delta\lambda$
All P_T^X	-4.82 .. -2.02	2.80	-1.96 .. 1.08	3.04	-3.05 .. 3.05	6.10
$P_T^X > 12$	-4.90 .. -2.72	2.18	-0.75 .. 1.46	2.21	-2.93 .. 2.94	5.87

Table 8.2: *95% CL single parameter limits for the parameters* $d\kappa$ *and* λ *for the measurement in the full phase space (all* P_T^X*) and that in the region* $P_T^X > 12$ *GeV. The subscripts* 1 *and* 2 *denote the disjoint regions in* $d\kappa$*. The length of the individual regions is denoted by* $\Delta d\kappa$ *and* $\Delta\lambda$*.*

Limits in the two Parameter Fit

The limits in two dimensions are obtained by performing the likelihood fit of Equation (8.7), whereby both $d\kappa$ and λ are allowed to vary. The confidence level is defined using again Equation (8.8), where the one-dimensional dependence on x is replaced by the two-dimensional dependence on $d\kappa$ and λ. The resulting 68% and 95% CL regions are shown in Figure 8.2. Note again the decrease of the 95% CL region when the events at $P_T^X < 12$ GeV are not used.

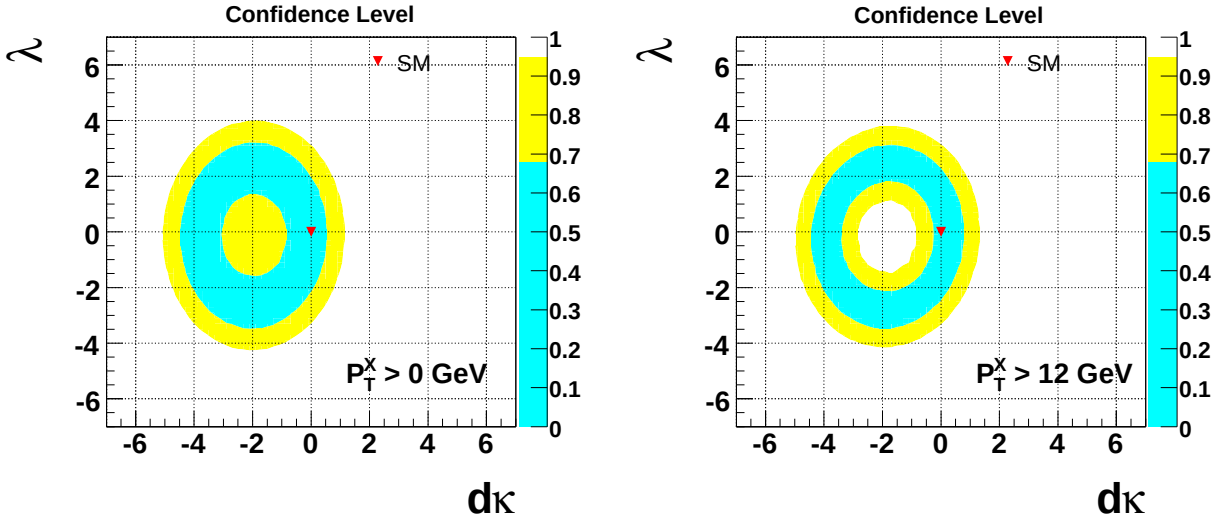

Figure 8.2: *68% and 95% CL regions on $d\kappa$ and λ for the full phase space (left) and for $P_T^X > 12$ GeV (right). The SM prediction is also shown (triangle).*

8.3 Results

The measurement at $P_T^X > 12$ GeV has a larger sensitivity to the coupling parameters $d\kappa$ and λ. The 95% CL single parameter limits are

$$-4.9 < \quad d\kappa \quad < -2.7, \tag{8.9}$$
$$-0.8 < \quad d\kappa \quad < \quad 1.5, \tag{8.10}$$
$$-2.9 < \quad \lambda \quad < \quad 2.9. \tag{8.11}$$

The 68% and 95% CL regions in two dimensions are shown in the right plot of Figure 8.2. The corresponding 95% CL two dimensional limits are

$$\begin{aligned} -5.0 < \quad d\kappa \quad < \quad 1.3, \\ -4.2 < \quad \lambda \quad < \quad 3.8 \end{aligned} \tag{8.12}$$

All results are in agreement with the SM expectation $d\kappa = \lambda = 0$. A comparison with other collider experiments is given in Chapter 10.

Source	$P_T^X > 0$ GeV	$P_T^X > 12$ GeV	δ (%)
$\mathcal{L}$	481.4 ± 19.3	481.4 ± 19.3	4
$\mathcal{A}$	0.258 ± 0.01	0.356 ± 0.01	4
N_{bg}	17.26 ± 3.45	8.09 ± 1.62	20
σ_W	$\sigma_W(d\kappa, \lambda)$	$\sigma_W(d\kappa, \lambda)$	15

Table 8.3: *The systematic uncertainties in the $WW\gamma$ analysis for the luminosity $\mathcal{L}$, acceptance $\mathcal{A}$, and the number of background events N_{bg}. The predicted single W boson production cross section $\sigma_W(d\kappa, \lambda)$ varies, depending on $d\kappa$ and λ. The values are shown for the full phase space $P_T^X > 0$ GeV and for $P_T^X > 12$ GeV. The last column contains the relative error δ of each source of systematic uncertainty in percent (%).*

8.4 Systematic Uncertainties

The sources of systematic uncertainties are the luminosity $\mathcal{L}$, the acceptance $\mathcal{A}$, the expected number of background events N_{bg}, and $\sigma_W(d\kappa, \lambda)$, the predicted total single W boson production cross section as a function of $d\kappa$ and λ. They enter the calculation via N_{exp} (Equation (8.2)). They are presumed uncorrelated and to be distributed around their mean values according to a Gaussian distribution. Under these assumptions they can be integrated out of the probability (8.7)

$$P_{(d\kappa,\lambda)|N_{obs}} = P_{(d\kappa,\lambda)|N_{obs}}(x_1, \ldots) \cdot \prod_{i=1}^{N_{sources}} \int \mathcal{G}_i(x_i)\, dx_i, \tag{8.13}$$

where the x are the systematic sources with mean $< x >$ and standard deviation σ_x and

$$\mathcal{G}(x) = \frac{1}{\sqrt{2\pi}\sigma_x} e^{-\frac{(x-<x>)^2}{2\sigma_x^2}}. \tag{8.14}$$

The systematic uncertainties are tabulated in Table 8.3. $\mathcal{L}$ is known to 4% (Section 4.2.4). The central value of $\mathcal{A}$ is assumed to be constant for different values of $d\kappa$ and λ. A 4% systematic uncertainty on $\mathcal{A}$ arises from the uncertainties on the trigger, track/cluster linking, and lepton identification efficiencies (Table 7.10). The systematic uncertainty on N_{bg} also includes these, but is dominated by the theoretical uncertainties introduced by the MC generators. The uncertainty on $\sigma_W(d\kappa, \lambda)$ is the 15% theoretical uncertainty from the EPVEC generator (Section 3.2).

The effect of each source of systematic uncertainty is studied and is tabulated in Table 8.4. The dominant systematic uncertainty is the theoretical systematic uncertainty on σ_W. The uncertainties on N_{bg} and $\mathcal{A}$ must be partly correlated, since both underly the uncertainties on the trigger simulation, track/cluster linking and lepton identification efficiencies. However, the demonstrated small effect of the uncertainty on N_{bg} allowes this to be safely neglected.

Finally, Figure 8.3 shows the smearing effect on $P_{(d\kappa,\lambda=0)|N_{obs}}$ and $P_{(d\kappa=0,\lambda)|N_{obs}}$, which results from incorporating the systematic uncertainties. The measurement is dominated by the statistical uncertainty.

Source	$d\kappa_1$	$\Delta(d\kappa_1)$	$d\kappa_2$	$\Delta(d\kappa_2)$	λ	$\Delta\lambda$
None	-4.59 .. -3.00	1.59	-0.55 .. 1.15	1.70	-2.55 .. 2.56	5.11
$\mathcal{L}$	-4.61 .. -2.94	1.67	-0.56 .. 1.16	1.72	-2.58 .. 2.59	5.17
N_{bg}	-4.62 .. -2.87	1.75	-0.62 .. 1.18	1.80	-2.58 .. 2.60	5.18
$\mathcal{A}$	-4.61 .. -2.93	1.68	-0.56 .. 1.18	1.74	-2.58 .. 2.60	5.18
$\sigma_W(d\kappa,\lambda)$	-4.84 .. -2.79	2.05	-0.70 .. 1.40	2.10	-2.86 .. 2.90	5.76
All	-4.90 .. -2.72	2.18	-0.75 .. 1.46	2.21	-2.93 .. 2.94	5.87

Table 8.4: *The 95% CL single parameter limits for $d\kappa$ and λ, the size of the corresponding regions ($\Delta(d\kappa)$ and $\Delta\lambda$), shown for the cases where no systematic uncertainties are included (None), only one is included ($\mathcal{L}$, N_{bg},$\mathcal{A}$ or $\sigma_W(d\kappa,\lambda)$), and all are included (All).*

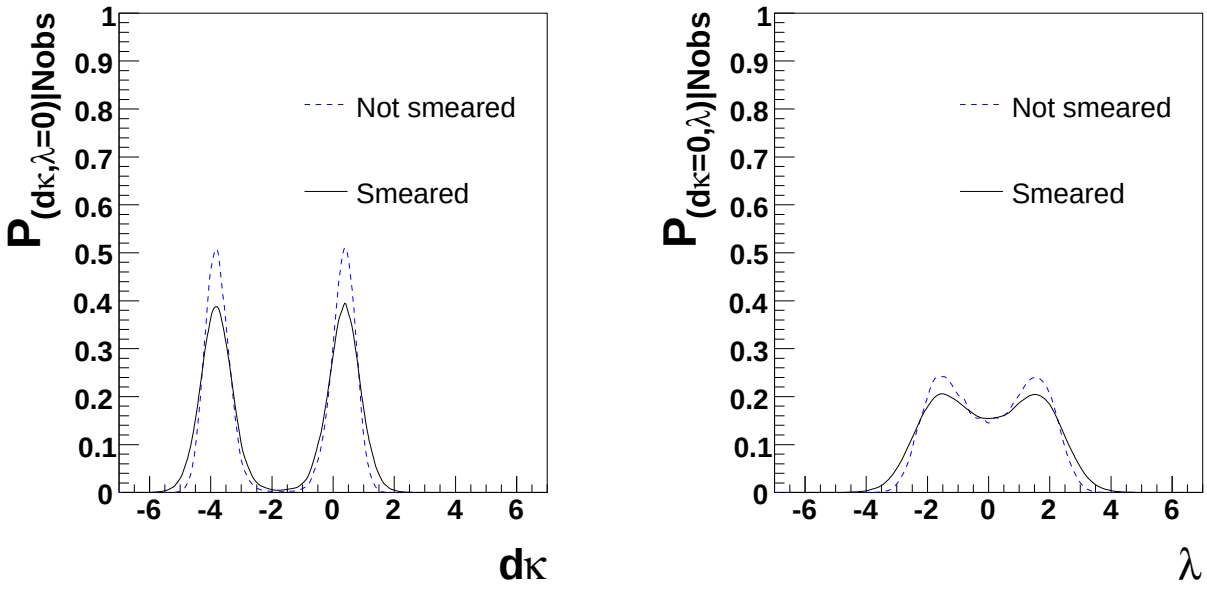

Figure 8.3: *$P_{(d\kappa,\lambda=0)|N_{obs}}$ (left) and $P_{(d\kappa=0,\lambda)|N_{obs}}$ (right) for the cases where the systematic uncertainties are ignored (not smeared) and included (smeared).*

9 Measurement of the W Boson Polarisation Fractions

In this chapter the measurement of the W boson polarisation fractions is presented. Since the polarisation dependent observables depend on the charge of the W boson, the selection of events with an energetic electron or muon and large missing transverse momentum, or $\ell + \not{P}_T$ events, is further restricted to events for which a reliable measurement of the charge of the isolated lepton exists. The reconstruction of the W boson rest frame is performed and the W boson differential cross section as a function of the decay angle θ^* is derived and used to extract the W boson polarisation fractions. In the last section, the evaluation of the systematic uncertainties on this measurement is presented.

9.1 W Boson Reconstruction

The main difficulty consists in the reconstruction of the undetected neutrino. When the event's Q^2 is large enough, the scattered electron can be detected. In this case the neutrino ν is the only missing particle and the event is said to be 'tagged'. If the scattered electron escapes down the beam-pipe, the event is 'untagged'. Tagged and untagged events are treated differently in the reconstruction process.

Tagged Events

When the event is tagged ($\sim 25\%$ of all events), it can be completely reconstructed. The transverse momentum components of the neutrino (ν), P_y^ν and P_x^ν, are determined by the missing P_T in the event using

$$\not{P}_T = \sqrt{\left(P_y^\nu\right)^2 + \left(P_x^\nu\right)^2}. \tag{9.1}$$

The longitudinal component $P_{z\nu}$ can be calculated using $E - P_Z$ conservation:

$$\begin{aligned} (E - P_z)_{\text{initial}} &= E_p - E_\text{e} - P_{z\,p} - P_{z\,\text{e}} = 2E_\text{e}, & (9.2)\\ (E - P_z)_{\text{final}} &= (E - P_z)_{\text{measured}} + (E - P_z)_\nu\,, & (9.3) \end{aligned}$$

where E_p, P_p, E_e and P_e are the scalar energies and momenta of the incoming proton and electron, respectively. Equating (9.2) with (9.3) leads to

$$(E - P_z)_\nu = 2E_e - (E - P_z)_{\text{measured}}\,. \tag{9.4}$$

The protons and electrons are assumed massless, hence $P^2 = 0 \Rightarrow E^2 = P^2$. The four vector of the W boson can be obtained by adding the four vectors of the isolated lepton and the reconstructed neutrino.

Untagged Events

In $\sim 75\%$ of the cases the scattered electron escapes down the beam-pipe and Equation (9.4) cannot be applied. For these 'untagged' events a W boson mass constraint is imposed to reconstruct the neutrino kinematics assuming a W boson in the event

$$M_W^2 = (P_\ell + P_\nu)^2 \simeq 2\,\bar{P}_\ell \cdot \bar{P}_\nu, \tag{9.5}$$

where ℓ and ν refer to the lepton and neutrino from the W boson decay. Both are assumed massless. Equation (9.5) can be written as a parabolic equation in $x \equiv (E - P_z)_\nu$

$$(E + P_z)_\nu = \frac{(E + P_z)_\nu\,(E - P_z)_\nu}{(E - P_z)_\nu} = \frac{(P_T^\nu)^2}{x}. \tag{9.6}$$

This allows to express E^ν and P_z^ν as:

$$E^\nu = \frac{1}{2}\left(x + (P_T^\nu)^2/x\right), \tag{9.7}$$

$$P^{z\nu} = \frac{1}{2}\left(P_T^\nu/x - x\right). \tag{9.8}$$

Together with Equation (9.5) this leads to a quadratic equation in the $(E - P_Z)$ of the neutrino

$$ax^2 + bx + c = 0, \tag{9.9}$$

where

$$\begin{aligned} a &= E^\ell - P_z^\ell, \\ b &= -2\left(P_x^\nu P_x^\ell + P_y^\nu P_y^\ell\right) - M_W^2, \\ c &= (P_T^\nu)^2\left(E^\ell - P_z^\ell\right), \end{aligned} \tag{9.10}$$

with solutions

$$x_{1,2} = \frac{-b \pm \sqrt{b^2 - 4ac}}{2a}. \tag{9.11}$$

When a solution corresponds to a negative energy, it is considered unphysical and will not be used.

Event Classification

Depending on the applied procedure to reconstruct the W boson, an event classification can be defined

I The event is tagged.
The MC predicts that 18% of the electron and 24% of the muon events are tagged. This difference is due to the absence of $\mu + \not{P}_T$ events with $P_T^X < 12$ GeV resulting in a larger rate of DIS events in this sample, for which the scattered electron is more likely to be detected.

Figure 9.1 (left) shows the reconstructed W boson mass for tagged MC events fit with a Gauss distribution. The W boson mass peaks around 80 GeV as expected. The worse resolution in the muon channel reflects the poorer muon momentum measurement.

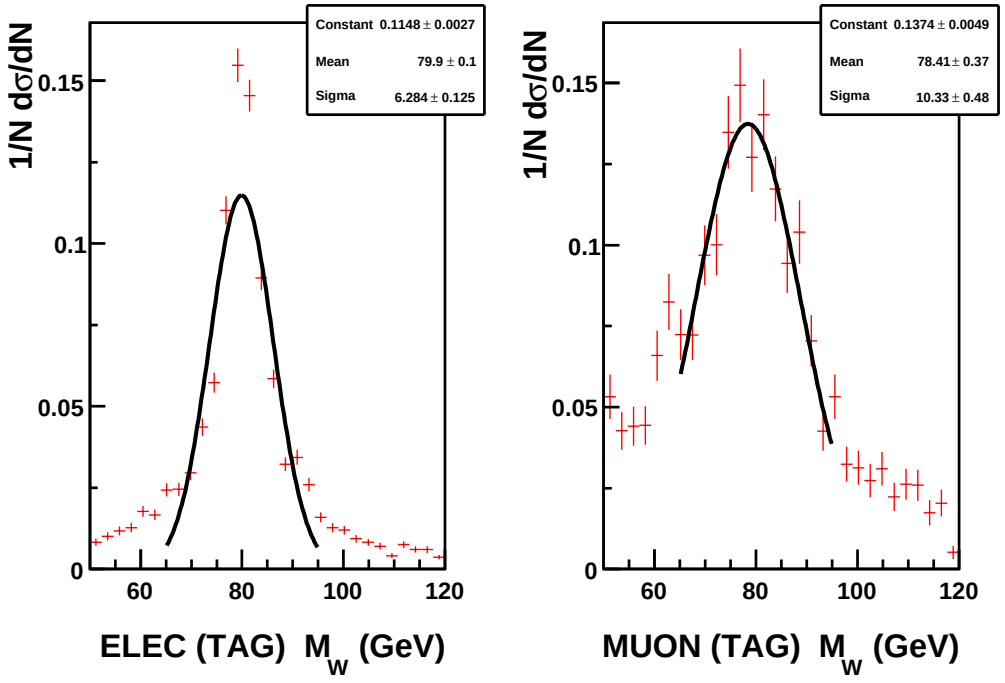

Figure 9.1: *The reconstructed W boson mass for tagged events generated with EPVEC in the electron (left) and muon (right) channels. A Gaussian is fit through the distributions to obtain a qualitative measure of the width and average value. The distributions are normalised to one.*

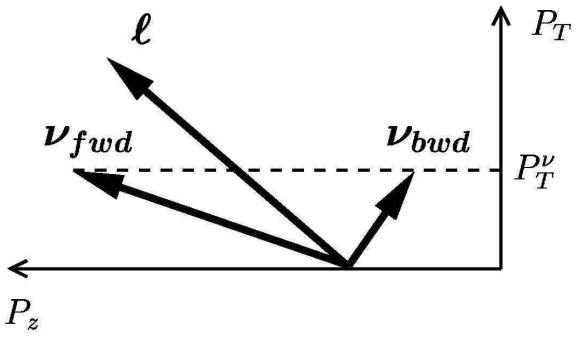

Figure 9.2: *Schematical representation of two different neutrinos satisfying the W mass constraint in the event.*

II Untagged event with complex solutions.
In 7% of the cases, the reconstructed events from EPVEC yield a complex solution to Equation (9.11). This is a result of fluctuations in the hadronic final state. For these events the imaginary part is ignored.

III Untagged event with only one physical solution.

Due to the large mass of the W boson, it does not happen that Equation (9.11) yields exactly one physical solution.

IV Untagged event with two physical solutions.
Mostly there are two possible solutions for a neutrino to satisfy Equation (9.11). The 'Forward' ('Backward') solution is defined as the solution for which the corresponding reconstructed neutrino has the larger (smaller) P_z. The corresponding neutrinos are called the 'forward' or 'backward' neutrinos. This is schematically shown in Figure 9.2. The strategy to choose the proper solution is based on the polar angle of the isolated lepton in the event θ^ℓ. From figure 9.3 (top) it can be seen that the distance of the forward neutrino to the generated neutrino (D_{FWD})

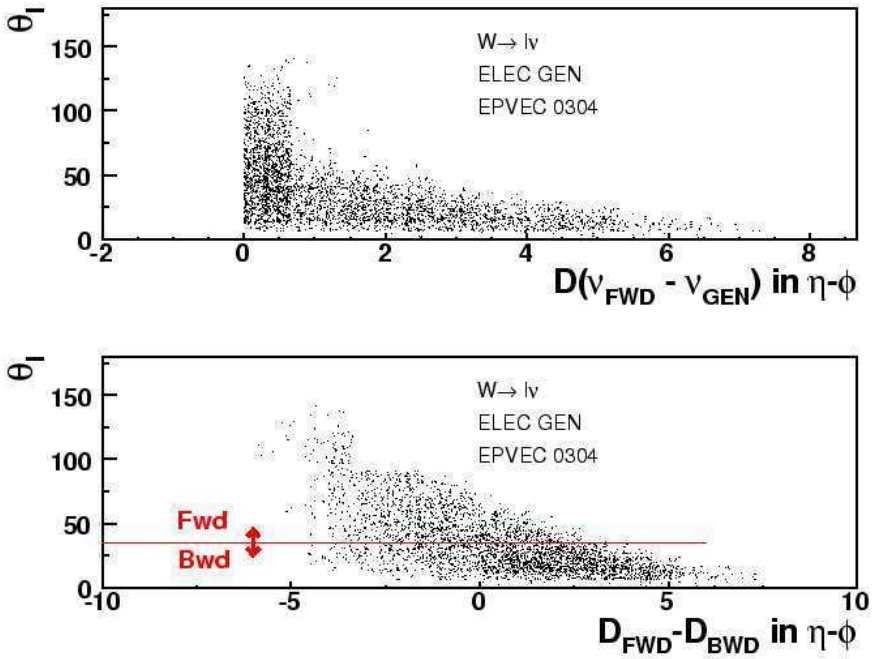

Figure 9.3: *Top: Distance in $\eta - \phi$ of the reconstructed forward neutrino to the generated neutrino in the decay $W \rightarrow \ell\nu$ correlated with the polar angle of the isolated lepton in the event θ^ℓ. Bottom: Correlation of $D_{FWD} - D_{BWD}$ with θ^ℓ, where D_{FWD} (D_{BWD}) is the distance in $\eta - \phi$ of the forward (backward) solution with the generated neutrino.*

decreases for decreasing θ^ℓ. This suggests that the choice can be based on the value of θ^ℓ. To analyse which value for θ^ℓ is optimal, θ^ℓ is correlated with $D_{FWD} - D_{BWD}$, see Figure 9.3 (bottom). Negative values for $D_{FWD} - D_{BWD}$ mean that the forward neutrino is closest to the generated neutrino. It is found that the success rate is optimal when the forward solution is chosen for $\theta^\ell > 35^o$.

Another strategy that is investigated makes use of the value of the total $E - P_Z$ in the event using either the forward or backward neutrino solution. The solution resulting in a value of $E - P_Z$ closest to 55 GeV, corresponds to the best solution.

The success rates of both methods are shown in Table 9.1. The best reconstruction is obtained

Decision method	Succes Rate (%) ELEC	MUON
θ_ℓ	0.78	0.84
$E - P_z$	0.77	0.80

Table 9.1: *Success rates in percent for choosing the proper neutrino solution for case IV events in the W boson reconstruction. Shown for the decision method where the choice is based on the isolated lepton's polar angle θ^ℓ, and for the method that uses the total $E - P_Z$ of the reconstructed event.*

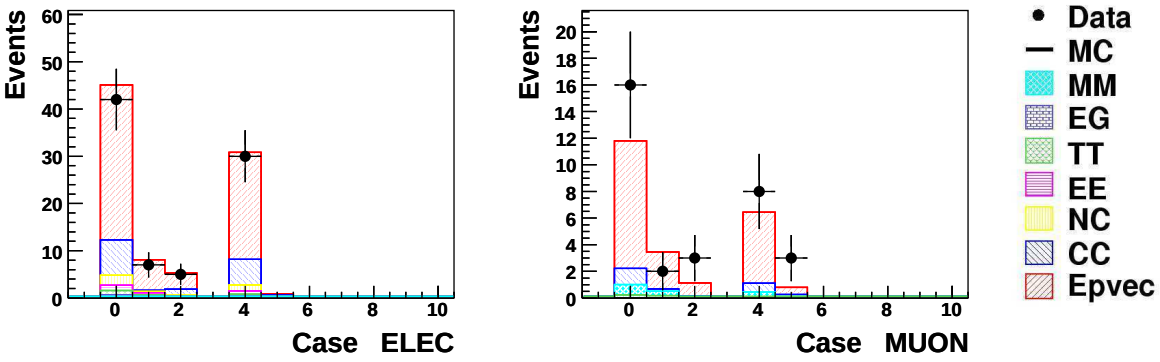

Case	Description
0	All events
1	Tagged
2	Complex
3	One solution
4	Two solutions
5	No solutions

Figure 9.4: *Top: the occurence of each case in the W boson reconstruction for data (points) and MC (open histograms) in the electron (left) and muon (middle) channels. The colour coding is explained (right) and a remainder of what each case means is provided in the table (lower left).*

by using θ^ℓ, which is the applied strategy in this work.

V Untagged with no physical solutions.
When the energies of both the forward and backward neutrino solutions are negative, there is no physical solution. When this occurs, the event rejected.

As shown in Figure 9.4, the rates of the above defined cases in the W boson reconstruction is well described by the MC. In both lepton channels, most events deliver two physical solutions for the neutrino (case IV). Tagged events (case I) and events with a complex solution (case II) occur less frequently.

For all $\ell + \not{P}_T$ events in the electron channel, a W boson rest frame can be reconstructed. In the muon channel, three events do not yield a physical neutrino. Therefore the W boson rest-frame cannot be reconstructed and these events are lost for the analysis.

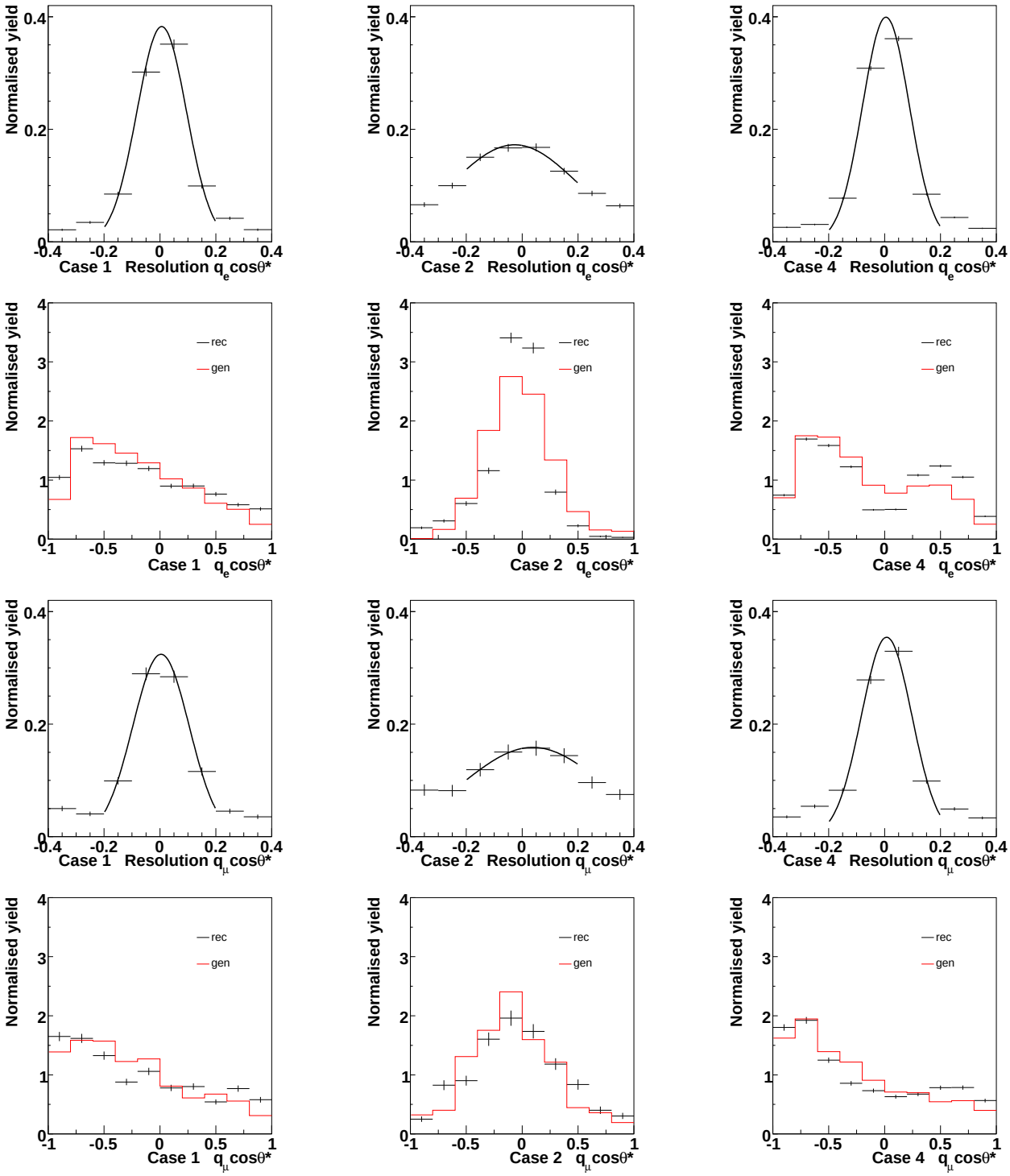

Figure 9.5: *Quality of the reconstruction of $q_\ell \cos\theta^*$ in the electron (top two rows) and the muon channels (lower two rows). In the first and third row the resolution for cases 1,2, and 4 fit with a Gaussian are shown. In the second and fourth row the generated (gen) and reconstructed (rec) distributions for $q_\ell \cos\theta^*$ are shown. All distributions are normalised. The error bars denote the statistical uncertainty.*

Reconstruction of θ^*

Once the W boson rest frame is reconstructed, the $\cos\theta^*$ is extracted. Here θ^* is the angle between the W boson three momentum in the laboratory frame and that of the charged decay lepton in the W boson rest frame. The quality of the reconstruction is presented in Figure 9.5 for the electron and muon channels. The $q_\ell \cos\theta^*$ distributions for Case I and Case IV events show the expected shape with the larger contributions at low values of $q_\ell \cos\theta^*$, representing the predominantly left handed W bosons. The $q_\ell \cos\theta^*$ is reconstructed with a resolution better than 0.1 in the cases I and IV in both lepton channels. In the electron channel an undershoot around $q_\ell \cos\theta^* = 0$ is observed. These are spill-over events that are reconstructed as Case II events. This is not observed in the muon channel, which can only be due to the low P_T^X events for which the reconstruction of the hadronic final state is worse. The reconstruction of these Case II events is, however, still acceptable, with a resolution $\sim$0.2.

9.2 Charge Measurement

The charge identification is important for the measurement of the W boson polarisation fractions, since $\cos\theta^*$ is weighed with the sign of the lepton charge $q_\ell = \pm 1$. A measure for the reliability of the charge measurement is provided by the 'charge significance'

$$\sigma_Q = \frac{|\kappa|}{d\kappa}, \tag{9.12}$$

where κ is the track curvature and $d\kappa$ is the uncertainty on κ. Tracks from high P_T particles can lead to small values of σ_Q, in which case there is a significant probability that the sign of the curvature is wrongly measured, resulting in the misidentification of the particle's charge.

To test the charge identification for high P_T particles, a standard high Q^2 NC sample with a purity of practically 100% is used. In addition to the NC selection cuts (described in Section A-1), the electrons are required to have $P_T >$ 10 GeV and the P_T as measured from the associated electron track (P_T^{track}) must match the calorimetric measurement (P_T^{calo}) with $1/P_T^{\text{track}} - 1/P_T^{\text{calo}} < 0.04$. This assures that both the track and the cluster can be attributed to the same electron [67]. This cut is also applied in the data sample, which will be used for the polarisation fractions.

In NC events (Section 2.3.2), the identified electron can only be the scattered electron and must have the same charge as the electron beam. Figure 9.6 shows the distribution of σ_Q, weighed with $Q^e Q^{\text{beam}}$ for the high Q^2 NC sample in the regions of $\theta_e < 20^o$, $20^o < \theta_e < 45^o$, and $45^o < \theta_e < 140^o$. Events for which the charge of the electron Q^e differs from that of the electron beam Q^{beam} are called 'wrong charge' events and have negative values for $Q_e Q_{\text{beam}} \sigma_Q$. In the region $\theta_e < 20^o$, the charge is misidentified in 25% of the events, therefore, this region is not further considered. For the region $20^o < \theta_e < 45^o$, where most of the $\ell + \not{P}_T$ events are concentrated, about 1.5% wrong-charge events are observed, while in the region $45^o < \theta_e < 140^o$, the wrong-charge events correspond to a negligible fraction of the total number of events ($> 2 \cdot 10^5$). A cut $\sigma_Q < 1$ is applied, which reduces the charge misidentification rate to less than 0.5% in the region $20^o < \theta_e < 45^o$. In this region, the selection efficiency of this cut is 98.9% in the NC data sample, well described by the MC within 1%.

The wrong-charge σ_Q distribution for reconstructed EPVEC events is shown in Figure 9.7 for both lepton channels. Here, σ_Q is weighed with the charge of the generated W boson Q_W^{gen} and that of the reconstructed isolated lepton in the event Q_ℓ, with $\ell = e$ or μ. Similar charge misidentification rates are obtained for EPVEC as for the NC MC. The predicted selection efficiency for the cut $\sigma_Q < 1$ is 97%. This is smaller than in the NC sample, which is attributed to the higher P_T tracks involved.

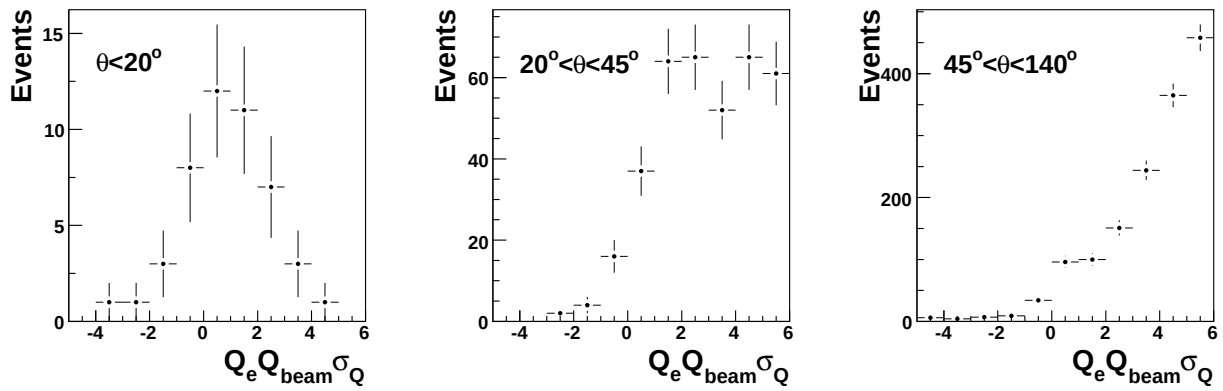

Figure 9.6: *The charge significance σ_Q weighed with the beam charge Q_{beam} and the electron charge Q_e for a high Q^2 NC data sample in the regions where the electron angle $\theta_e < 20^o$ (left), $20^o < \theta_e < 45^o$ (middle), and $45^o < \theta_e < 140^o$ (right). Only the region with small values for σ_Q (< 6) is shown.*

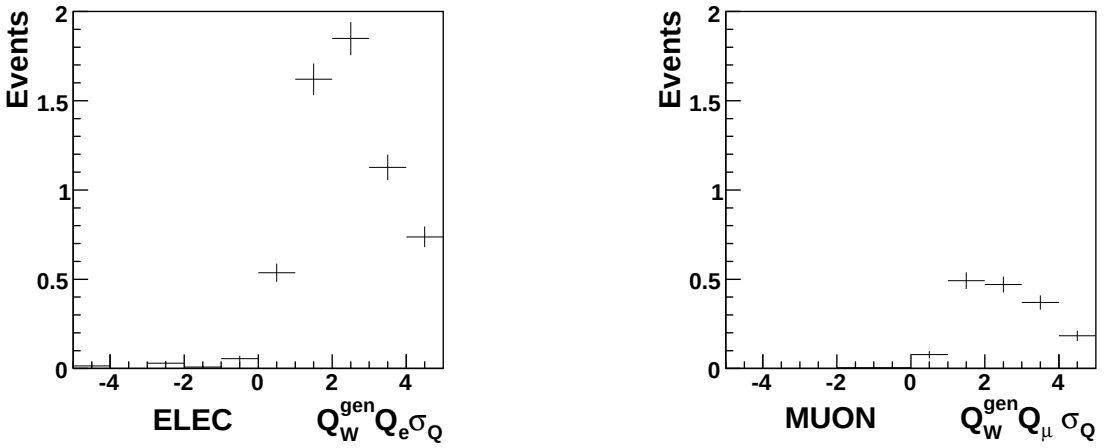

Figure 9.7: *The charge significance σ_Q weighed with the charge of the reconstructed electron Q_e (left) or muon Q_μ (right) and with that of the generated W boson in the event Q_W^{gen} for reconstructed EPVEC events (where only the decay $W \rightarrow e/\mu + \nu$ is considered) before cutting on σ_Q. Only the region with small values for σ_Q (< 5) is shown.*

The effect of this cut on the current data sample is shown in Figure 9.8, where σ_Q is displayed in the range $0 < \sigma_Q < 5$ for both $\theta_e < 20^o$ and $\theta_e > 20^o$, after successfully reconstructing the W boson rest-frame and applying the P_T matching criterion. In the forward region no events are kept and in the central region, one event is lost.

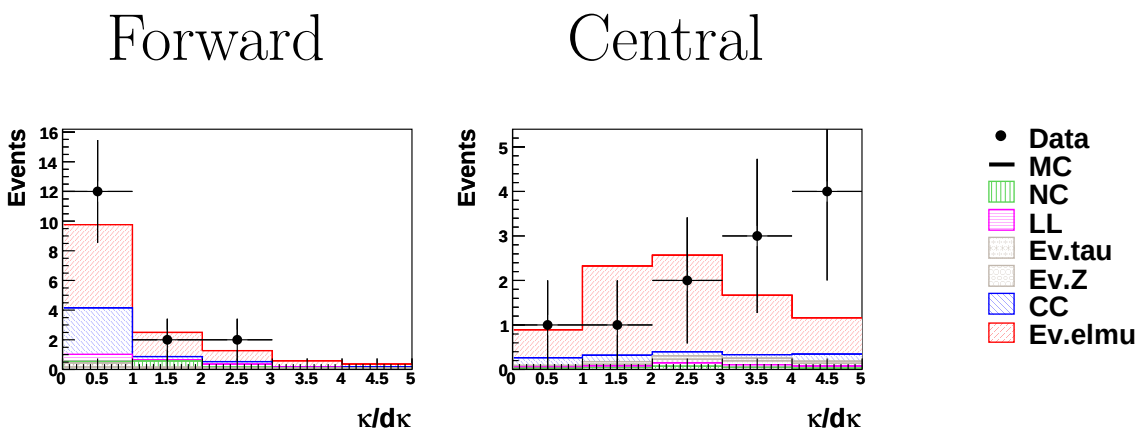

Figure 9.8: σ_Q *for* $0 < \sigma_Q < 5$ *in the forward (left) and central (right) regions for the data sample after successfully reconstructing the* W *boson rest-frame and applying the* P_T *matching criterion. The legend on the right contains the colour coding for all included processes: NC (NC), CC (CC), lepton pair production (LL), bremsstrahlung (EG), and single* W *and* Z *boson production (Epvec).*

%	Data				Welmu		Wtau		WZ		CC		NC		LL	
Cut	e		μ		e	μ	e	μ	e	μ	e	μ	e	μ	e	μ
None	100	(42)	100	(16)	100	100	100	100	100	100	100	100	100	0	100	100
W	100	(42)	81	(13)	99	94	99	99	93	100	91	82	99	0	99	96
P_T^{Match}	85	(36)	81	(13)	85	94	79	99	66	100	62	82	87	0	80	96
$\theta_\ell < 20^o$	52	(22)	62	(10)	59	76	50	81	51	64	20	8	67	0	49	70
$\sigma_Q < 1$	50	(21)	62	(10)	57	75	50	81	50	64	18	5	66	0	48	68

Table 9.2: *Cut flow in both lepton channels for data and MC. The numbers denote the percentage of the initial* $\ell + \not{P}_T$ *sample (Chapter 6) that is left after applying the corresponding cut. For the data, the number of events is shown in parentheses. The final sample is used to extract the polarisation fractions.*

9.3 Final Sample for the W Boson Polarisation Measurement

The final sample for the W boson polarisation measurement consists of 21 electron and 10 muon events with an estimated over-all signal purity of 74%. Table 9.2 shows the cut flow in the selection of the data and MC, starting from the $\ell + \not{P}_T$ sample (Chapter 6). Three muon events are lost because the W boson rest-frame could not be reconstructed. 6 events fail the matching requirement of the P_T's of tracks and clusters, which is only applied in the electron channel. Another 14 electron and 3 muon events are lost to the forward region $\theta^\ell < 20^o$. One electron event is lost by requiring $\sigma_Q > 1$. The yield as a function of $q_\ell \cos\theta^*$ for the resulting final sample is well described by the MC, as is shown in Figure 9.9 and Table 9.3. Events in the electron and muon channels, originating from the decay $W \to \tau\,(\to e/\mu + \nu) + \nu$, are considered as background, since for these events the $\cos\theta^*$ distributions

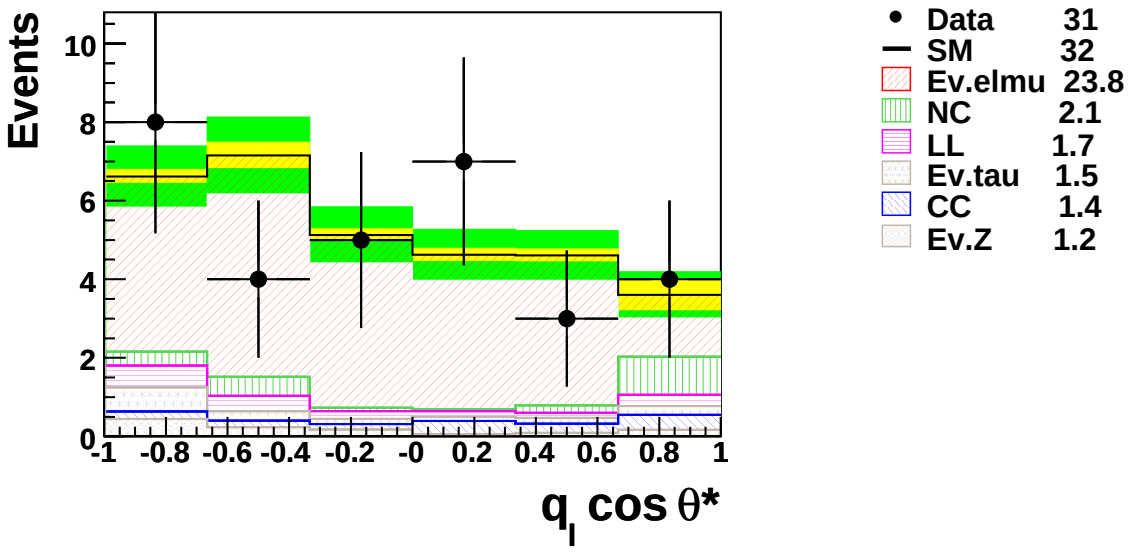

Figure 9.9: *The data yield (points) in bins of $q_\ell \cos\theta^*$ compared to the SM expectation (open histogram). The shaded inner regions around the open histogram line denote the statistical uncertainty and the darker regions the total uncertainty. The seperate SM contributions are also shown with their explicit contributions in the legend on the right. These include the CC (CC), NC and bremsstrahlung (NC), lepton pair production (LL) and the single W boson production processes with the decay $W \to e/\mu + \nu$ (Ev.elmu) and $W \to \tau + \nu$ (Ev.tau), and Z boson production with the decay $Z \to \nu\bar{\nu}$ (Ev.Z).*

are not expected to be described by relation (3.12).

9.4 Extraction of the W Boson Polarisation Fractions

The measured $q_\ell \cos\theta^*$ distribution is corrected for acceptance and detector effects, using the same method as the one applied to determine the differential $\ell + \not{P}_T$ cross section as a function of P_T^X (Section 7.3). The stability and purity of the bins is shown in Figure 9.10. Both are critically low in the last two bins, which means that the over-all reconstruction resolution of 0.2 (Figure 9.5) does not allow for more bins. The acceptances are shown in Figure 9.11. In the electron channel, the selection efficiency is pronounced in the center, due to contributions from events at low P_T^X ($\sim P_T^W$), whereas in the muon channel it is flat.

The resulting differential cross section as a function of $q_\ell \cos\theta^*$, further referred to as $d\sigma_W/d\,(q_\ell \cos\theta^*)$, is shown on the left hand side of Figure 9.12 and is tabulated in Table 9.4. No deviations from the SM are observed. The corresponding integrated single W boson production cross section of

$$1.19 \pm 0.37\,(\text{stat}) \pm 0.13\,(\text{sys})\ \text{pb}, \tag{9.13}$$

is consistent with the previously derived value of $\sigma_W = 1.23 \pm 0.25\,(\text{stat}) + 0.13\,(\text{sys})$ pb (Section 7.4).

As explained in Section 3.5, the off-shell W boson are not expected to follow the predicted polarisation behaviour of Equation (3.12). Therefore, the measured values of $d\sigma_W/d\,(q_\ell \cos\theta^*)$ are multiplied

$\text{Rates}^{(e^{\pm}p)}_{q_l cos\,\theta*}$	**H1 Data**	**SM exp**	**SM sig**	**SM bg**
-1 – -0.67	8	6.62 ± 0.74	4.46 ± 0.69	2.16 ± 0.20
-0.67 – -0.33	4	7.15 ± 0.91	5.63 ± 0.87	1.52 ± 0.18
-0.33 – 0	5	5.13 ± 0.69	4.40 ± 0.68	0.73 ± 0.08
0 – 0.33	7	4.62 ± 0.63	3.93 ± 0.61	0.70 ± 0.11
0.33 – 0.67	3	4.61 ± 0.61	3.82 ± 0.59	0.79 ± 0.09
0.67 – 1.0	4	3.60 ± 0.40	1.58 ± 0.25	2.03 ± 0.30

Table 9.3: *The data yield (points) in bins of $q_\ell \cos\theta^*$ compared to the SM prediction (SM exp). Also shown are the separate SM signal (SM sig) and SM background (SM bg) contributions. The errors denote the total uncertainty on the given numbers. The row marked with $\int$ denotes the total yield.*

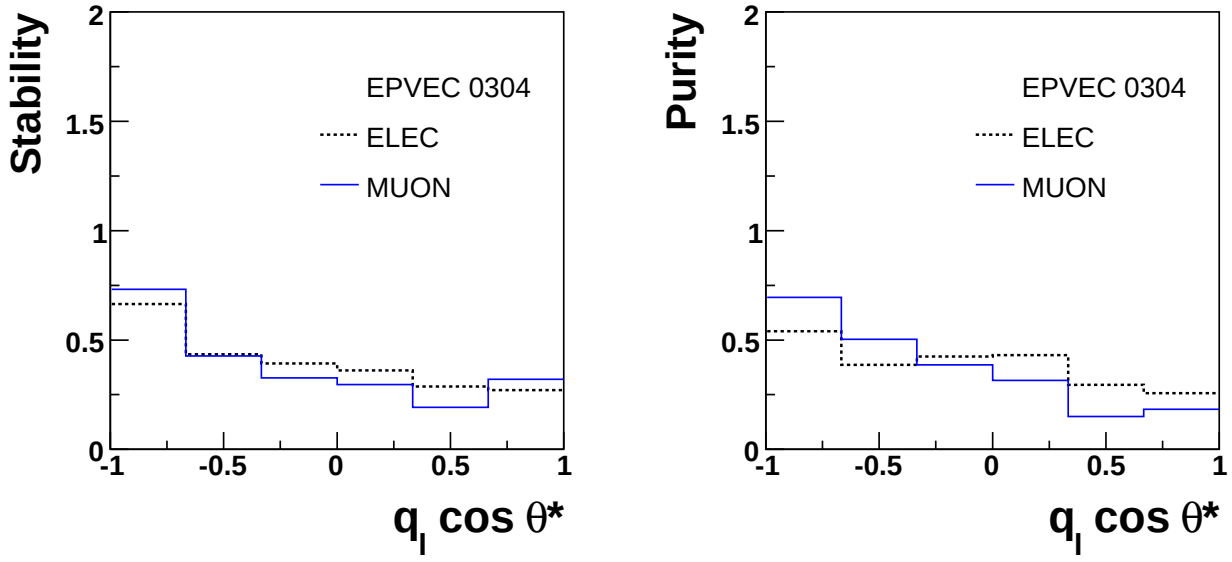

Figure 9.10: *Stability (left) and purity (right) for each bin in $q_\ell \cos\theta^*$. Calculated with reconstructed events from EPVEC.*

$\frac{d\sigma}{d(q_l cos\,\theta*)}^{(e^{\pm}p)}(fb)$	**Measured ± stat ± sys**	**SM ± th sys**
-1 – -0.67	$1312 \pm 900 \pm 136$	1144 ± 172
-0.67 – -0.33	$392 \pm 308 \pm 63$	829 ± 124
-0.33 – 0	$602 \pm 338 \pm 42$	628 ± 94
0 – 0.33	$583 \pm 267 \pm 43$	490 ± 74
0.33 – 0.67	$292 \pm 208 \pm 23$	428 ± 64
0.67 – 1.0	$391 \pm 306 \pm 88$	400 ± 60

Table 9.4: *Results for the differential cross section measurement as a function of $q_\ell \cos\theta^*$ shown with the statistical (stat) and systematic (sys) uncertainty. Also shown is the SM prediction (SM) with the theoretical systematic uncertainty (th sys).*

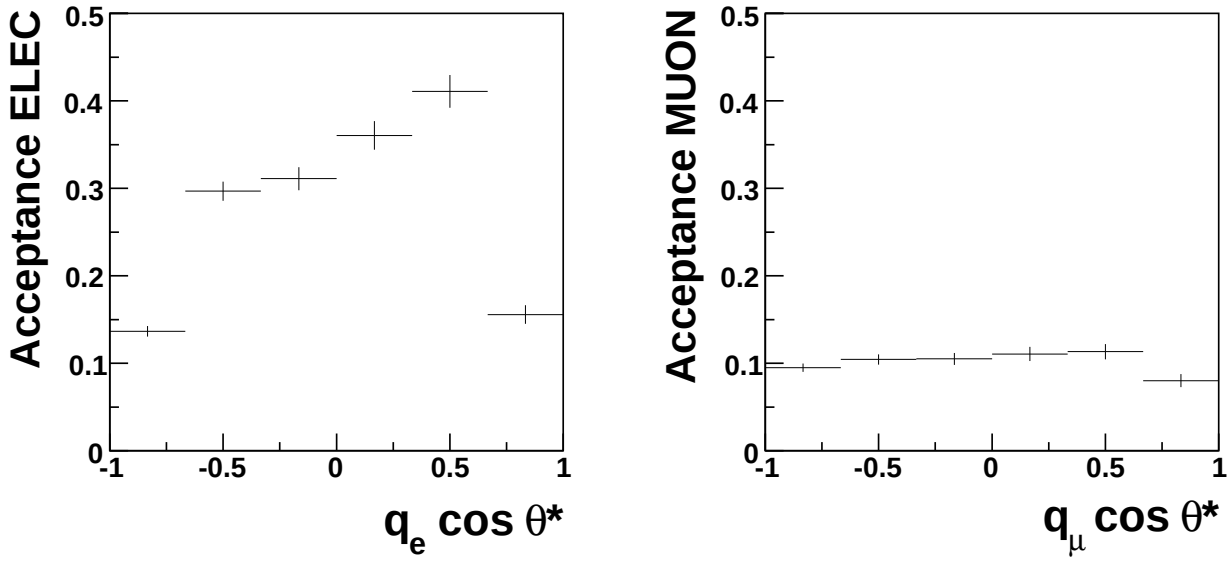

Figure 9.11: *Acceptances in the electron (left) and muon (right) channels in bins of $q_\ell \cos\theta^*$ estimated with reconstructed events from EPVEC. The error bars indicate the statistical uncertainty.*

by the correction-factors from Table 3.2 in each bin. The resulting distribution is fit to the model defined in Equation (3.12). Since the data is binned, Equation (3.12) is integrated in each bin i, which leads to a linear dependence of σ_W on F_0 and F_-

$$\sigma_W = A\left[(1 - F_0 - F_-)\cdot f_i^+ + F_0 \cdot f_i^0 + F_- \cdot f_i^-\right], \tag{9.14}$$

where A is an over-all normalisation parameter, which is kept free in the fit to avoid biasing among bins. f_+^i , f_0^i and f_-^i are defined as:

$$\begin{aligned} f_+^i &= \int_{a_i}^{b_i} \frac{3}{4}\left(1-\cos^2\theta^*\right) d\cos\,\theta^*, \\ f_0^i &= \int_{a_i}^{b_i} \frac{3}{8}\left(1-\cos\,\theta^*\right)^2 d\cos\,\theta^*, \\ f_-^i &= \int_{a_i}^{b_i} \frac{3}{4}\left(1+\cos^2\theta^*\right) d\cos\,\theta^*, \end{aligned} \tag{9.15}$$

where a_i (b_i) is the lower (upper) edge of the i^{th} bin. The optimal values for the free parameters in the fit are found using the `MINUIT` package [68], which uses a χ^2 minimisation scheme (MIGRAD). This means that for each pair F_- and F_0 the quantity $\chi^2(F_-, F_0)$ is determined:

$$\chi^2\left(F_-, F_0\right) = \prod_{i=1}^{N_{\text{bins}}} \left(\frac{\delta\sigma_i^{\text{Data}} - \delta\sigma\left(F_-, F_0\right)_i^{\text{Theory}}}{\Delta\delta\sigma_i^{\text{Data}}}\right)^2, \tag{9.16}$$

where $\delta\sigma^{\text{Data}}$ denotes the measured $d\sigma_W/d\left(q_\ell\cos\theta^*\right)$ and $\delta\sigma^{\text{Theory}}\left(F_-, F_0\right)$ denotes the predicted $d\sigma_W/d\left(q_\ell\cos\theta^*\right)$ as a function of F_- and F_0. $\Delta\delta\sigma^{\text{Data}}$ denotes the total measurement uncertainty

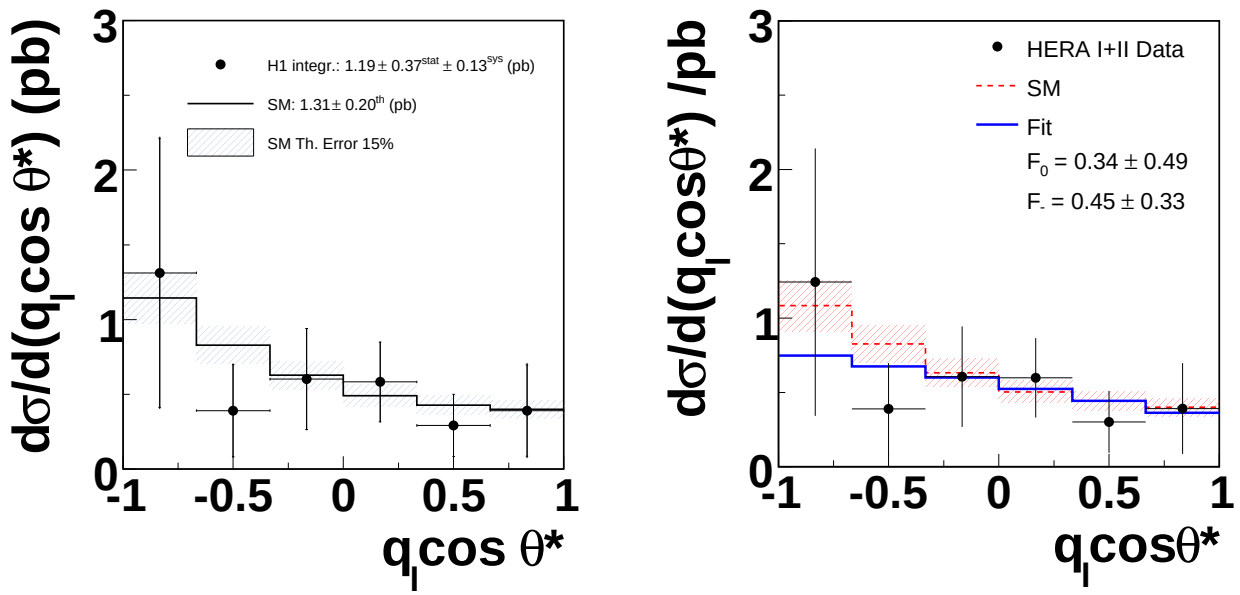

Figure 9.12: *Left: Derived $d\sigma_W/d\,(q_\ell \cos\theta^*)$ (points). The dashes (bars) denote the statistical (total) uncertainties. The EPVEC prediction (open histogram) is also shown, which has a 15% theoretical uncertainty (hatched). The numerical values of the integrated cross section is shown for the data (H1 integr.) and SM (SM) with corresponding uncertainties.*
Right: Derived $d\sigma_W/d\,(q_\ell \cos\theta^*)$ corrected for off-shell W bosons (points) with statistical uncertainties (bars) together with the SM expectation (dashed) with theoretical uncertainty (hatched) and the unscaled fit result (open histogram). The values from the fit for F_- and F_0 are shown with statistical errors corresponding to one standard deviation.

on $d\sigma_W/d\,(q_\ell \cos\theta^*)$. The minimal value of χ^2 defines the optimal values for F_- and F_0 in the fit. In the extraction of F_- and F_0, `MINUIT` is called twice. In the first step the optimal value for A is determined, which is 0.826 ± 0.261. The large error estimate indicates that the fit is not sensitive to the value of A. In the second iteration step, A is fixed and F_- and F_0 are simultaneously extracted while keeping both parameters free. The fit is shown on the right hand side of Figure 9.12 together with the measured $d\sigma_W/d\,(q_\ell \cos\theta^*)$, corrected for off-shell W bosons. Even though the data point in the first bin from the left is above the SM prediction, the fit is even lower. This is due to the point in the second bin, which is below the expectation and the point in the fourth bin, which is measured with better accuracy. Latter bin thus 'pulls the fit' and the obtained value for F_- is lower than the SM expectation. The correlation coefficient between F_- and F_0 is -0.87 and the fit results are

$$F_- = 0.34 \pm 0.49\,(\text{stat}) \; +0.04 - 0.05\,(\text{sys}), \tag{9.17}$$

$$F_0 = 0.45 \pm 0.33\,(\text{stat}) \; +0.05 - 0.05\,(\text{sys}). \tag{9.18}$$

The systematic uncertainties are discussed explicitely in Section 9.5. The statistical uncertainties correspond to one standard deviation, in the case of an unconstrained fit (39% CL). However, F_- and

F_0 are constrained to their physically allowed values, which define the domain

$$\begin{aligned} 0 < \quad & F_- \quad & < 1, \\ 0 < \quad & F_0 \quad & < 1, \\ 0 < \quad & F_- + F_0 \quad & < 1. \end{aligned} \tag{9.19}$$

The determination of the true 68% and 95% confidence levels (CL) is calculated explicitly by renormalising the probability density inside the domain (9.19). The CL corresponding to the region inside a contour of constant χ^2 around the optimal values for the parameters is given by [69]

$$CL\left(\chi^2\right) = \int_0^{\chi^2} f\left(\chi'^2\right) d\chi'^2, \tag{9.20}$$

where $f\left(\chi'^2\right)$ is the probability density:

$$f\left(\chi^2\right) = \frac{\frac{1}{2}\left(\chi^2/2\right)^{n/2-1} e^{-\chi^2/2}}{\Gamma\left(n/2\right)}, \tag{9.21}$$

with $\Gamma\left(\chi^2\right)$ the Gamma function, defined as $\Gamma\left(x+1\right) = x!$. n corresponds to the number of free parameters in the fit, which is 2 in this case.

Using Equation (9.20), the CL in the physically allowed region (9.19) can be expressed as:

$$CL\left(\chi^2\left(F_-, F_0\right)\right) = \frac{\int_0^{\chi^2} f\left(\chi^2\left(F_-, F_0\right)\right) \pi\left(F_-, F_0\right) d\chi^2}{\int_0^{\chi^2_{\max}} f\left(\chi^2\left(F_-, F_0\right)\right) \pi\left(F_-, F_0\right) d\chi^2}, \tag{9.22}$$

where $\pi\left(F_-, F_0\right)$ is 0 if the pair F_- and F_0 is outside the allowed region and 1 otherwise. $\chi^2_{\max}$ is any value of χ^2 for which $CL\left(\chi^2_{\max}\right) = 1$.

The determination of the 68% and 95% CL contours is performed in three steps. First, the value of χ^2 is evaluated using Equation (9.16) on a grid of 250 by 250 equidistant points covering the domain

$$\begin{aligned} F_- &= [-1, 2] \\ F_0 &= [-2, 2.5]\,. \end{aligned} \tag{9.23}$$

This domain must be large enough to fully contain the contour at ${\chi^2}_{\max}$. This procedure provides a method to cross-check the optimal values for F_- and F_0, as given by MINUIT (Equations (9.17) and (9.18)). Indeed the results are fully consistent. In the second step, the resulting χ^2 distribution is used to construct a radial grid with 102 equi distant contours in χ^2. ${\chi^2}_{\max}$ is determined as the smallest value of χ^2, for which the value of

$$\sum_{i=2}^{i=102} CL_i\left(\chi^2_i\right) - CL_{i-1}\left(\chi^2_{i-1}\right) = 0.999. \tag{9.24}$$

${\chi^2}_{\max}$ is 13.72 and the corresponding contour is indeed fully contained in the domain of Equation (9.23). The normalisation term in the denominator of Equation (9.22) is determined by performing the integration of Equation (9.24) again, taking into account the physical region for F_- and F_0

$$\sum_{i=2}^{i=102} \left(CL_i\left(\chi^2_i\right) - CL_{i-1}\left(\chi^2_{i-1}\right)\right) \cdot \mathrm{F}\left(F_-, F_0\right) \tag{9.25}$$

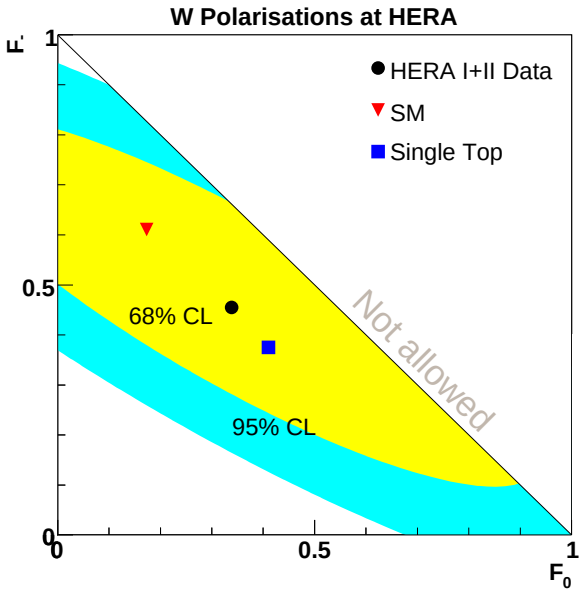

Figure 9.13: *Measured values for F_- and F_0 (point) with the 68% and 95% CL contours. Also shown are the predicted values for the SM (triangle) and anomalous single top production via FCNC (square).*

where $\mathrm{F}(F_-, F_0)$ is the fraction of the contour circomference within the physically allowed region. The result of Integration (9.25) corresponds to a total probability of 0.4545 and the contours for which integral Equation (9.25) first exceeds 68% and 95% of this number define the 68% and 95% CL contours, respectively.

The result is shown in Figure 9.13 and is in good agreement with the SM. This measurement is statistically limited and the result is also compatible with anomalous single top production via FCNC within 68% CL (the polarisation fractions of this process were discussed in Section 3.5).

The single parameter limits on F_- and F_0 are also extracted in fits where one parameter is fixed to its SM value and the other is fit, and vice versa

$$F_- = 0.56 \pm 0.16\,(\mathrm{stat}) + 0.02 - 0.02\,(\mathrm{sys}), \quad (9.26)$$

$$F_0 = 0.14 \pm 0.23\,(\mathrm{stat}) + 0.01 - 0.01\,(\mathrm{sys}), \quad (9.27)$$

$$(9.28)$$

The `MINUIT` package is used for the error estimates. `MINUIT` gives symmetric errors because the fit is performed without constraining F_- and F_0 to their physical regions. The results are in agreement with the SM.

Two cross-checks are performed, which give confidence about the stability of the fit results. All results are cross-checked by `MINUIT` using HESSE [68] and are fully consistent. In addition, the two parameter fits are also performed with F_- and F_+, and F_+ and F_0 as free parameters. The results are fully consistent.

ONE parameter fit

Source	$\mathbf{d}F_0^{up}$	$\mathbf{d}F_0^{dn}$	$\mathbf{d}F_-^{up}$	$\mathbf{d}F_-^{dn}$
Theory	0.006	0.006	0.001	0.001
Trigger	0.004	0.004	0.007	0.007
Track/Clus Lnk	0.004	0.004	0.007	0.007
Elec ID	0.004	0.004	0.007	0.007
Muon ID	0.004	0.004	0.007	0.007
Bgnd anti-corr	0.006	0.006	0.009	0.009
Charge	-	0.008	-	0.005
On-/Off-shell	$< 1\%$			
Total	0.012	0.014	0.017	0.017

TWO parameter fit

Source	$\mathbf{d}F_0^{up}$	$\mathbf{d}F_0^{dn}$	$\mathbf{d}F_-^{up}$	$\mathbf{d}F_-^{dn}$
Theory	0.022	0.022	0.013	0.013
Trigger	0.020	0.019	0.018	0.019
Trk/Clus Lnk	0.020	0.019	0.018	0.019
Elec ID	0.020	0.019	0.018	0.019
Muon ID	0.020	0.019	0.018	0.019
Bgnd anti-corr	0.022	0.022	0.022	0.022
Charge	-	0.005	-	0.003
On/Off-shell	$< 1\%$			
Total	0.051	0.049	0.044	0.046

Table 9.5: *Systematic uncertainties on the W boson polarisation fractions F_- and F_0 in the single parameter (left) and two parameter (right) fits. Starting from the top: Theory, Trigger, Track/Cluster linking, electron identification, muon identification, Background anti-correlated, the uncertainty on the correction for off-shell W bosons (negligible), and the systematic uncertainty on the charge identification, which is asymmetric.*

9.5 Systematic Uncertainties

The systematic uncertainties on F_- and F_0 are determined as follows: $d\sigma_W/d\,(q_\ell \cos\theta^*)$ is re-evaluated after shifting each systematic by ± 1 standard deviation

$$\sigma_{\rm sys} \tag{9.29}$$

in each bin. The result is fit to the model (relation 3.12) extracting the shifted values $F^{\rm up}$ and $F^{\rm dn}$ for F_0 and F_-. Here $F^{\rm up} - F^{\rm c} > 0$ and $F^{\rm dn} - F^{\rm c} < 0$ where $F^{\rm c}$ denotes the measured central values for F_- and F_0. The quoted uncertainties are defined as

$$\begin{aligned} dF_-^{\rm up\ (dn)} &= \left| F_-^{\rm up\ (dn)} - F_- \right| \\ dF_0^{\rm up\ (dn)} &= \left| F_0^{\rm up\ (dn)} - F_0 \right|. \end{aligned} \tag{9.30}$$

The systematic uncertainties in the efficiencies of the trigger, track cluster linking, electron and muon identification are similar and therefore evaluated only once. They were established in the differential cross section measurement as a function of P_T^X (Chapter 7). This is also true for the combined theoretical uncertainty on the calculations from the MC generators. The effect of the systematic uncertainties on the shape of $d\sigma_W/d\,(q_\ell \cos\theta^*)$ from uncertainties on the background estimates and charge misidentification are discussed separately below. The results are summarised in Table 9.5.

SM Background

Fluctuations in the SM background estimates can distort the shape of $d\sigma_W/d\,(q_\ell \cos\theta^*)$ and are expected to have an additional systematic effect on the fit result. This is estimated below, using the distributions for $q_\ell \cos\theta^*$, which are shown in Figure 9.14 for the so-called 'enriched' control samples (the applied cuts are described in Appendix A-1). Each sample omits certain kinematic cuts with respect to the final sample to select one background process. The data is taken in the years 2003-2005 and corresponds to an integrated luminosity of 169 pb^{-1}.

As shown in the figure, the NC enriched sample is described within the quoted 30%. A minor effect on the shape of the $q_\ell \cos\theta^*$ distribution can be seen due to a slight underestimation in the outer bins and overestimation in the center bins.

The CC enriched sample in the electron channel is overestimated. These events are concentrated in the forward region and it is difficult to collect statistics.

The CC enriched sample in the muon channel is well described by the MC. The CC events are concentrated in the most outer bins, thus the systematic uncertainty on the production cross section affects the measurement of F_- and F_0.

The lepton pair (LL) enriched sample is reasonably described by the MC. As in the case for the CC enriched sample, largest contributions occur in the outer most bins and have potentially a systematic effect on the shape.

For the 'background anti-correlated' entry in Table 9.5 it is assumed that the background estimation is wrong by $\sim$30% in such a way that it affects the shape of $d\sigma_W/d\,(q_\ell \cos\theta^*)$ rather than the yield. In the procedure to determine the systematic uncertainties on F_- and F_0, each bin is assigned a value for the standard deviation σ_{sys} (Equation (9.29)), ranging from +5% of the total yield in the first bin to -5% of that in the last bin and vice versa.

Off-Shell W bosons

In the procedure to determine the systematic uncertainties on F_- and F_0 originating from the correction for off-shell W bosons, the statistical uncertainty on the correction factors from Table 3.3 is used for σ_{sys} in each bin of $d\sigma_W/d\,(q_\ell \cos\theta^*)$. The effect is $< 1\%$ and is ignored.

Charge Misidentification

As discussed in Section 9.2, the charge misidentification in the final sample is well below 1%. A conservative charge misidentification of 1% is assumed. To assess the impact of 1% charge misidentification on the fit result, a MC sample is taken where $\sigma_Q > 2$. The charge misidentification in this sample is $\simeq 0.10\%$ at 95% CL. For a randomly chosen 1% of the events in this sample, the measured lepton charge is multiplied with -1 (wrong charge). The effect is shown in Figure 9.15. The measured values for $d\sigma_W/d\,(q_\ell \cos\theta^*)$ in each bin are multiplied with the factors shown in the figure and the systematic uncertainties for F_- and F_0 are extracted.

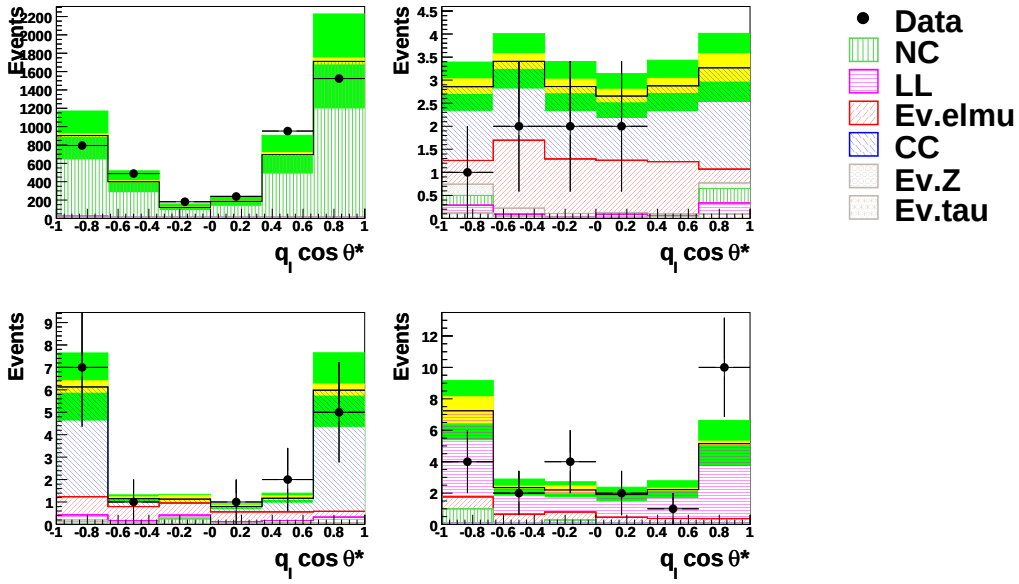

Figure 9.14: *The $q_\ell \cos\theta^*$ distribution in the enriched data control samples in the electron channel (top row): NC (left) and CC (right) and in the muon channel (bottom row): CC (left) and LL (right). The data (dots) are compared to the sum-total of the SM prediction.*

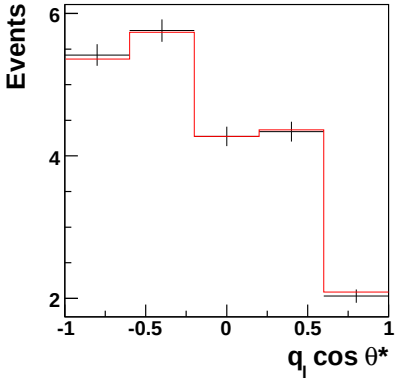

bin:	1	2	3	4	5
Effect:	-0.0105	-0.0042	0.0000	0.0056	0.0281

Figure 9.15: *Arbitrarily scaled $q_\ell \cos\theta^*$ distribution (left) in a sample where $\sigma_Q > 2$ for which the charge identification is $\simeq 100\%$ (histogram with error bars) and in the same sample, where an artificial charge misidentification of 1% is applied (open histogram without error bars). The relative effect of the 1% charge misidentification per bin is presented in the table (right).*

10 Discussion and Conclusions

10.1 Measurement of the $\ell + \not{P}_T$ Production Cross Section

The data sample collected in $e^{\pm}p$ collisions at HERA by the H1 experiment corresponding to an integrated luminosity $\mathcal{L} = 0.5$ fb^{-1} has been used to measure events with an isolated, energetic lepton (electron or muon) with large transverse missing momentum ($\ell + \not{P}_T$ events). In total 58 events are selected for a SM prediction of 57.4±7.3. The prediction is dominated within the SM by the production of single W bosons at the 75% level. In the e^+p data set (295 pb^{-1}) 43 events are found for a SM prediction of 34.6 ± 4.4 while in the e^-p data set (186 pb^{-1}) 15 events are found for a SM prediction of 22.8. An excess of events above the SM expectation is observed in the e^+p data set for events with $P_T^X > 25$ GeV: 17 events are observed for a SM prediction of 8.4 ± 1.2 corresponding to a 2.3σ excess.

The total event sample is used to determine a model-independent production cross section for $\ell + \not{P}_T$ events at HERA

$$\sigma_{\ell+\not{P}_T} = 0.24 \pm 0.05\,(\text{stat}) \pm 0.04\,(\text{sys}) \quad \text{pb}. \tag{10.1}$$

This agrees with the SM prediction of 0.26 ± 0.04 pb, and is consistent with the previously published HERA I result, which was based on a data sample of 118.3 pb^{-1} [11].

The $\ell + \not{P}_T$ cross section has been measured differentially as a function of P_T^X (Section 7.3). This measurement (Table 10.1) is in agreement with the previously published result and has better precision.

$\frac{d\sigma_{\ell+\not{P}_T}^{(e^{\pm}p)}}{dP_T^X}(\frac{fb}{GeV})$		**Measured ± stat ± sys**	**SM ± th sys**
0 –	12	$10.13 \pm 3.20 \pm 1.75$	13.50 ± 2.02
12 –	25	$5.35 \pm 1.59 \pm 0.73$	3.72 ± 0.56
25 –	40	$2.06 \pm 0.87 \pm 0.32$	1.92 ± 0.29
40 –	80	$0.63 \pm 0.28 \pm 0.09$	0.45 ± 0.07

Table 10.1: *Derived values for the differential $\ell + \not{P}_T$ cross section in bins of P_T^X with statistical (stat) and systematic (sys) uncertainties, compared to the SM prediction with the theoretical systematic uncertainty (th.sys).*

10.2 Measurement of Single W boson Production at HERA

The measurement of $\ell + \not{P}_T$ events is also used to determine the first significant production cross section for single W bosons at HERA

$$\sigma_W = 1.23 \pm 0.25\,(\text{stat}) + 0.13\,(\text{sys}) \ \text{pb}, \tag{10.2}$$

which is in good agreement with the SM expectation $\sigma_W^{\text{SM}} = 1.31 \pm 0.20$ pb.[1]

[1] For completeness it should be noted that ZEUS quoted [62] a W boson production cross section using 47.7 pb^{-1} of HERA I data at $\sqrt{s} = 300$ GeV of $\sigma_W = 0.9 + 1.0 - 0.7\,(\text{stat}) \pm 0.2\,(\text{sys})$ pb using three events with an isolated

10.3 Measurement of the $WW\gamma$ Vertex

The single W boson production cross section at HERA is predicted to be sensitive to the $WW\gamma$ vertex. In particular to the anomalous couplings $1 + d\kappa$ and λ, which are investigated in the present work. The investigation of these parameters, using an unbinned likelihood fit, was presented in Chapter 8. The measurement was performed in the full phase space as well as at $P_T^X > 12$ GeV. The measurement in the latter region of phase space showed most sensitivity to $d\kappa$ and λ. Fixing λ to its SM value, disjoint intervals are allowed for $d\kappa$ at 95% CL

$$-4.9 < d\kappa < -2.7 \quad \text{and} \quad -0.8 < d\kappa < 1.5. \tag{10.3}$$

If $d\kappa$ is fixed to zero, the interval of the parameter λ at 95% CL is

$$-2.9 < \lambda < 2.9. \tag{10.4}$$

When both parameters are allowed to vary in the fit, the two dimensional 95% CL limits are

$$-5.0 < d\kappa < 1.3, \tag{10.5}$$
$$-4.2 < \lambda < 3.8. \tag{10.6}$$

The only published single parameter limits on $d\kappa$ and λ at HERA were set by ZEUS [62]

$$\begin{aligned} -4.7 < d\kappa < 1.5, \\ -3.2 < \lambda < 3.2, \end{aligned} \tag{10.7}$$

at 95% CL. The ZEUS limits result from the non-observation of any events above $P_T^X = 20$ GeV leading to an upper limit of the measured σ_W of 0.58 pb. In addition, the theoretical uncertainty on the cross section calculation, was not taken into account [70], whereas in the current analysis, this is the dominant uncertainty (Table 8.4).

The larger statistical accuracy for the current measurement yields a better limit on $d\kappa$, despite the degeneracy. Also for λ, the limits presented here are stricter.

The present single parameter limits on $d\kappa$ and λ are in agreement with both the ZEUS results and the 95% CL from the four LEP experiments combined [71]

$$\begin{aligned} -0.042 < d\kappa < 0.136, \\ -0.062 < \lambda < 0.026. \end{aligned} \tag{10.8}$$

These results exclude the first allowed domain in (10.3).

10.4 Measurement of the W Boson Polarisation Fractions

The measurement of the W boson polarisation fractions has been performed for the first time at HERA. For the measurement, the W boson rest frame has been resconstructed and the cosine of the charged lepton decay angle θ^* was used, weighed with the lepton charge $q_\ell = \pm 1$ to be able to use W bosons of both charges (Section 3.5). The single differential W boson production cross section $d\sigma_W / d(q_\ell \cos\theta^*)$ was derived and fit to the model of Equation (3.12) to extract the polarisation

electron in the final state. At this moment there are no recent ZEUS results available.

fractions. The measurement of the W boson polarisation fractions F_- and F_0, for left handed and longitudinally polarised W bosons, respectively, were obtained by fixing F_- to its SM value while fitting F_0, and vice versa. The results are in agreement with the SM

$$F_- = 0.56 \pm 0.16\,(\text{stat}) + 0.02 - 0.02\,(\text{sys}) \quad \text{SM:} \quad 0.61 \pm 0.01\,(\text{stat}), \tag{10.9}$$

$$F_0 = 0.14 \pm 0.23\,(\text{stat}) + 0.01 - 0.01\,(\text{sys}) \quad \text{SM:} \quad 0.17 \pm 0.01\,(\text{stat}). \tag{10.10}$$

$$\tag{10.11}$$

The two dimensional 68% and 95% CL regions were also extracted (Figure 9.13). This was done by leaving both F_- and F_0 free in the fit. The resulting χ^2 distribution was renormalised considering only the physical domain for F_- and F_0. The measurement is statistically limited and the result is also compatible with the predictions for W boson polarisation within a model of anomalous single top production via FCNC.

The W boson polarisation fractions have not been measured before in ep scattering. Since the polarisation properties of the W boson depend on the production mechanism, a direct comparison with other measurements is not possible. However, measurements of the polarisation fractions have been performed previously, using much the same method. Mentioned here are the measurements by L3 and OPAL at LEP [72, 73] and by D0 and CDF at the Tevatron [74, 75]. At the Tevatron the large hadronic background makes the measurement difficult and typically 100 events are used from $t\bar{t}$ production, where the W boson is produced in the decay of the top quark. This is a direct test of the top quark properties, whereas in the present analysis, the W boson properties in $\gamma q \to W q'$ collisions are tested. The LEP experiments use 2000 to 4000 events, depending on which W boson production processes and decay channels are included. Latter experiments establish the polarisation fractions at the 10% level. Mentioned experiments do not observe deviations from the SM.

10.5 Outlook

The results presented in this work explore a new research domain related to the production of real W bosons in ep collisions at HERA. Although statistically limited, significant measurements have been performed for the first time and lead to unique tests of the SM. The measurements can be further improved by combining H1 and ZEUS data and be used for further comparisons with BSM models.

APPENDIX

A-1 Samples

NC DIS

The assessment of the charge misidentification (Chapter 9) makes use of a NC DIS sample, using data taken in the years 1999-2006, corresponding to an integrated luminosity of 296 pb^{-1}. This sample is required to satisfy all criteria of the general data preselection of Chapter 6. Further events are selected, in which an identified electron is isolated against hadrons and has an energy $E_e > 15$ GeV and $P_T > 10$ GeV. Futhermore, the event's $Q^2 > 113$ GeV^2 and $y < 0.63$ unless $Q^2 > 890$ GeV^2. Furthermore, the requierement that $35 < E - P_Z < 63$ GeV must be satisfied. Finally, the track associated to the electron must have a minimal distance of closest approach to the cluster of 12 cm. The ep background is dominated by photoproduction and is estimated at the 0.1% level, see for example Refs [10, 76].

Enriched Control Samples

The study of the description of each particular background, in the measurement of the W boson polarisation fractions, makes use of 'enriched' samples (Section 9.5). These samples have the same detection phase space definition in both lepton channels as the $\ell + \not{P}_T$ selection. Additionally, the cuts described in Chapter 9, to select events from the $\ell + \not{P}_T$ data sample for the polarisation fractions measurement, are also applied. The additional cuts to select a particular background process are described here. More details can be found in Ref. [20]. The data is taken in the years 2003-2005 and correspond to an integrated luminosity of 169 pb^{-1}.

- **Electron Channel Neutral Current**
  In the detection phase space, the NC processes dominate. Cuts are applied to reduce, in particular, the CC component. Since in CC events the misidentified lepton is usually part of a jet, a minimal distance of one unit in $\eta - \phi$ space is required between the isolated lepton and all jets and other tracks in the event.

- **Electron Channel Charged Current**
  The CC processes are selected by suppressing the dominant NC component. It is required that $\zeta > 2500$ GeV^2, since for photoproduction processes $Q^2 = \zeta$, and a strong peaking at small values of Q^2 is observed for the latter. Another significant amount of photoproduction is removed by requiring $V_{ap}/V_p < 0.15$. Events with genuine $\not{P}_T$ generally have low values for V_{ap}/V_p. Since NC events are intrinsically balanced, the scattered electron and the jet are mostly back-to-back. Therefore a cut on the opening angle in the transverse plane between these is applied $\Delta\phi_{\ell - X} < 160^o$. Furthermore, it is required that $E - P_Z < 50$ GeV. This removes part of the NC and LL components, which peak around $\delta_{\text{miss}} = 0$ GeV and fall off steeply above 5 GeV.

- **Muon Channel Charged Current**
  The main cut applied in the muon channel to select CC events is done by requiering $V_{ap}/V_p < 0.15$. The events must contain at least one muon. Isolation criteria are not applied, since most

misidentified muons form part of a hadronic jet and it is important that this is well understood. In addition it is required that $\Delta\phi_{\ell-X} < 170^o$.

- **Muon Channel Lepton Pair** Similarly to the NC enriched selection, isolation cuts are applied to suppress the CC component. In addition a cut is applied $V_{ap}/V_p < 0.2$.

References

[1] S. L. Glashow, "Partial Symmetries Of Weak Interactions", Nucl. Phys. **22**, 579 (1961).
A.Salam, in: Elementary Particle Theory, ed. N.Svartholm (Almquist and Wiksells, Stockholm) (1968). S. Weinberg, "A Model Of Leptons", Phys. Rev. Lett. **19**, 1264 (1967).

[2] L. Arnaudon *et al.* [Working Group on LEP Energy], "Measurement of the mass of the Z boson and the energy calibration of LEP", Phys. Lett. B **307**, 187 (1993).

[3] F. Abe *et al.* [CDF Collaboration], "Measurement of the W boson mass", Phys. Rev. Lett. **75**, 11 (1995), [hep-ex/9503007].

[4] P. Schmueser, "The Electron Proton Colliding Beam Facility Hera", Nucl. Instrum. Meth. A **235**, 201 (1985).

[5] I. Abt *et al.* [H1 Collaboration], "The H1 detector at HERA", Nucl. Instrum. Meth. A **386**, 310 (1997).
I. Abt *et al.* [H1 Collaboration], "The Tracking, calorimeter and muon detectors of the H1 experiment at HERA", Nucl. Instrum. Meth. A **386**, 348 (1997).

[6] M. Derrick *et al.* [ZEUS Collaboration], "A Measurement of sigma(t) (gamma p) at s**(1/2) = 210-GeV", Phys. Lett. B **293**, 465 (1992).

[7] C. Adloff *et al.* [H1 Collaboration], "Deep-inelastic inclusive e p scattering at low x and a determination of alpha(s)", Eur. Phys. J. C **21**, 33 (2001), [hep-ex/0012053].

[8] I. Abt *et al.* [H1 Collaboration], "Measurement of the proton structure function F2 (x, Q**2) in the low x region at HERA", Nucl. Phys. B **407**, 515 (1993).

[9] M. Derrick *et al.* [ZEUS Collaboration], "Measurement of the proton structure function F2 in e p scattering at HERA", Phys. Lett. B **316**, 412 (1993).

[10] C. Adloff *et al.* [H1 Collaboration], "Measurement of neutral and charged current cross-sections in positron proton collisions at large momentum transfer", Eur. Phys. J. C **13**, 609 (2000), [hep-ex/9908059].

[11] V. Andreev *et al.* [H1 Collaboration], "Isolated electrons and muons in events with missing transverse momentum at HERA", Phys. Lett. B **561**, 241 (2003), [hep-ex/0301030].

[12] K, Korcsak-Gorzo, "Events with an isolated lepton and missing transverse momentum at ZEUS", To be pusblished in the proceedings of DIS 2007.
http://indico.cern.ch/getFile.py/access?contribId=123&sessionId=9&resId=0&materialId=slides&confId=9499

[13] U. Baur and D. Zeppenfeld, "MEASURING THE W W gamma VERTEX IN SINGLE W PRODUCTION AT e p COLLIDERS", Nucl. Phys. B **325**, 253 (1989).

[14] T. Araki *et al.* [KamLAND Collaboration], "Measurement of neutrino oscillation with KamLAND: Evidence of spectral distortion", Phys. Rev. Lett. **94**, 081801 (2005), [hep-ex/0406035].

[15] E. Rutherford, "The Scattering of α and β Particles by Matter and the Structure of the Atom", Phil. Mag. **21**, 669 (1911).
http://fisica.urbenalia.com/arts/structureatom.pdf

[16] C. Adloff *et al.* [H1 Collaboration], "Determination of the longitudinal proton structure function F(L)(x,Q**2) at low x", Phys. Lett. B **393**, 452 (1997), [hep-ex/9611017].

[17] A. M. Cooper-Sarkar, R. C. E. Devenish and A. De Roeck, "Structure functions of the nucleon and their interpretation", Int. J. Mod. Phys. A **13**, 3385 (1998), [hep-ph/9712301].

[18] N. Arteaga-Romero, C. Carimalo and P. Kessler, "High P(t) lepton pair production at e p colliders: Comparison between various production mechanisms", Z. Phys. C **52**, 289 (1991).

[19] B.LEISSNER, thesis, Muon Pair Production in Electron-Proton Collisions, I.Phys.Institut RWTH Aachen 10/02, DESY-THESIS-2002-049.

[20] D. M. South, "Events with isolated leptons and missing transverse momentum in e+ p collisions at HERA", DESY-THESIS-2003-030.
http://www.slac.stanford.edu/spires/find/hep/www?r=desy-thesis-2003-030

[21] U. Baur, J. A. M. Vermaseren and D. Zeppenfeld, "Electroweak Vector Boson Production In High-Energy E P Collisions", Nucl. Phys. B **375**, 3 (1992).

[22] H. L. Lai *et al.*, "Improved parton distributions from global analysis of recent deep inelastic scattering and inclusive jet data", Phys. Rev. D **55**, 1280 (1997), [hep-ph/9606399].

[23] P. Aurenche, P. Chiappetta, M. Fontannaz, J. P. Guillet and E. Pilon, "Higher order QCD corrections to the photoproduction of a direct photon at HERA", Z. Phys. C **56**, 589 (1992).

[24] S. D. Drell and T. M. Yan, "Massive Lepton Pair Production In Hadron-Hadron Collisions At High-Energies", Phys. Rev. Lett. **25**, 316 (1970) [Erratum-ibid. **25**, 902 (1970)].

[25] C. F. von Weizsacker, "Radiation emitted in collisions of very fast electrons", Z. Phys. **88**, 612 (1934).

[26] E. J. Williams, "Nature of the high-energy particles of penetrating radiation and status of ionization and radiation formulae", Phys. Rev. **45**, 729 (1934).

[27] G. Altarelli and G. Parisi, Nucl. Phys. B **126**, 298 (1977).

[28] K. P. Diener, C. Schwanenberger and M. Spira, "Photoproduction of W bosons at HERA: Reweighting method for implementing QCD corrections in Monte Carlo programs", hep-ex/0302040.

[29] P.Nason, R.Ruč̈k and M.Spira, Proceedings of the 3rd UK Phenomenology Workshop on HERA Physics, Durham, 1998, J.Phys.**G25** (1999) 1434.

[30] M. Spira, "W boson production at NLO", hep-ph/9905469.

[31] K. P. Diener, C. Schwanenberger and M. Spira, "Photoproduction of W bosons at HERA: QCD corrections", Eur. Phys. J. C **25**, 405 (2002), [hep-ph/0203269].

[32] K. Hagiwara, R. D. Peccei, D. Zeppenfeld and K. Hikasa, "Probing the Weak Boson Sector in e+ e- → W+ W-", Nucl. Phys. B **282**, 253 (1987).

[33] W. M. Yao *et al.* [Particle Data Group], J. Phys. G **33**, 1 (2006).

[34] A. Aktas *et al.* [H1 Collaboration], "Tau lepton production in e p collisions at HERA", [hep-ex/0604022].

[35] G. Frising, "Rare phenomena and W production in electron proton scattering at HERA", DESY-THESIS-2004-048.
http://www.slac.stanford.edu/spires/find/hep/www?r=desy-thesis-2004-048
K. P. Diener, C. Schwanenberger and M. Spira, "Photoproduction of W bosons at HERA: Reweighting method for implementing QCD corrections in Monte Carlo programs", [hep-ex/0302040].
P. Nason, R. Ruckl and M. Spira, "A note on W boson production at HERA", J. Phys. G **25**, 1434 (1999). [hep-ph/9902296].

[36] E. Perez, private communication.

[37] K. Ackerstaff *et al.* [HERMES Collaboration], "HERMES spectrometer," Nucl. Instrum. Meth. A **417**, 230 (1998), [hep-ex/9806008].

[38] E. Hartouni *et al.* [HERA-B Collaboration], "An Experiment to Study CP Violation in the B System Using an Internal Target at the HERA Proton Ring,", Design Report, DESY-PRC 95/01 (1995).

[39] A. Mehta, "HERA upgrade and prospects," Acta Phys. Polon. B **33**, 3937 (2002).

[40] A. Aktas *et al.* [H1 Collaboration], [hep-ex/0703022].

[41] S. Burke, R. C. W. Henderson, S. J. Maxfield, J. V. Morris, G. D. Patel, D. P. C. Sankey and I. O. Skillicorn, "Track finding and fitting in the H1 forward track detector", Nucl. Instrum. Meth. A **373**, 227 (1996).

[42] R. Brun, R. Hagelberg, M. Hansroul and J. C. Lassalle, "Geant: Simulation Program For Particle Physics Experiments. User Guide And Reference Manual".

[43] A.B. Meyer. *A New Object-Oriented Data Analysis Framework.* Published in Budapest 2001, High Energy Physics hep200/276.

[44] R. Brun, F. Rademakers and S. Panacek, "ROOT, an object oriented data analysis framework", http://www.slac.stanford.edu/spires/find/hep/www?irn=4655214SPIRES entry *Prepared for CERN School of Computing (CSC 2000), Marathon, Greece, 17-30 Sep 2000.*

[45] H. Jung, *Hard Diffractive Scattering in High Energy ep Collisions and the Monte Carlo Generator RAPGAP*, Comput. Phys. Commun. **86** (1995) 147;
See also: https://www.desy.de/∼Ejung/rapgap/welcome.html

[46] G. A. Schuler and H. Spiesberger, *DJANGO: The Interface for the Events Generators HERACLES and LEPTO in ep Collisions*, Comput. Phys. Commun. **101** (1997) 135.

[47] T. Abe, "GRAPE-Dilepton (Version 1.1): A generator for dilepton production in e p collisions", Comput. Phys. Commun. **136**, 126 (2001), [hep-ph/0012029].

[48] Ch. Berger and P.Kandel, "A new Generator for Wide Angle Bremsstrahlung". http://www.desy.de/∼Eheramc/proceedings/wg70/proc.wabgen.ps.gz

[49] E. E. Boos, M. N. Dubinin, V. A. Ilyin, A. E. Pukhov and V. I. Savrin, "CompHEP: Specialized package for automatic calculations of elementary particle decays and collisions", hep-ph/9503280.

[50] C. Adloff *et al.* [H1 Collaboration], "Measurement and QCD analysis of neutral and charged current cross sections at HERA", Eur. Phys. J. C **30**, 1 (2003) [hep-ex/0304003].

[51] B. Heineman, *Measurement of Charged Current and Neutral Current Cross Sections in Positron-Proton Collisions at* $\sqrt{s} \simeq$ *300 GeV.* Dissertation, Fachbereich Physik der Universität Hamburg (1999).

[52] M. GOETTLICH, thesis, Study of Charm and Beauty Production at HERA/H1 using Dilepton Events DESY-THESIS-2007-012, Univ. Hamburg 2007.

[53] M. Peez, B. Portheault and E. Sauvan, "An Energy Flow Algorithm for Hadronic Reconstruction in OO: Hadroo2", H1 Note, H1-01/05-616.

[54] K. H. Klimek [H1 Collaboration], "Beauty production at HERA", hep-ph/0305266.

[55] M.PEEZ,Univ. Lyon, "Recherche de deviations au Model Standard dans les processus de grande energie transverse sur le collisionneur electron - proton HERA", DESY-THESIS-2003-023.

[56] J.DINGFELDER, thesis, "Search for Anomalous Production of Single Top Quarks with the H1 Experiment at HERA", Univ.Heidelberg, 01/03.

[57] S. Bentvelsen, J. Engelen and P. Kooijman, "Reconstruction Of (X, Q**2) And Extraction Of Structure Functions In Neutral Current Scattering At Hera", NIKHEF-H-92-02 http://www.slac.stanford.edu/spires/find/hep/www?r=nikhef-h-92-02

[58] A. Schoëning, *Untersuchung von Prozessen mit virtuellen und reellen* $W^{\pm}$*-Bosonen am H1-Detektor bei HERA.* Dissertation, Fachbereich Physik der Universität Hamburg (1996).

[59] Christian Veelken, *H1NonepBgFinder - Rejection of cosmic muon and beam-halo events in the H1oo framework*, H1-09/02-603 (H1 internal note).

[60] T. Ahmed *et al.* [H1 Collaboration], "Observation of an e+ p → mu+ X event with high transverse momenta at HERA", DESY-94-248.
http://www.slac.stanford.edu/spires/find/hep/www?r=desy-94-248

[61] C. Adloff *et al.* [H1 Collaboration], "Observation of events with an isolated high energy lepton and missing transverse momentum at HERA", Eur. Phys. J. C **5** (1998) 575, [hep-ex/9806009].

[62] J. Breitweg *et al.* [ZEUS Collaboration], "W production and the search for events with an isolated high-energy lepton and missing transverse momentum at HERA", Phys. Lett. B **471**, 411 (2000), [hep-ex/9907023].

[63] Preliminary Isolated Electrons and Muons: H1prelim-07-063 https://www-h1.desy.de/h1/www/publications/htmlsplit/H1prelim-07-063.long.html.

[64] Presented at: Deep Inelastic Scattering (DIS) 2006, München, Germany. Slides: http://indico.cern.ch/contributionDisplay.py?contribId=124&sessionId=9&confId=9499

[65] M. Mozer, *Measurement and QCD analysis of Diffractive Jet Cross Sections in Deep-Inelastic Scattering at HERA*, Thesis, University Heidelberg, DESY thesis H1TH-431.

[66] T. Sjostrand, S. Mrenna and P. Skands, "PYTHIA 6.4 physics and manual", JHEP **0605**, 026 (2006), [hep-ph/0603175].

[67] A. Aktas *et al.* [H1 Collaboration], "A general search for new phenomena in e p scattering at HERA", Phys. Lett. B **602**, 14 (2004), [hep-ex/0408044].

[68] F. James and M. Roos, Comput. Phys. Commun. **10**, 343 (1975).

[69] V. Blobel, E. Lohrmann, "Statistische und numerische Methoden der Datenanalyse", Teubner Studeienbuc̆her, 1998. ISBN: 3-519-03243-0.

[70] D. Waters, T. Matsushita, Private communication.

[71] P. Spagnolo, "Boson gauge couplings at LEP", [hep-ex/0506048].

[72] P. Achard *et al.* [L3 Collaboration], "Measurement of W polarisation at LEP", Phys. Lett. B **557**, 147 (2003), [hep-ex/0301027].

[73] G. Abbiendi *et al.* [OPAL Collaboration], "W boson polarisation at LEP2", Phys. Lett. B **585**, 223 (2004), [hep-ex/0312047].

[74] V. M. Abazov *et al.* [D0 Collaboration], "Measurement of the W boson helicity in top quark decay at D0", Phys. Rev. D **75**, 031102 (2007), [hep-ex/0609045].

[75] A. Abulencia *et al.* [CDF II Collaboration], "Measurement of the Helicity Fractions of W Bosons from Top Quark Decays using Fully Reconstructed $t\bar{t}$ Events with CDF II", Phys. Rev. D **75**, 052001 (2007), [hep-ex/0612011].

[76] C. Adloff *et al.* [H1 Collaboration], "Measurement of neutral and charged current cross sections in electron proton collisions at high Q**2", Eur. Phys. J. C **19**, 269 (2001) [hep-ex/0012052].

All theses are available at: `https://www-h1.desy.de/publications/theses_list.html`

Summary

A key process in understanding the dynamics of the electroweak interactions in the Standard Model (SM) is single W boson production. One of the most striking signatures of this process at HERA is the observation of events with isolated leptons (electrons or muons) and missing transverse momentum, or '$\ell + \not{P}_T$' events. In a data sample collected with the H1 detector corresponding to an integrated luminosity of 481 pb^{-1}, 58 such events are observed for a SM prediction of 57.4 ± 7.3. The purity of the H1 analysis in the signal, dominated within the SM by the W boson production, is at the 75% level. This allowed for the determination of the model-independend production cross section for $\ell + \not{P}_T$ events

$$\sigma_{\ell+\not{P}_T} = 0.24 \pm 0.05\,(\text{stat}) \pm 0.04\,(\text{sys}) \quad \text{pb}, \tag{1.1}$$

which is in agreement with the SM expectation of 0.26 ± 0.04 pb. The measurement of $\ell + \not{P}_T$ events is also used to determine the cross section for single W boson production at HERA

$$\sigma_W = 1.23 \pm 0.25\,(\text{stat}) + 0.13\,(\text{sys}) \ \text{pb}, \tag{1.2}$$

which is in good agreement with the SM expectation of 1.31 ± 0.20 pb. This is the most precise measurement of the single W boson production cross section to date in ep scattering.

The single W boson production cross section is sensitive to anomalous values of the coupling parameters $d\kappa$ and λ that govern the $WW\gamma$ coupling. The number of observed $\ell + \not{P}_T$ events are used to extract limits on the possible anomalous values of $d\kappa$ and λ, which have SM expectation values $d\kappa = \lambda = 0$. The following 95% CL single parameter limits are obtained

$$-4.9 < d\kappa < -2.7 \quad \text{and} \quad -0.8 < d\kappa < 1.5, \tag{1.3}$$

and

$$-2.9 < \lambda < 2.9. \tag{1.4}$$

No deviations from the SM are observed. Due to the limited statistics, these limits are not competitive with the corresponding results obtained at LEP and the Tevatron.

The W boson is further studied using the charged lepton decay angle in the W boson rest frame. The W boson polarisation fractions F_- and F_0, for left handed and longitudinally polarised W bosons, respectively, were measured for the first time at HERA. The two-dimensional 68% and 95% CL regions were extracted. In addition, F_- and F_0 were measured in single parameter fits

$$F_- = 0.56 \pm 0.16\,(\text{stat}) + 0.02 - 0.02\,(\text{sys}), \tag{1.5}$$

$$F_0 = 0.14 \pm 0.23\,(\text{stat}) + 0.01 - 0.01\,(\text{sys}), \tag{1.6}$$

which is consistent with the SM predictions $F_- = 0.61 \pm 0.01$ and $F_0 = 0.17 \pm 0.01$.

These measurements provide a unique test of the SM. The main uncertainty is due to statistics and can be further improved in a future H1/ZEUS combined analysis.

Samenvatting

Het proces waarbij een quasi reëel W boson geproduceerd wordt, speelt een grote rol in het begrijpen van de elektrozwakke dynamica van het Standaard Model (SM). Een van de meest in het oog lopende eigenschappen van W boson productie aan HERA is het optreden van detectorsignaturen (events), waarbij een geisoleerd, hoog energetisch lepton (elektron of muon) wordt aangetroffen samen met een significant missend momentum, afgekort '$\ell + \not{P}_T$' events. H1 heeft 58 $\ell + \not{P}_T$ events waargenomen, tegen een SM voorspelling van 57.4 ± 7.3, in een data sample overeenkomend met een geïntegreerde luminositeit van 481 pb^{-1}. De dominante bijdrage aan dit sample, met meer dan 70%, is W boson productie in het SM. Dit heeft het mogelijk gemaakt een significante modelonafhankelijke meting te doen van het productieproces van $\ell + \not{P}_T$ events aan HERA. De gemeten werkzame doorsnede van $\ell + \not{P}_T$ events is

$$\sigma_{\ell+\not{P}_T} = 0.24 \pm 0.05\,(\text{stat}) \pm 0.04\,(\text{sys}) \quad \text{pb}, \tag{1.7}$$

hetgeen overeenkomt met de SM voorspelling van 0.26 ± 0.04 pb. Hetzelfde sample is ook gebruikt om de werkzame doorsnede van het productieproces van resonante W bosonen af te leiden

$$\sigma_W = 1.23 \pm 0.25\,(\text{stat}) + 0.13\,(\text{sys}) \ \text{pb}, \tag{1.8}$$

hetgeen consistent is met de SM verwachting 1.31 ± 0.20 pb. Dit is de eerste significante bepaling van de werkzame doorsnede van de resonante productie van W bosonen in elektron-proton verstrooiing.

De werkzame doorsnede van W bosonen aan HERA is gevoelig voor anomale waarden van de koppelingsparameters $d\kappa$ en λ, welke de $WW\gamma$ vertex parametriseren. De meting van $\ell + \not{P}_T$ events heeft het mogelijk gemaakt limieten te zetten op mogelijke afwijkende waarden van $d\kappa$ en λ. In het geval dat slechts een parameter gevarieerd wordt en alle andere parameters hun SM waarden hebben, zijn de volgende 95% CL limieten gevonden voor $d\kappa$

$$-4.9 < d\kappa < -2.7 \quad \text{en} \quad -0.8 < d\kappa < 1.5, \tag{1.9}$$

en

$$-2.9 < \lambda < 2.9. \tag{1.10}$$

Geen afwijkingen van het SM zijn waargenomen. De meting is statistisch bepaald en concurrereert daarom niet met de resultaten behaald aan LEP en de Tevatron.

Het W boson is tevens geanalyseerd waarbij gebruik gemaakt is van de vervalshoek van het geladen vervalslepton in het rustsysteem van het W boson. De polarisatiefracties F_- and F_0, voor linkshandige en longitudinaal gepolariseerde W bosonen, zijn hiermee voor het eerst gemeten aan HERA. Het 68% en 95% CL gebied voor F_- and F_0 zijn berekend. Tevens zijn F_- en F_0 gemeten in fits waarbij een parameter per keer is gevarieerd

$$F_- = 0.56 \pm 0.16\,(\text{stat}) + 0.02 - 0.02\,(\text{sys}), \tag{1.11}$$

$$F_0 = 0.14 \pm 0.23\,(\text{stat}) + 0.01 - 0.02\,(\text{sys}), \tag{1.12}$$

in overeenstemming met de SM voorspellingen $F_- = 0.61 \pm 0.01$ and $F_0 = 0.17 \pm 0.01$.

Deze metingen verschaffen een unieke test van het SM. De statistische precisie bepaalt de meetonzekerheid en kan verbeterd worden door in de toekomst de data van H1 en ZEUS te combineren.

Acknowledgements

This work would not have come into existence without the help from many different people and it is based on many man-years of work by members of the H1 collaboration and the engineers of the HERA machine. A collective 'thank you' to all of them.

Apart from that, I would like to mention some individuals here.

First of all I want to humbly thank my parents for their constant, thorough and steady support. Without their help my life would have been incredibly more difficult during the past four years (or 31 years for that matter)!

Secondly, I want to thank the three key persons who made this thesis possible. Many thanks Bob van Eijk for having enough faith in me, four years ago already, that I would come up with a worthy thesis. Many thanks to Cristinel Diaconu for guiding me continuously during the past years. His help, support and ideas have co-created this thesis. The third key-person I want to thank is Andrey Afrikanovich Rostovtsev. He took me in as a member of the co-working researchers at the ITEP institute in Moscow. Without him, I would not have gotten into H1.

Many thanks to David Milstead for stimulating discussions and for showing me how much fun phenomenological research can be. With David I worked in Sweden in 2005 and 2006 on two publications regarding the phenomenology of exotic heavy stable particles (including R-hadrons). Thanks to the other two authors of the last paper, Alexey Kaidalov and Olga Piskunova, as well.

Many thanks as well to Dima Ozerov for being incredibly lenient with me regarding my H1OO duties while I was writing my thesis. Many thanks to Voica Radescu. Not only for proof-reading substantial parts of my thesis and useful discussions on structure functions (I think I finally got it), but also for being enormously patient with me when I had no time to go dancing! (To be replenished soon.) Thanks to Gerhard Brandt for showing me how to automate and for proof-reading and useful discussions. Thanks to Dave South for proof-reading and useful discussions as well.

Thanks to Siebe Boersma for putting the fine art on this thesis. Many thanks to Berend de Boer and Jeroen Steen for being my paranymphs during the defence. Finally, I want to thank the following people for useful and supportive discussions: Joachim Meyer, Daniel Pitzl, Hannes Jung, Serguei Levonian, and Hans-Ulrich Martyn.